

Fachhochschule Kärnten
Carinthia University of Applied Sciences
Electrical Energy and mobility systems



MASTER THESIS

Modification of a Heating unit for Dynamic Measurement Station to perform Analysis on Switching losses of SiC Mosfet over temperature

Submitted in Partial Fulfillment of the Requirements of the Academic Degree

Master of Science in Engineering, Msc

Author: Basil Jacob

Registration Number: 2210673007

Supervisor: FH-Prof. Dipl.-Ing. Winfried Egger
Fachhochschule Kärnten

Second supervisor: Mr. Steinberger Andrej
Infineon Technologies Austria AG

Villach, June 2025

Declaration of Originality

I hereby declare that

- I have independently written the presented Master thesis by myself;
- I have prepared this Master thesis without outside help and without using any sources or aids other than those cited by me. Moreover, I have identified as such any passages taken verbatim or in terms of content from the sources used;
- In addition, I have fully indicated the use of generative AI models (e.g., ChatGPT) by specifying the product name and the reference source (e.g., URL);
- I have not used any other unauthorized aids and have consistently worked independently, and when using generative AI models, I realize that I am responsible for how the content will be used and to what extent;
- I have not yet submitted this Master thesis in the same or similar form to any (other) educational institution as an examination performance or (scientific) thesis.

I am aware that any violation ("use of unauthorized aids") violates academic integrity and may result in (academic-related) legal consequences.

(Place, Date)

(Signature)

Abstract

This thesis presents the development and implementation of a digitally controlled heating system designed to facilitate temperature-dependent switching loss analysis of Silicon Carbide (SiC) MOSFETs. SiC devices are increasingly used in high-efficiency power electronics due to their low losses and high-temperature capability. However, their switching behavior varies significantly with temperature, necessitating accurate and controlled thermal testing.

To address this, a commercial RS PRO SMD rework station was reverse engineered and modified into a microcontroller-based heating unit. The system integrates MAX31865 and PT1000 sensors for accurate temperature feedback, controlled via a PID algorithm implemented on an Arduino Mega 2560. A Python-based GUI was developed for real-time control, visualization, and safety features. The heating unit was then integrated into a Double Pulse Test (DPT) setup to measure switching losses at various temperatures.

The results revealed a clear temperature dependency in the turn-on losses (E_{on}), with minimal variation in turn-off losses (E_{off}), validating both the hardware and measurement methodology. In addition to technical achievements, the project also provided exposure to industry-standard measurement practices, waveform analysis, and in-depth knowledge of SiC MOSFET behavior. This system offers a scalable and cost-effective platform for future research and test automation in power semiconductor characterization.

Acknowledgement

I would like to express my sincere gratitude to everyone who supported and guided me throughout the course of this master's thesis. The successful completion of this work was made possible through the invaluable contributions of several individuals and institutions.

First and foremost, I extend my heartfelt thanks to my first supervisor, Prof. Winfried Egger, for his guidance, constructive feedback, and academic mentorship throughout this research. His encouragement and support helped maintain clarity and direction during the entire process.

I am deeply grateful to my second supervisor, Mr. Andrej Steinberger from Infineon Technologies Austria AG, for his technical insights and professional advice. His practical knowledge and dedicated supervision were instrumental in refining the experimental aspects of this work. Beyond his official role, he has been a great teacher to me from the very beginning. He was always patient and generous with his time, explaining topics clearly and understandably. Whenever I faced challenges, he never hesitated to help and often came up with several possible solutions. His deep knowledge and constant support made a big difference in my learning and progress.

I would like to especially thank my manager, Mr. Kassmannhuber Andreas, for his unwavering support, for entrusting me with this project, and for facilitating the conditions needed to carry it out successfully. His guidance, openness, and timely assistance were invaluable. I am particularly grateful for his thoughtful decision in assigning me a highly experienced and supportive supervisor, and for continuously encouraging my academic and professional development throughout this journey.

My sincere appreciation also goes to Infineon Technologies Austria AG for providing the opportunity and infrastructure necessary for conducting this thesis.

Special thanks are due to my colleagues and friends, whose cooperation, shared ideas, and motivation positively influenced the progress of this thesis.

Lastly, I wish to express my deepest gratitude to my parents and siblings. Their unconditional support, patience, and belief in me have been a constant source of strength and inspiration throughout this journey.

Thank you all for your valuable contributions to this work.

Contents

Declaration of Originality	ii
Abstract	iii
Acknowledgement	iv
List of Figures	xiii
List of Tables	xiv
1 Introduction	1
2 Background and Literature Review	5
2.1 Switching Losses in SiC MOSFETs	5
2.2 Dynamic Measurement Techniques	6
2.3 Compact Heating Unit Designs and Modifications	6
2.4 Temperature Sensing and Digital PID Control	7
2.5 Research Gap and Contribution	7
3 Reverse engineering of RS PRO rework station	9
3.1 Finding Traces	10
3.2 Schematics	11
3.3 Atmega Microcontroller	12

3.4	Voltage regulation	13
3.5	Mains and Heater driver Circuit	13
3.6	Temperature sensor & Amplification, and Handle sensor	15
3.7	Fan Controller	16
3.8	Circuit for Analog Reference	16
3.9	Display	17
4	Design and Development of the Digital Temperature Control System – First Prototyping Phase	18
4.1	Configuration of the MAX31865 module with the PT1000 sensor . .	19
4.2	Interfacing between the Arduino Mega and the original PCB . . .	20
4.3	Experimental setup	20
4.4	Control block diagram	21
4.5	Preliminary results obtained	22
5	Design and Development of the Digital Temperature Control System – Second Prototyping Phase	24
5.1	The new PCB contains MAX31865, MAX31855 and Protection Circuit	24
5.2	New Arduino Compatible PCB	26
5.3	Adapter that Connects Main PCB to Controller	27
5.4	Delays in Adafruit MAX31865 Library	28
5.5	Non-blocking Continuous Code	29
5.6	Control Diagram	29
5.7	Different Use Cases	30
5.7.1	Case 1	30
5.7.2	Case 2	31
5.7.3	Case 3	32

5.8	PID Tuning: Trial and Error Method	32
5.8.1	Experiment Concept	32
5.8.2	Obtained Results	34
5.9	Designing of GUI for Temperature Control and Monitoring—First Phase	36
6	Design and Development of Digital Temperature Control Systems	
	– New Python PyQt-based GUI	38
6.1	GUI Overview	38
6.2	Main Plot and System Information	39
6.3	System Control, Temperature and Fan Controls, Sensor and Protection Setting	40
6.4	COM Port Selection and Interactive Status Bar	40
6.5	Performance Analysis with PT1000 as Feedback Source	41
6.6	Performance Analysis with K-Thermocouple as Feedback Source . .	42
6.7	Different Protection Mechanisms	43
6.7.1	Over-Temperature Protection Using Protection Threshold Setting	43
6.7.2	Over-Temperature Protection Using Hot Gun Temperature .	44
6.7.3	Under-Temperature Protection	45
6.8	Problem Observed with Interposer Assembly	46
6.9	Custom Back Panel for Heating Unit	47
7	Measurement and Analysis of SiC MOSFET Switching Losses over Temperature	49
7.1	Purpose of the Measurement and Analysis	49
7.2	Objectives of Double Pulse Test	50
7.3	Test Setup	51
7.4	Description of the Test Circuit	53

7.5	Measurement Board	55
7.6	Equipment Used	57
7.6.1	Dynamic Measurement Station	57
7.6.2	Power Supply	60
7.6.3	Oscilloscope	61
7.6.4	Measurement Probes (Voltage/Current)	62
7.7	De-skewing Methods and Procedure	64
8	Measurement Procedure for Switching Loss Analysis	66
8.1	Test Procedure	66
8.2	Preparation and Initial Checks	67
8.2.1	Pulse Width and Timing	68
8.2.2	Gate Resistance and Drive Voltage	68
8.3	Measurement Points	69
8.3.1	Voltage Probing Locations	69
8.3.2	Current Probing Location	70
8.4	Data Acquisition	70
8.5	Measurement Parameters	71
8.5.1	Turn-on Energy (E_{on})	71
8.5.2	Turn-off Energy (E_{off})	72
8.5.3	Switching Times (t_{on}, t_{off}, t_d)	72
8.6	Parasitic Effects Observed	72
8.7	Verify Functionality of Setup	73
8.7.1	Gate Pulse Test	74
8.7.2	Drain Supply V_{DC}	75

9 Data Analysis	76
9.1 Waveform Interpretation	76
9.1.1 Turn-On	79
9.1.2 Turn-Off	82
9.2 Identifying Switching Events	86
9.3 Calculating Switching Losses	88
9.4 Effect of Test Conditions	90
9.5 Observations and Discussion	92
9.6 Key Findings	99
10 Conclusion and Future work	101
List of Abbreviations	108
Appendix	110
A Source Code	110
A.1 Template File Formats	110
A.1.1 HSPICE	110
A.1.2 VHDL	110
A.2 Generated Netlists	111
A.2.1 HSPICE	111
A.2.2 VHDL	111

List of Figures

3.1	RS PRO Rework Station [1].	9
3.2	After finding traces using GIMP tool	10
3.3	System schematics overview	11
3.4	ATmega microcontroller block	12
3.5	Voltage regulation circuit	13
3.6	Heater driver circuit	14
3.7	Temperature amplification and handle sensor	15
3.8	Fan controller circuit	16
3.9	Analog reference circuit	16
3.10	7-segment display circuit	17
4.1	MAX31865 with PT1000 sensor[2].	19
4.2	Interfacing Arduino Mega and the main PCB	20
4.3	Experimental setup	21
4.4	Control block diagram	22
4.5	settled temp at 100°C line with oscillations	23
4.6	Settled temp at 100°C line with error convergence and tolerance . .	23
5.1	New Schematic for Arduino compatible PCB	25
5.2	Controller PCB Top view	26
5.3	New Arduino compatible PCB	26

5.4	Adapter PCB to interface controller and main board	27
5.5	Delay section in Adafruit MAX31865 library[3].	28
5.6	Code snippet from Adafruit library	28
5.7	Non-blocking continuous mode verified using logic analyzer	29
5.8	Updated control block diagram	30
5.9	Hotgun placed in different position and angle	31
5.10	Hotgun placed in different horizontdal positions over DUT	31
5.11	Hotgun placed in different vertical positions over DUT	32
5.12	Hot air gun on X-Y grid for PID tuning trials	33
5.13	GUI test case with PT1000 sensor: 25C to 50C	36
5.14	GUI test case with thermocouple: 25C to 100C	37
6.1	Main plot and system information panel	39
6.2	COM port selection and status bar	41
6.3	System response using K-type thermocouple	42
6.4	Over-temperature protection based on user-defined threshold	43
6.5	Over-temperature protection triggered by hot gun	44
6.6	Under-temperature protection mechanism	45
6.7	Illustration of the rubber pad, the interposer, and the socket	46
6.8	Custom-designed back panel for Heating Unit	48
7.1	Test Setup of the Dynamic Measurement Station	52
7.2	Schematic of the Double Pulse Test Circuit[4].	54
7.3	Front Side of the Measurement Board	55
7.4	Back Side of the Measurement Board	56
7.5	Dynamic Measurement Station	57
7.6	Back Panel of the Dynamic Measurement Station	58
7.7	GUI of the Dynamic Measurement Station 1	59

7.8	GUI of the Dynamic Measurement Station 2	60
7.9	Keysight N5772A Programmable Power Supply[5].	60
7.10	Keysight InfiniVision DSO-X 6004A Oscilloscope (Front View)[6]. .	61
7.11	Tektronix P6100 Passive Voltage Probe used for V_{GS} Measurement[7].	62
7.12	Tektronix P5100A Differential Probe used for V_{DS} Measurement[8].	63
7.13	Coaxial Shunt Setup for Drain Current Measurement (i_D)	63
7.14	Illustration of Probe Misalignment and Midpoint Alignment during Switching Transition[9].	64
7.15	Overlay of De-skewed V_{DS} and I_D Signals during Switching[9]. . . .	65
8.1	Parameter _{waveform}	71
8.2	Parasitic Equivalent Circuit[9].	73
8.3	Gate Pulse Verification without DUT[10].	74
9.1	dpt timing diagram[9].	77
9.2	dpt scope waveform	78
9.3	dpt scope waveform zoomed	79
9.4	Turn on zoomed waveform	80
9.5	Turn Off zoomed waveform	83
9.6	Turn on energy analysis	87
9.7	Switching loss calculation VSC console 1	88
9.8	Switching loss calculation VSC console 2	90
9.9	Switching Losses vs. Test Current at Different Temperatures	92
9.10	Switching Losses vs. Temperature and Current	94
9.11	Average Switching Energy Loss vs. Current	96
9.12	Average Switching Energy Loss vs. Temperature	97
9.13	Energy loss current temperature plot	99

List of Tables

5.1 PID Tuning Results Across Different Temperature Ranges	34
--	----

Chapter 1

Introduction

The rapid evolution of power electronics has driven the demand for semiconductor devices that can operate efficiently under high voltage, high temperature, and high switching frequency conditions. Among the recent developments, Silicon Carbide (SiC) Metal-Oxide-Semiconductor Field-Effect Transistors (MOSFETs) have emerged as promising candidates to replace conventional silicon-based transistors. Owing to their wide bandgap characteristics, SiC MOSFETs offer significant advantages such as lower conduction and switching losses, higher thermal conductivity, and the ability to withstand higher junction temperatures. These properties render SiC devices particularly suitable for high-efficiency and high-power-density applications, including electric vehicles, renewable energy systems, and industrial motor drives.

Despite their many advantages, the performance of SiC MOSFETs is strongly influenced by their thermal environment. Switching losses—comprising turn-on (E_{on}) and turn-off (E_{off}) energy—exhibit temperature-dependent behavior. Variations in junction temperature can significantly impact carrier mobility, parasitic capacitances, and threshold voltage, thereby altering the dynamic behavior of the device. Accurate characterization of switching losses over a range of operating temperatures is therefore crucial to ensure device reliability, optimize thermal design, and enable robust system-level performance.

The standard approach for evaluating dynamic switching losses is the Double Pulse Test (DPT), which allows isolation of switching events under well-controlled electrical conditions. However, traditional DPT setups often lack integrated thermal

control capabilities, making it difficult to conduct temperature-dependent analyses. To overcome this limitation, a dedicated heating unit must be employed to regulate the device under test (DUT) temperature prior to and during the switching event. This calls for the development of a compact, responsive, and digitally controllable heating system that can be integrated with the DPT hardware and software environment.

In this context, the primary objective of this thesis is to modify an existing heating unit—originally based on an RS PRO 858D SMD rework station—for integration with a dynamic measurement station. The goal is to achieve precise digital control over the DUT temperature and thereby enable systematic analysis of SiC MOSFET switching losses across a wide thermal range. The work involves hardware redesign, embedded software development, control system implementation, and experimental validation through DPT measurements.

To achieve this, the original analog control logic of the RS PRO rework station is reverse engineered and replaced with a custom-designed microcontroller-based system. The new control architecture centers around the Arduino Mega 2560, chosen for its versatility, processing power, and open-source ecosystem. Critical thermal feedback is acquired using a PT1000 resistance temperature detector (RTD), digitized by the MAX31865 RTD-to-digital converter. The digitized temperature data is processed through a Proportional-Integral-Derivative (PID) control algorithm running on the Arduino, which adjusts the power delivered to the heating element via a triac-based driver circuit. This enables precise and real-time temperature regulation of the DUT.

To support user interaction and facilitate dynamic configuration, a graphical user interface (GUI) was developed in Python using the PyQt5 framework. The GUI enables real-time visualization of temperature response, manual input of control parameters, switching between sensor types (PT1000 or thermocouple), and safety threshold adjustments. Communication between the GUI and the Arduino is established via a USB serial link. The software also implements protection features such as over-temperature shutdown and sensor fault detection, enhancing the system's reliability and safety.

The development process followed a phased approach. The first phase focused on integrating the MAX31865 with the PT1000 sensor and validating the closed-loop

control using the Arduino Serial Plotter. A secondary thermocouple and hand-held thermometer were used for cross-verification. In the second phase, a custom controller PCB was designed and fabricated, incorporating both MAX31865 and MAX31855 (for K-type thermocouples) to provide dual-sensor compatibility. A relay-based safety cut-off mechanism was also included to disconnect power in case of excessive temperature.

The PID controller was tuned experimentally across different temperature ranges using a trial-and-error method. A significant finding during this tuning process was that no single set of PID constants yielded optimal results across the entire operating range. Therefore, the temperature range was divided into discrete zones, and suitable PID values were identified for each. Further analysis revealed that the PT1000 sensor provided better stability and lower overshoot compared to the thermocouple, making it the preferred choice for precise applications.

A major part of this thesis is devoted to the measurement and characterization of SiC MOSFET switching losses using the newly developed temperature control system. The modified heating unit was integrated into a Dynamic Measurement Station (DMS) equipped with a half-bridge test board, programmable gate drivers, a differential voltage probe, and a coaxial current shunt. The DUT temperature was precisely controlled using the developed system, and DPT measurements were conducted at multiple temperature levels ranging from room temperature up to 180°C.

Waveforms from the DPT were captured using a high-bandwidth oscilloscope and exported as CSV files for post-processing. A custom Python script was written to parse these files, identify switching intervals, compute Eon and Eoff by integrating the product of drain current and drain-source voltage, and plot the results. These measurements revealed distinct trends in switching losses with respect to temperature. Specifically, Eon exhibited a notable increase with both temperature and current, while Eoff remained relatively constant, highlighting the superior reverse recovery characteristics of the SiC device under test.

The data obtained from these measurements are valuable for power electronics designers seeking to optimize thermal and switching performance in SiC-based converters. Furthermore, the modular and low-cost nature of the heating unit and control system makes it suitable for educational labs, RD facilities, and industrial

test environments.

The significance of this work lies not only in its technical outcomes but also in its methodological approach. By combining embedded system design, sensor integration, digital control, and experimental power electronics testing, the thesis presents a comprehensive solution to a real-world engineering problem. Moreover, the use of open-source hardware and software promotes reproducibility and scalability for future applications.

The scope of the thesis extends beyond the heating unit itself. The system was integrated into a broader testbench involving CAS (Computer Aided Software) for configuring the pulse generator and measurement conditions. This holistic integration ensures that the entire DPT workflow—from device mounting and thermal conditioning to waveform acquisition and loss analysis—is streamlined and reliable. Furthermore, the Python-based GUI class developed as part of this work lays the groundwork for future integration into a larger, fully automated measurement ecosystem. Its modular architecture and dynamic interfacing capabilities make it suitable for expansion into multi-device control, synchronized data logging, and remote experiment execution within advanced laboratory environments.

In summary, this thesis presents the design, implementation, and validation of a digitally controlled heating unit tailored for the dynamic switching loss analysis of SiC MOSFETs. The system combines Arduino-based PID control, MAX31865 sensor interfacing, Python GUI development, and experimental DPT characterization. By enabling systematic and accurate loss measurements over temperature, the work contributes to the advancement of power semiconductor evaluation methodologies and supports the development of more efficient and thermally robust power electronic systems.

Chapter 2

Background and Literature Review

2.1 Switching Losses in SiC MOSFETs

Silicon carbide (SiC) MOSFETs have emerged as superior alternatives to traditional silicon-based power transistors. Their advantages include higher breakdown voltage, lower switching losses, and the ability to operate at elevated temperatures[11, 12]. SiC devices exhibit lower conduction losses due to reduced on-state resistance and enable faster switching transitions because of smaller intrinsic capacitances.

Importantly, switching losses in SiC MOSFETs are influenced by junction temperature. As temperature increases, factors such as threshold voltage shift, carrier mobility reduction, and parasitic capacitance variations affect switching behavior. Nayak et al. characterized how junction temperature affects the reverse recovery behavior of SiC MOSFET body diodes and switching energy in a half-bridge configuration[13]. This temperature robustness makes SiC suitable for automotive and aerospace applications where reliability is critical.

The Double Pulse Test (DPT) is the standard method to experimentally determine switching losses. It enables separation of E_{on} and E_{off} under controlled current and voltage conditions[14]. High-speed probes and accurate synchronization of voltage and current measurements are crucial for precision loss analysis.

2.2 Dynamic Measurement Techniques

Dynamic switching characterization typically involves half-bridge circuits with clamped inductive loads. To isolate thermal effects on switching loss, tests must be performed at known, controlled junction temperatures. However, self-heating during switching complicates such measurements.

Advanced methods incorporate thermal chambers, fluid-cooled platforms, or localized heating units to control temperature[15]. These setups allow systematic evaluation across a range of temperatures. In academic environments, however, resource limitations make compact and cost-efficient setups desirable.

Custom heating units integrated into DPT setups provide a practical alternative. Such systems use localized heating (e.g., resistive blocks or hot air rework handles) to precondition the DUT before measurements. Keysight's application note on double pulse testing with function generators details recommended DPT setups, waveform generation, and energy measurement practices [16].

2.3 Compact Heating Unit Designs and Modifications

Inexpensive SMD hot air rework stations like the 858D are widely repurposed as heating elements for research setups. These devices use 700W heating coils and built-in thermocouples for basic thermal regulation[17]. However, the original control logic often suffers from temperature overshoot, slow response, and non-linear control behavior.

Enbewe[18] reverse-engineered the Saito 858D rework station and found significant control loop limitations. Overshoot exceeding 50°C was observed, which is unacceptable for precision power device testing. To overcome this, various researchers have implemented Arduino-based PID control systems, enhancing stability and resolution. These controllers utilize solid-state relays and RTD feedback to maintain setpoints with tolerances below $\pm 1^\circ\text{C}$.

Compared to commercial thermal forcing systems, these modified units offer a balance between cost, size, and control accuracy. While lacking rapid cooling or sub-

zero capabilities, they meet the requirements for characterizing high-temperature switching behavior in WBG devices like SiC.

2.4 Temperature Sensing and Digital PID Control

High-fidelity temperature measurement is crucial for thermal control. Resistance Temperature Detectors (RTDs), especially PT100 or PT1000 sensors, provide accurate and stable readings over a wide range. The MAX31865 RTD-to-digital converter is widely used in embedded applications due to its compatibility with 2-, 3-, and 4-wire RTDs and SPI interface[19].

In power electronics labs, real-time temperature data is fed into PID controllers implemented on microcontrollers such as Arduino Mega or STM32. Proper tuning of the PID gains (K_p , K_i , K_d) enables fast settling and minimal overshoot. Non-blocking temperature readout routines are preferred to maintain responsiveness, especially during PWM updates.

Literature reports successful implementation of PID control for reflow ovens, 3D printer beds, and hot air systems. In each case, thermal inertia, ambient influence, and sensor placement significantly affect stability[20]. Feedforward elements and safety thresholds are often incorporated to avoid thermal runaway.

The integration of a GUI-based control interface (via Python and PyQt5) allows dynamic setpoint control, sensor selection, and real-time plotting. This further enhances usability in experimental setups for switching loss characterization.

2.5 Research Gap and Contribution

While literature offers extensive discussion on DPT methods and thermal effects on SiC MOSFETs, very few studies provide an end-to-end solution combining:

- A digitally-controlled compact heating unit,
- RTD-based sensing with MAX31865,
- Embedded PID logic with Arduino,

- and integration with a dynamic measurement station.

This thesis contributes by designing and validating such a system, tailored for systematic switching loss evaluation under thermal variation, with cost-effective and reproducible methods.

Chapter 3

Reverse engineering of RS PRO rework station



Figure 3.1: RS PRO Rework Station [1].

The RS PRO SMD Rework Station is a 700W dual-function unit combining a soldering iron and a hot air gun, both with independent temperature control and digital displays. The hot air system offers adjustable airflow up to 120L/min and a temperature range of 100–450°C, making it ideal for desoldering SMDs like QFP and SOP, heat shrinking, and preheating tasks. This compact, versatile station supports precise thermal control during electronic repair and prototyping activities in this thesis.

3.1 Finding Traces

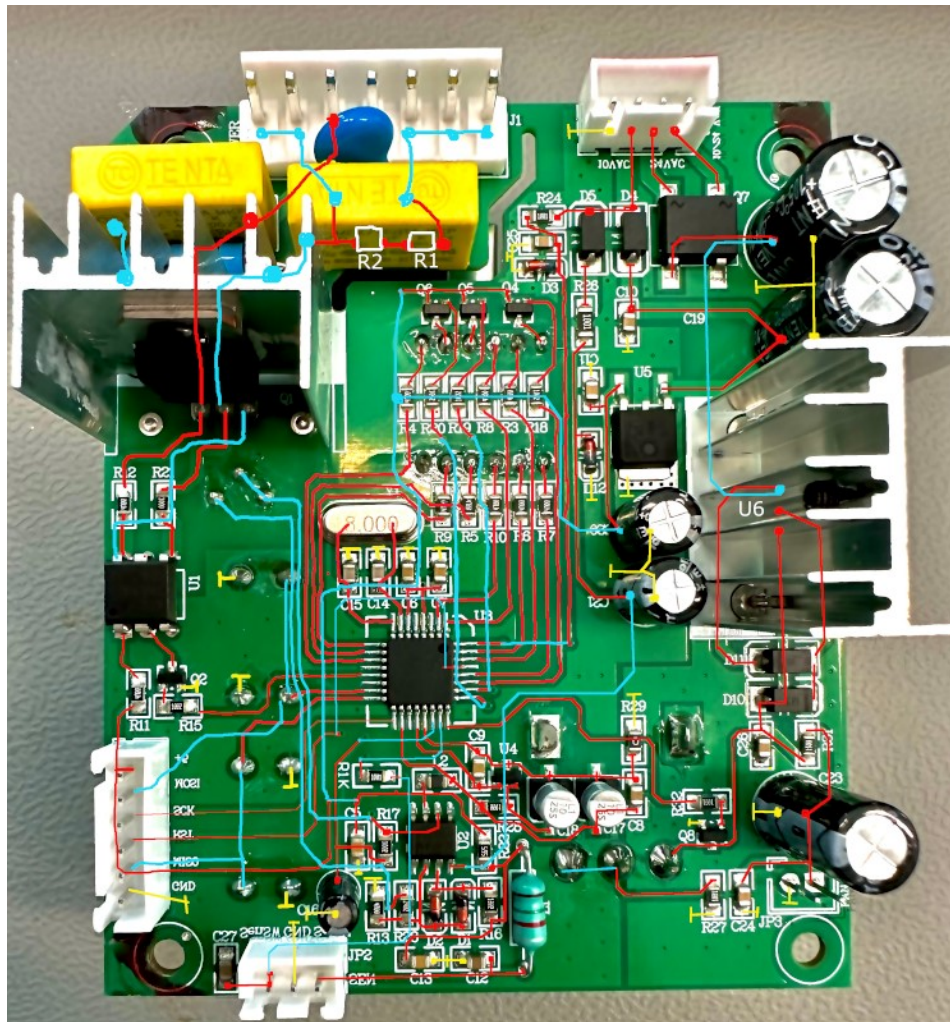


Figure 3.2: After finding traces using GIMP tool

To begin the reverse engineering process of the internal electronics, GIMP software was used to manually trace the PCB (Printed Circuit Board) routing from a detailed image of the board. This approach allowed me to visually map out the electrical connections and served as a valuable first step in reconstructing the schematic diagram of the main PCB using Autodesk Eagle.

Figure 4 shows the top view of the internal PCB after the routing lines were traced. In this figure, the power lines are highlighted in red and the ground connections

in blue, making the overall structure of the board easier to understand and interpret. Alongside this, compiled a basic Bill of Materials (BOM) by examining the components mounted on the board. This list includes component values and types, which not only helped verify the schematic but also improved my understanding of how the circuit functions.

3.2 Schematics

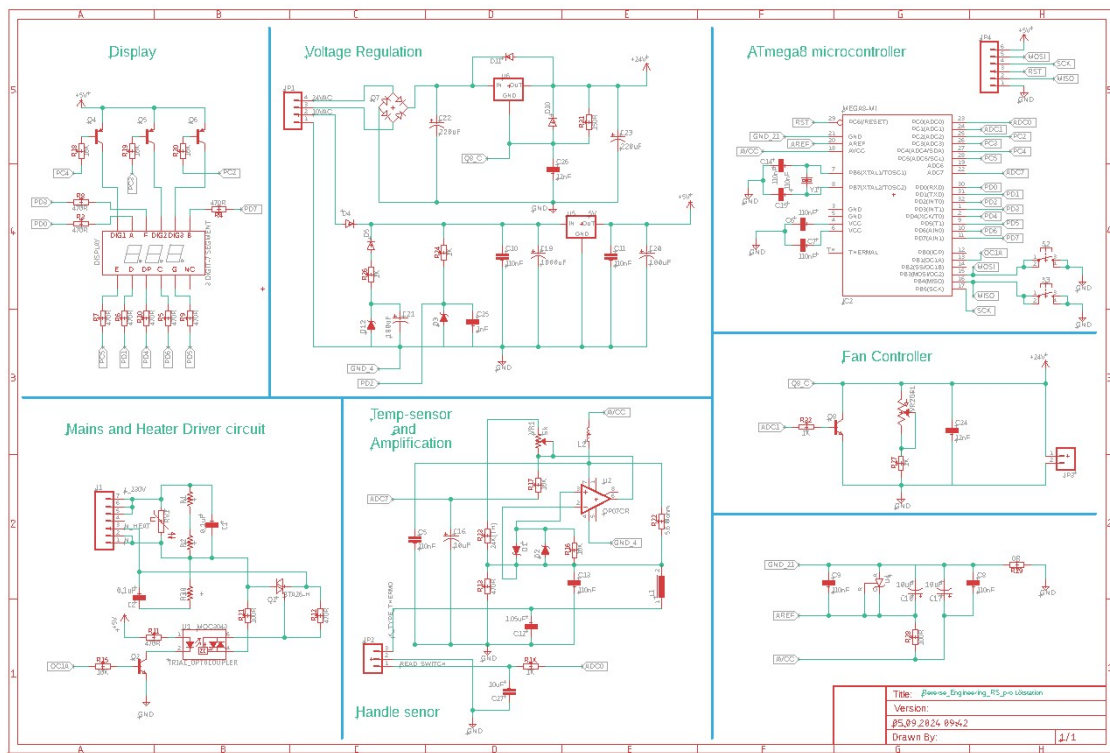


Figure 3.3: System schematics overview

The schematic depicts the design of a soldering station, incorporating key subsystems for temperature regulation, safety, and efficient operation. The ATmega8 microcontroller serves as the central control unit, interfacing with modules such as the display, heater driver, temperature sensing, and fan control circuits. A voltage regulation circuit converts the AC mains supply to regulated 5V and 24V DC to power the system components. The heater driver circuit uses an optoisolator and

a triac to control high-power AC loads while maintaining electrical isolation for safety. The temperature sensing circuit, using a thermocouple or thermistor and operational amplifiers, provides precise feedback for temperature regulation. A handle sensor with a reed switch detects user interaction, enabling energy-saving features such as auto-sleep. The fan controller regulates cooling to maintain the system's thermal stability.

3.3 Atmega Microcontroller

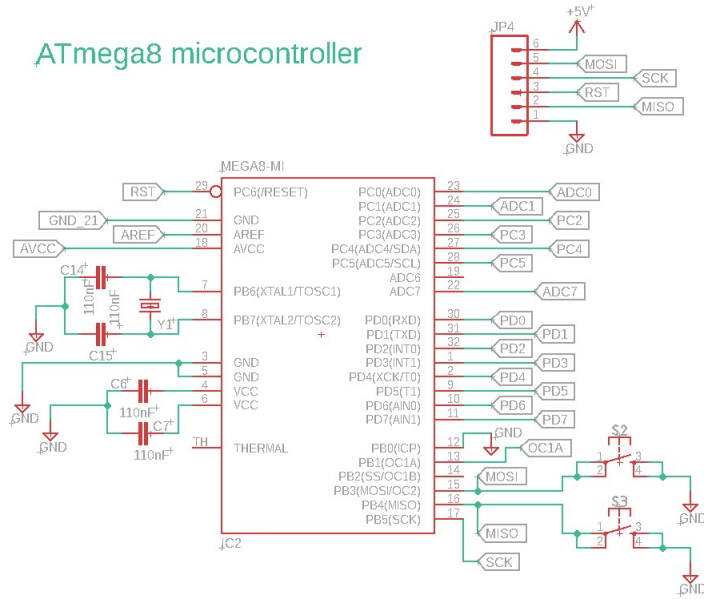


Figure 3.4: ATmega microcontroller block

This section illustrates the ATmega8 microcontroller interfacing with peripheral components. It includes clock circuitry with an external crystal oscillator, reset configuration, and an SPI header (JP4) for programming. The microcontroller receives regulated power via VCC and AVCC, and manages digital I/O lines for control, sensing, and communication. Its primary function is to coordinate temperature regulation, handle user inputs, process sensor data, and control the display, heater, and fan systems, acting as the central processing unit of the soldering station.

3.4 Voltage regulation

The voltage regulation circuit converts an AC input into stable DC outputs required by the system. It uses a bridge rectifier and smoothing capacitors to generate unregulated DC, followed by linear regulators to produce isolated +24V and +5V rails. These supply power to high-load components such as the heater and fan, as well as sensitive control circuitry like the microcontroller. Filtering and protection components are included to ensure safe, noise-free operation, forming the electrical backbone of the soldering station.

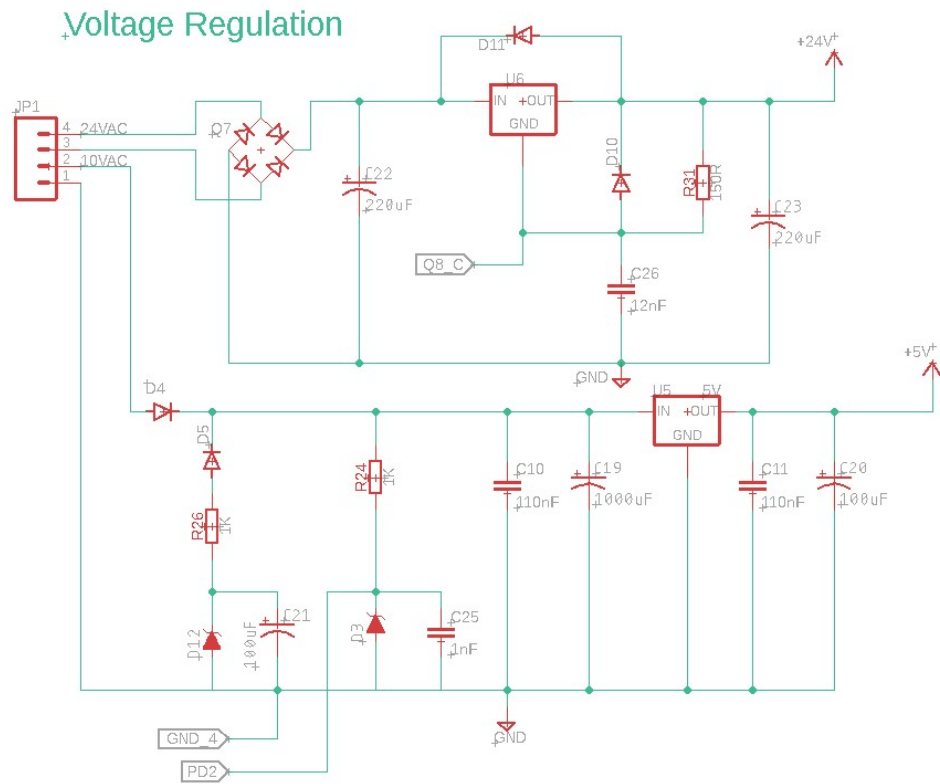


Figure 3.5: Voltage regulation circuit

3.5 Mains and Heater driver Circuit

The mains and heater driver circuit is responsible for switching the high-voltage AC supply to the heater element, enabling precise thermal control within the sol-

dering station. At its core, the design incorporates an opto-isolated triac driver (opto-triac) to ensure galvanic isolation between the microcontroller and the 230V AC mains supply, enhancing user safety and protecting low-voltage control circuitry. The microcontroller provides a control signal (OC1A), typically a PWM waveform, which activates the internal LED of the optocoupler. This, in turn, triggers the gate of a triac, allowing AC power to flow to the heater when required. Passive components such as resistors, capacitors, and a snubber network are used to shape and protect the triggering circuit, ensuring stable operation and suppressing voltage transients. Overall, this circuit ensures safe, electrically isolated, and efficient switching of the heater, forming a key functional block in the temperature regulation system of the rework station.

Mains and Heater Driver circuit

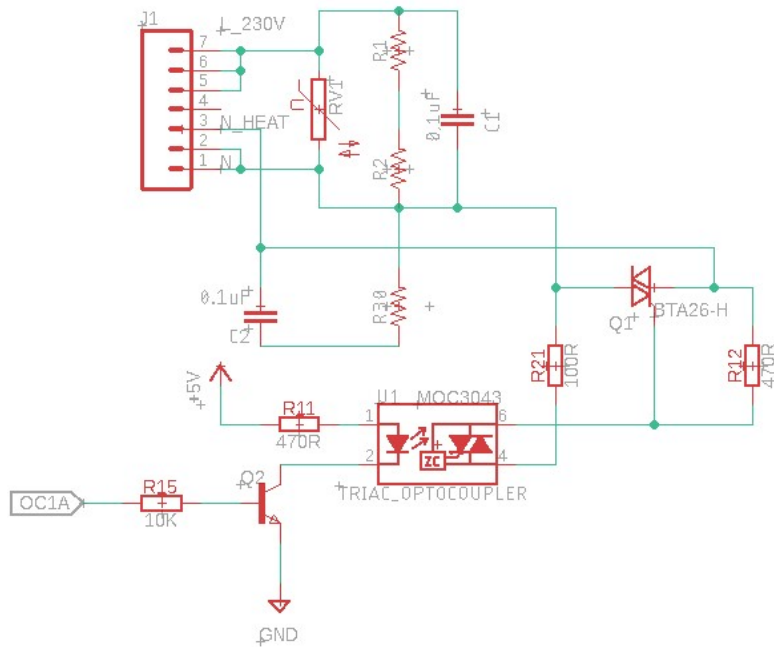


Figure 3.6: Heater driver circuit

3.6 Temperature sensor & Amplification, and Handle sensor

This circuit processes signals from a K-type thermocouple, using an operational amplifier to amplify the small voltage generated by temperature changes. The filtered and amplified signal is fed to the microcontroller's ADC for precise measurement. Additionally, a reed switch in the handle sensor enables user detection for energy-saving features like auto standby.

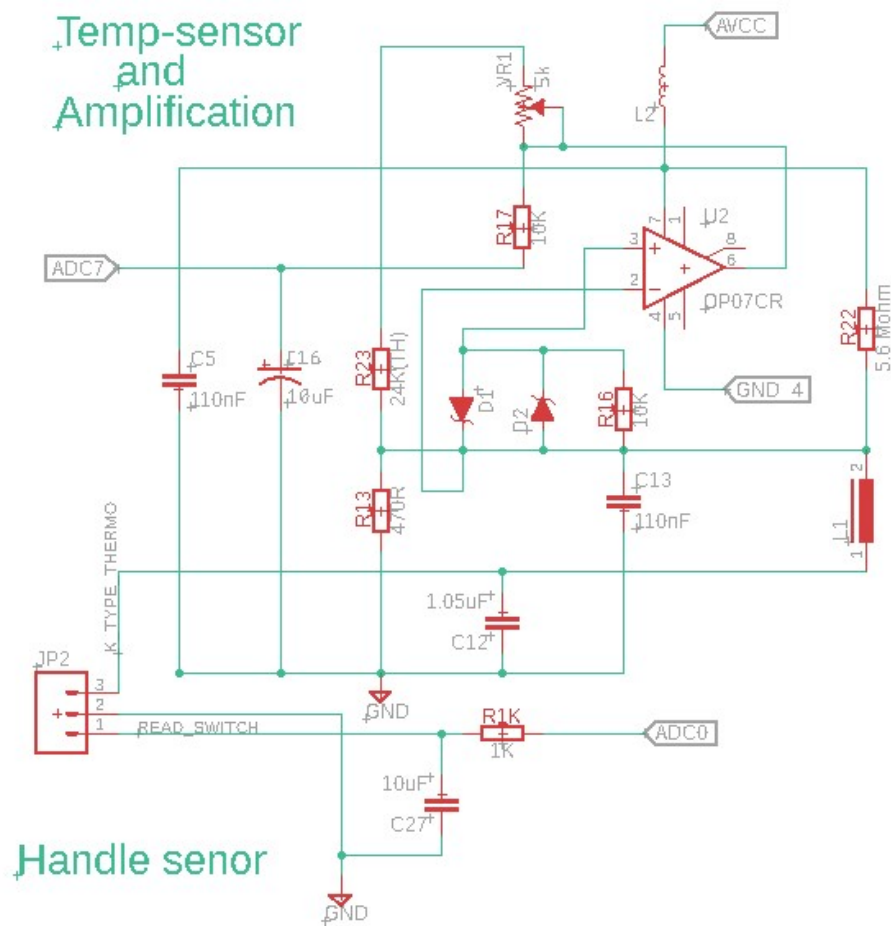


Figure 3.7: Temperature amplification and handle sensor

3.7 Fan Controller

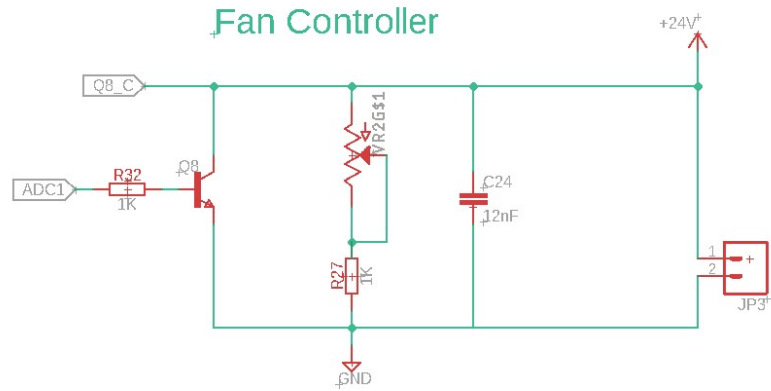


Figure 3.8: Fan controller circuit

The fan controller circuit enables variable speed control of a 24V fan using a PWM signal from the microcontroller via ADC1. A transistor acts as a switch to On and OFF fan power, the power flow through fan is controlled by a potentiometer manually, while passive components ensure signal stability and noise filtering. The fan performs two essential functions: first, to cool down and prevent thermal buildup, and second, to direct hot air toward the Device Under Test (DUT) or target object during soldering. This dual-purpose operation supports both system reliability and functional heating performance.

3.8 Circuit for Analog Reference

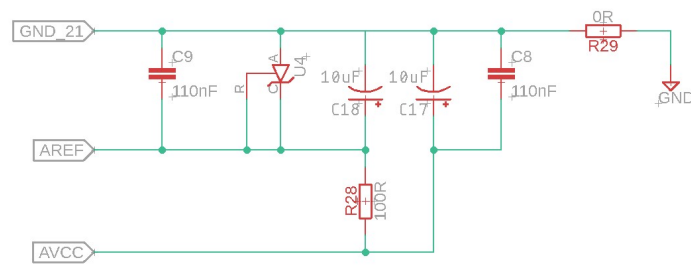


Figure 3.9: Analog reference circuit

This analog reference circuit filters and stabilizes the AVCC and AREF lines for the microcontroller's ADC, ensuring accurate and noise-free analog-to-digital conversion by using decoupling capacitors and isolation resistors.

3.9 Display

This circuit drives a multiplexed 3-digit 7-segment display using transistor switches and current-limiting resistors, enabling the microcontroller to show real-time parameters such as temperature, status codes.

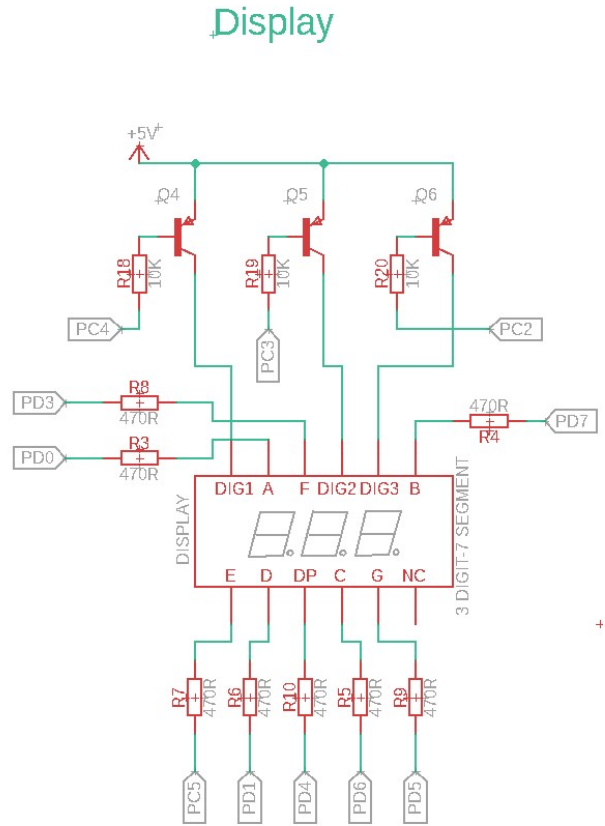


Figure 3.10: 7-segment display circuit

Chapter 4

Design and Development of the Digital Temperature Control System – First Prototyping Phase

In the initial phase of prototyping, the decision was made to replace the built-in ATmega8A microcontroller on the main PCB with an external microcontroller. The Arduino Mega was selected due to its compatibility with the Arduino IDE, which enabled efficient testing and development of entirely new firmware implementations.

Major functional blocks such as the voltage regulation circuitry, the heater driver, and the fan controller were retained from the original rework station's main PCB. Since the system's primary objective is to regulate the desired temperature at the Device Under Test (DUT), it was essential to establish a reliable feedback mechanism. For this purpose, a PT1000 sensor was mounted directly onto the DUT. This sensor provides an analog signal corresponding to the DUT temperature, which is crucial for closed-loop control.

The analog signal from the PT1000 is interfaced with the microcontroller using a MAX31865 RTD-to-digital converter and signal conditioning amplifier. This digitized temperature signal serves as the reference input for a PID controller, which subsequently generates a PWM signal to control a triac-based power driver. The triac modulates the power delivered to the heating element based on the

control loop's output.

This section will further detail the integration and configuration of the MAX31865 module with the PT1000 sensor, the interfacing between the Arduino Mega and the original PCB components, the experimental setup, the developed control block diagram, and selected preliminary results.

4.1 Configuration of the MAX31865 module with the PT1000 sensor

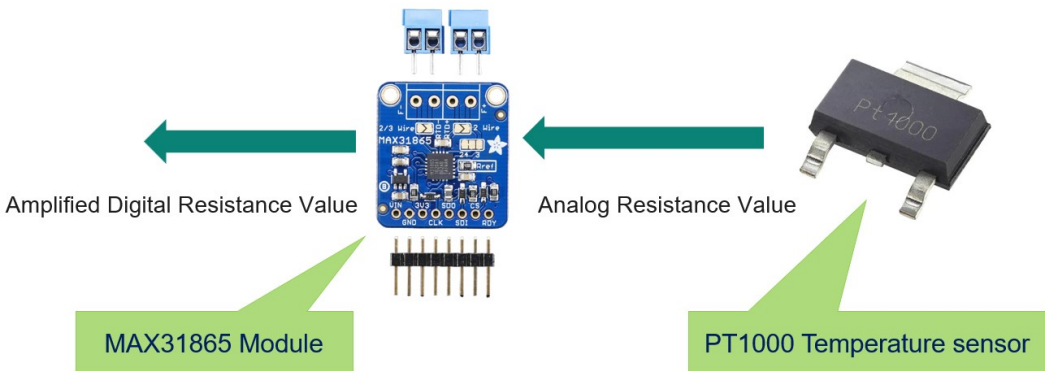


Figure 4.1: MAX31865 with PT1000 sensor[2].

The MAX31865 is a high-accuracy RTD-to-digital converter specifically designed to interface with platinum resistance temperature detectors such as the PT1000. The PT1000 sensor varies its resistance with temperature, and this analog resistance is precisely read and digitized by the MAX31865 using an internal precision reference resistor and amplifier. The module supports multiple wiring configurations (2-, 3-, or 4-wire), allowing compensation for lead resistance, which improves accuracy in practical setups. Communication with the microcontroller is achieved through the SPI protocol, enabling reliable retrieval of processed digital temperature values for integration into closed-loop control systems.

4.2 Interfacing between the Arduino Mega and the original PCB

As part of the system redesign, the original onboard ATmega8A microcontroller was substituted with an Arduino Mega 2560, as illustrated in Figure 4.2. The Arduino offered broader compatibility, a user-friendly development environment, and easier firmware iteration. Electrical interfacing between the Arduino and the original PCB was achieved using jumper wires, with signal mapping performed to identify and connect compatible pins. The use of a custom Arduino shield simplified the integration by providing a structured platform for wiring and mechanical support. Additionally, the MAX31865 module was connected to the Arduino via SPI, using dedicated high-reliability cables designed to reduce noise and ensure stable data transmission. This modular arrangement allowed rapid prototyping and simplified debugging during early development stages.

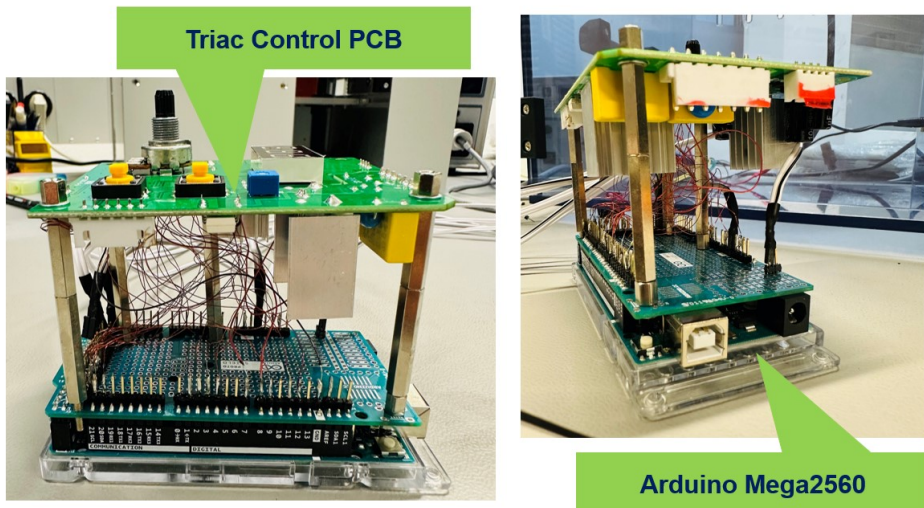


Figure 4.2: Interfacing Arduino Mega and the main PCB

4.3 Experimental setup

The experimental setup, as shown in Figure 4.3, was designed to evaluate the thermal control system and its integration with the DUT. A hot air gun was posi-

tioned vertically above the DUT to provide controlled heating, while a PT1000 sensor mounted on the DUT ensured accurate temperature feedback. The MAX31865 module, located near the DUT (not visible in the image), digitized the analog temperature signal and transmitted it via SPI cables to the Arduino Mega. A K-type thermocouple connected to a handheld thermometer was used for cross-verification of the DUT temperature in real time. To ensure operator and equipment safety, the entire system was enclosed in a protective safety box, and an isolation transformer was used to prevent potential back-feed to the mains grid. The Arduino was connected to a PC through USB for flashing firmware and real-time data monitoring via the Arduino IDE. During testing, a logic analyzer monitored digital signal transitions, while an oscilloscope was used to observe the output waveform of triac and PWM behavior. This setup enabled controlled thermal experiments under safe laboratory conditions.

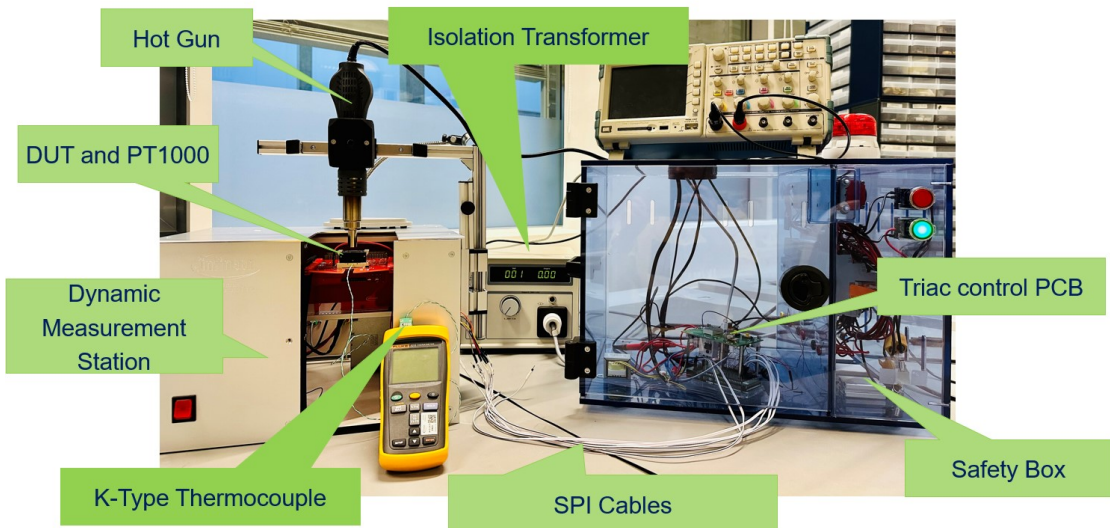


Figure 4.3: Experimental setup

4.4 Control block diagram

The control block diagram shown in Figure 4.4 illustrates the overall operation of the temperature regulation system. The user initiates commands via the Arduino IDE on a personal computer, including parameters such as the temperature

setpoint, fan speed, and PID constants for tuning. The PT1000 sensor, mounted on the DUT, provides real-time temperature data, which is converted into a digital signal by the MAX31865 module and transmitted to the microcontroller unit (MCU). The onboard PID algorithm compares the setpoint with the feedback and calculated error, then generates a PWM signal that drives the triac-based power control circuit. This triac regulates the heating element's power delivery accordingly. Output variables—such as actual temperature, PWM values, PID parameters, error and system status—are visualized using the IDE's serial monitor and plotter. This closed-loop arrangement enables effective temperature tracking and fine-tuning during experimental analysis.

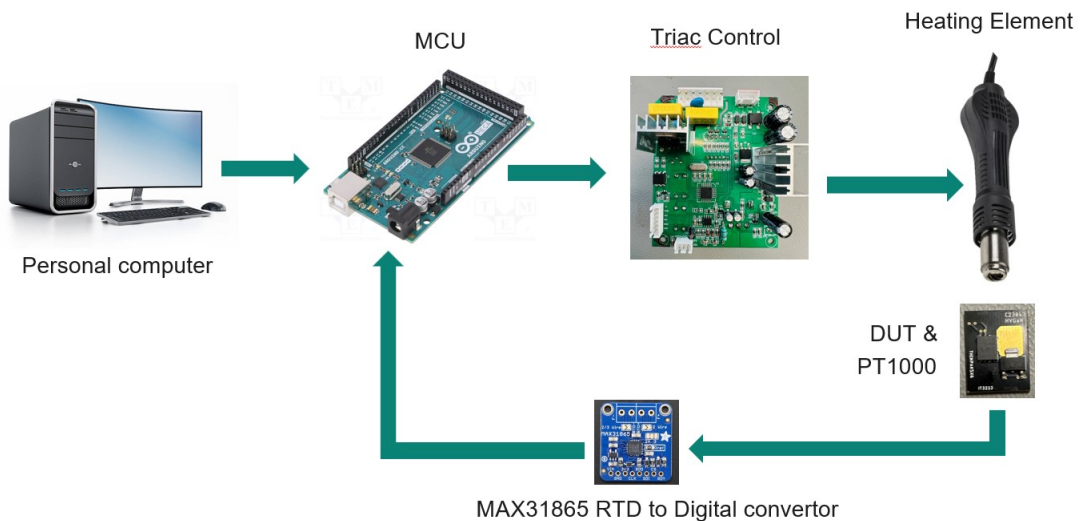


Figure 4.4: Control block diagram

4.5 Preliminary results obtained

Figure 4.5 illustrates a output captured using the Arduino Serial Plotter. The graph shows the system response as the temperature rises from ambient conditions and approaches the defined setpoint of 100°C. After reaching the target value, the actual temperature (CT) exhibits damped oscillations around the setpoint (ST), which is a typical behavior during the settling phase of a PID-regulated control system. Due to limitations of the Serial Plotter, the initial warm-up phase is not

fully visible in the plot. Despite this, the oscillatory nature of the control response provides valuable insights into PID tuning performance and system thermal inertia.

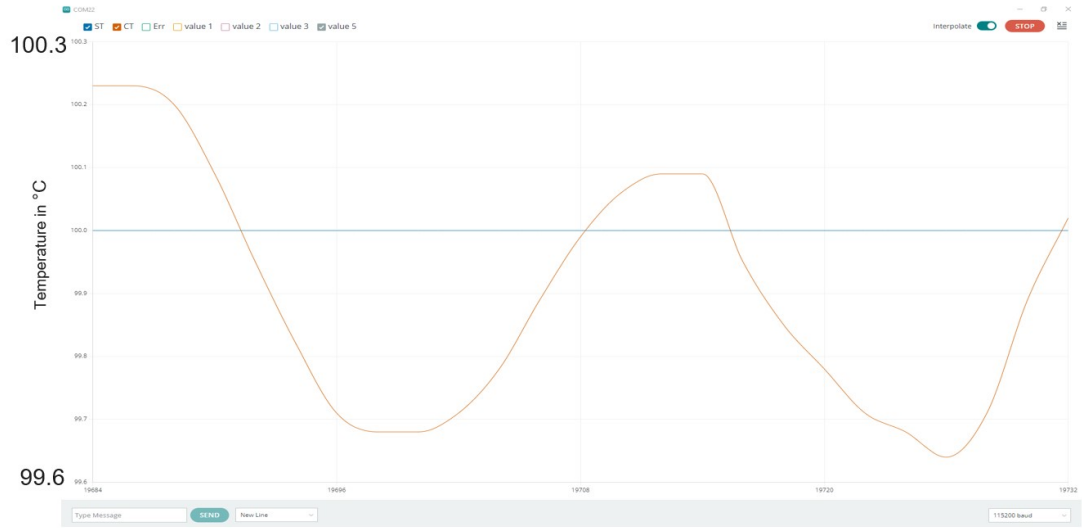


Figure 4.5: settled temp at 100°C line with oscillations

In another test scenario, as shown in Figure 4.6 the system successfully stabilized the DUT temperature at the defined setpoint of 100°C, with the corresponding error line consistently converging near zero. This demonstrates the PID controller's effectiveness in achieving steady-state regulation with a tolerance of approximately $\pm 1^{\circ}\text{C}$. The experimental setup was capable of regulating temperatures across a broad range from ambient up to 200° allowing for diverse thermal testing conditions. This foundational experiment not only confirmed the prototype's reliability but also provided valuable insight into control response dynamics, system behavior, forming the basis for future enhancements and parameter optimization.

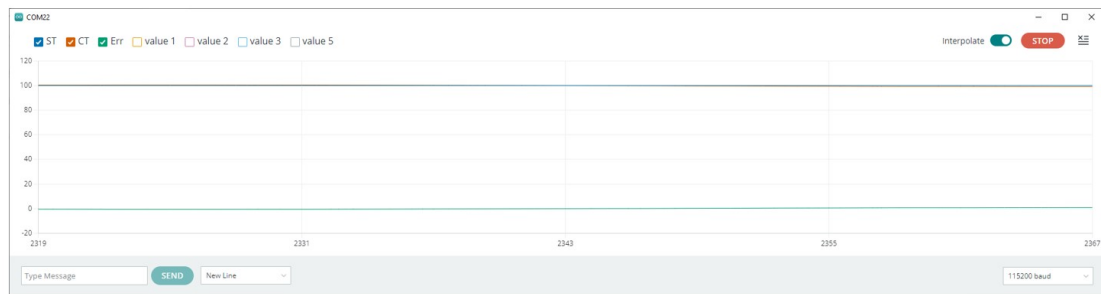


Figure 4.6: Settled temp at 100°C line with error convergence and tolerance

Chapter 5

Design and Development of the Digital Temperature Control System – Second Prototyping Phase

In this chapter, the design and development of the second prototype of a digital temperature control system are presented. This phase involved creating a custom Arduino-compatible PCB integrating key components such as the MAX31865 for RTD sensors, MAX31855 for thermocouples, and a relay-based protection circuit. Alongside hardware development, a Python-based GUI was introduced for real-time temperature monitoring and control. Special attention was given to PID tuning across various thermal scenarios. Key improvements, like non-blocking temperature reading and dual sensor compatibility, were implemented to ensure stable and responsive performance during dynamic heating experiments.

5.1 The new PCB contains MAX31865, MAX31855 and Protection Circuit

A custom PCB was developed to integrate multiple essential circuits, including the MAX31865 for RTD sensing, the MAX31855 for K-type thermocouple input, and a dedicated over-temperature protection circuit. The design is Arduino Mega-

compatible, replicating the official Adafruit reference circuits for reliable sensor interfacing.

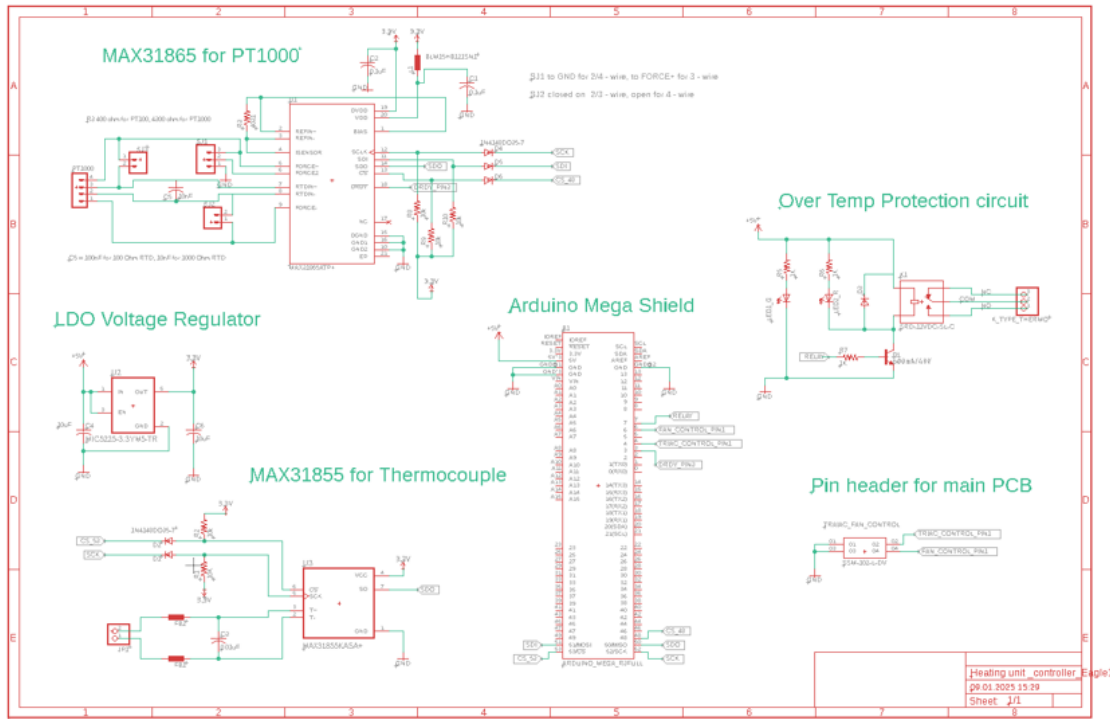


Figure 5.1: New Schematic for Arduino compatible PCB

A 3.3V LDO regulator supplies both MAX ICs. The protection circuit includes a normally open relay rated for 230V, 5A, offering thermal isolation. A pin header was added for carrying PWM control signals to the main PCB from controller PCB. The board layout was created in Eagle and fabricated as a single-sided PCB. Manual component placement and soldering ensured precise assembly. The modular layout enables easy maintenance and future expansion.

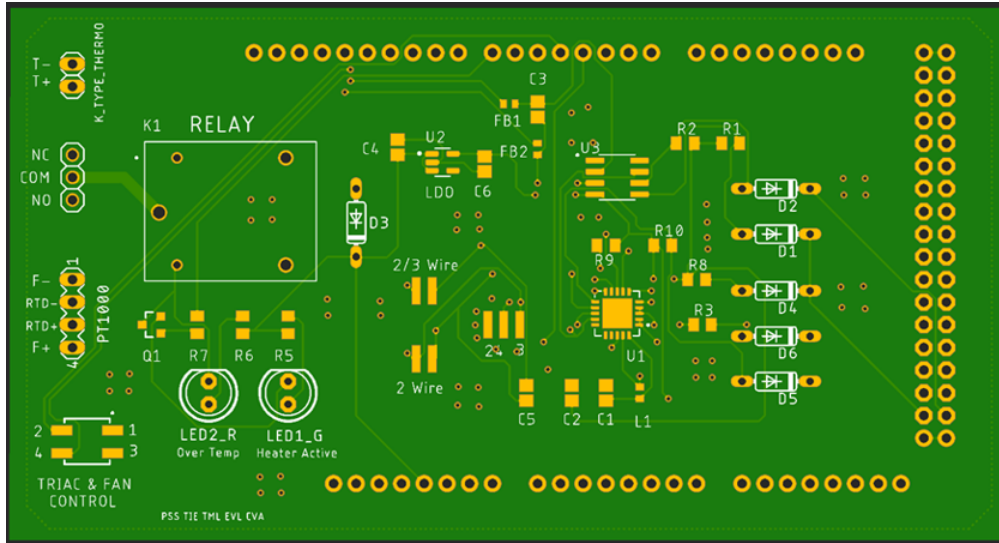


Figure 5.2: Controller PCB Top view

5.2 New Arduino Compatible PCB

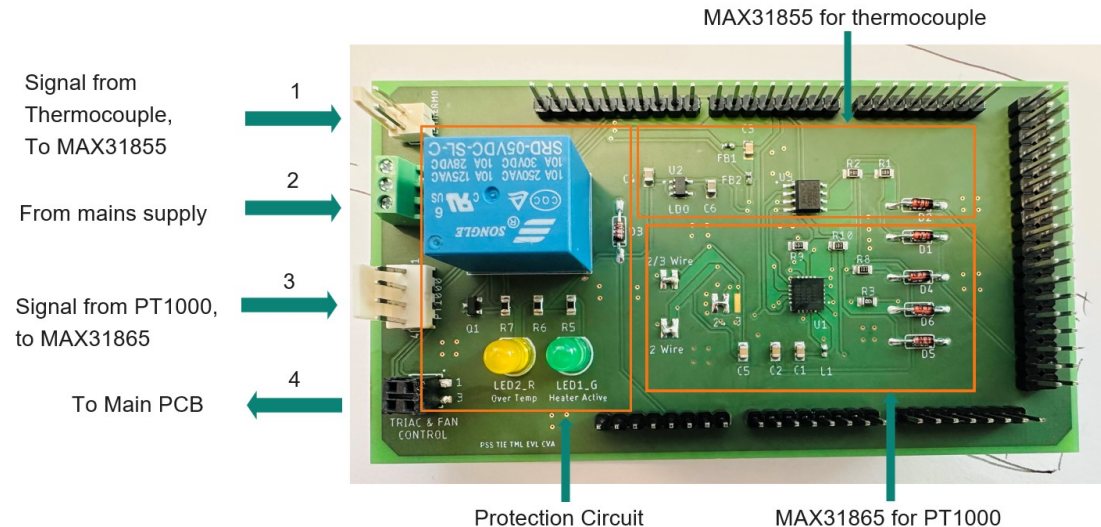


Figure 5.3: New Arduino compatible PCB

The newly designed Arduino-compatible PCB, shown in Figure 5.3, combines three main circuits: the MAX31865 for PT1000 sensors, the MAX31855 for thermocou-

ples, and a relay-based protection circuit. On the left side, four pin headers are used for specific tasks—one connects the thermocouple to the MAX31855, another links the relay to the mains power, the third sends the PT1000 signal to the MAX31865, and the fourth carries PWM signals to the main PCB for controlling the fan and heater. Long pin headers match the Arduino layout and make testing easier with tools like oscilloscopes or logic analyzers.

5.3 Adapter that Connects Main PCB to Controller

To interface the new controller PCB with the original main board, a compact adapter PCB was designed. The bottom side of the adapter matches the footprint of the original ATmega8A IC, allowing it to fit directly into its place. The top side provides four solder pads—two for ground, one for the triac control signal, and one for the fan control. This adapter allowed easy connection between the main PCB and the controller using a simple 4-core cable.

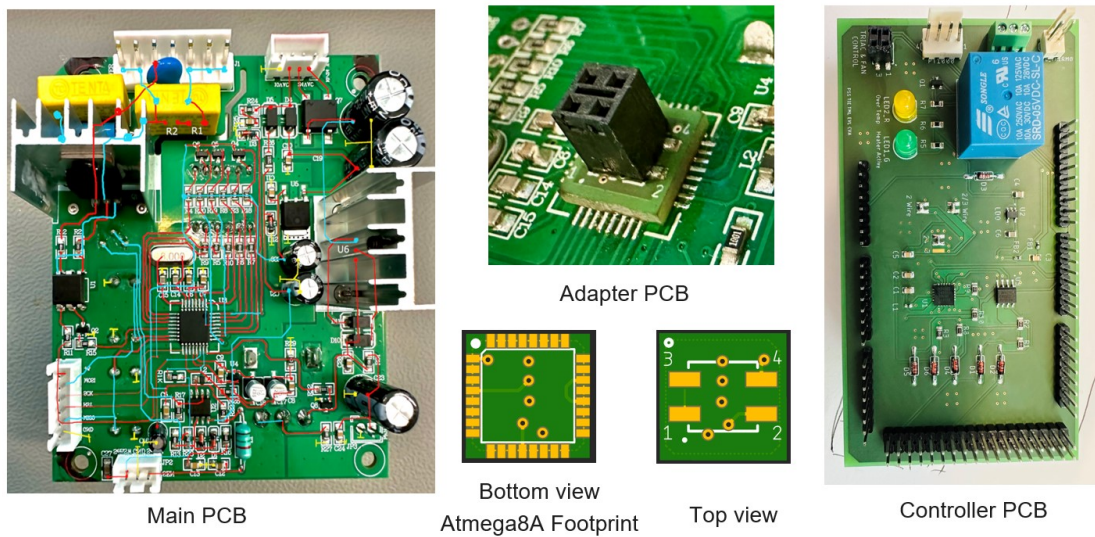


Figure 5.4: Adapter PCB to interface controller and main board

5.4 Delays in Adafruit MAX31865 Library

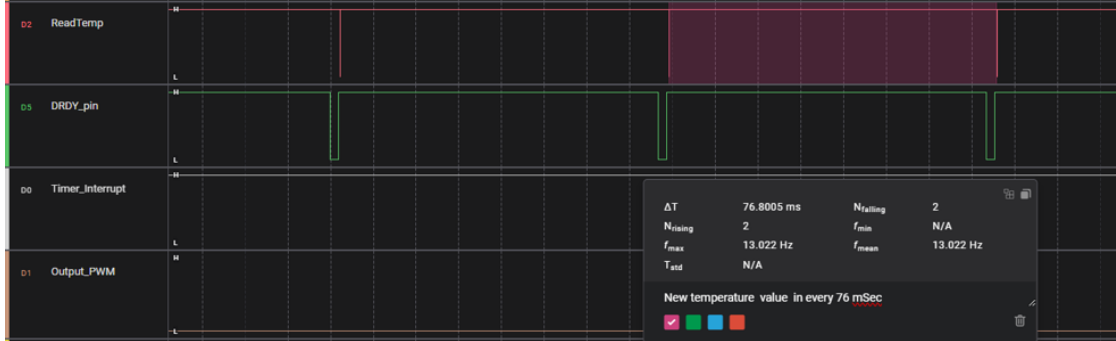


Figure 5.5: Delay section in Adafruit MAX31865 library[3].

During system testing, it was observed that the default delays in the Adafruit MAX31865 library available on GitHub limited the update rate of temperature readings. As shown in the code snippet (Figure 5.6), the function `readRTD()` includes two fixed delays: 10 ms and 65 ms. These delays are required for bias stabilization and RTD conversion, respectively. The logic analyzer output (Figure 5.5) confirms that a complete temperature read cycle takes approximately 76 ms. This delay directly affects how quickly new temperature values are available, and in turn, how frequently the PID loop can update the PWM output. Reducing this delay could improve system responsiveness, especially when maintaining tight temperature tolerances like $\pm 1\text{C}$.

```
uint16_t Adafruit_MAX31865::readRTD(void) {
    clearFault();
    enableBias(true);
    delay(10);
    uint8_t t = readRegister8(MAX31865_CONFIG_REG);
    t |= MAX31865_CONFIG_1SHOT;
    writeRegister8(MAX31865_CONFIG_REG, t);
    delay(65);
    uint16_t rtd = readRegister16(MAX31865_RTDMsb_REG);

    enableBias(false); // Disable bias current again to reduce
selfheating.
    // remove fault
    rtd >>= 1;
    return rtd;
}
```

Figure 5.6: Code snippet from Adafruit library

5.5 Non-blocking Continuous Code

To solve the timing limitations caused by the standard Adafruit library, a custom non-blocking MAX31865 library was used, available on GitHub [21]. Unlike the original single-shot method, this version continuously reads temperature at a fixed rate of 50 Hz, delivering a new value every 20 milliseconds without using any `delay()` functions. The logic analyzer output in Figure 5.7 confirms this performance. This improvement allowed the control loop to react much faster, helping maintain a tighter temperature tolerance and better real-time response under dynamic conditions.

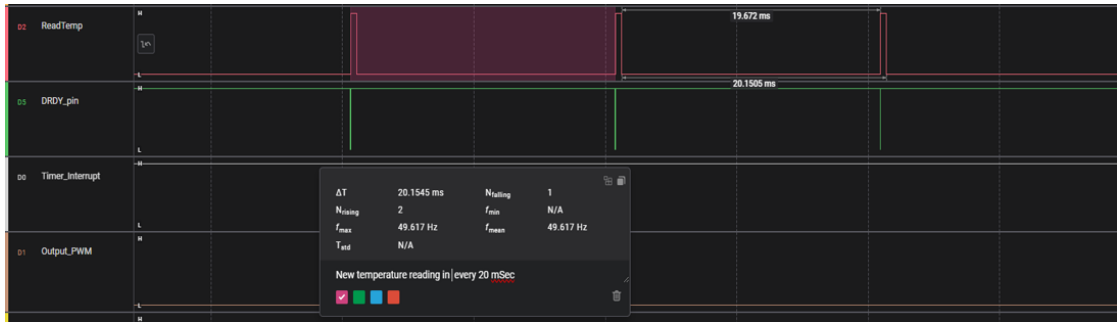


Figure 5.7: Non-blocking continuous mode verified using logic analyzer

5.6 Control Diagram

The updated control diagram in Figure 5.8 shows the complete operation of the improved temperature control system. Commands such as temperature setpoint, fan speed, and feedback source selection are sent from a custom-developed GUI running on a personal computer. The DUT is monitored using either a PT1000 sensor connected via the MAX31865 module or, if not available, a thermocouple linked to the MAX31855 module. This temperature data is sent to the microcontroller, which processes it using a PID algorithm and generates a PWM signal for triac-based power control. Additionally, a built-in thermocouple in the hot air gun is used for safety via a relay control mechanism in the firmware.

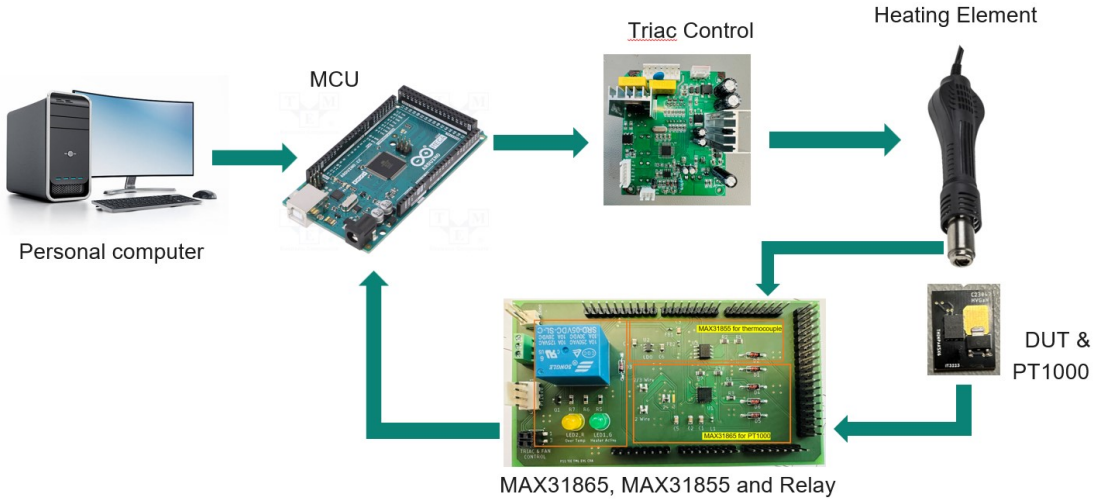


Figure 5.8: Updated control block diagram

5.7 Different Use Cases

Various real-world use cases were considered while developing the control logic, especially during PID tuning. Understanding the system's dynamic behavior under different physical conditions of Hotgun required significant time and effort. This step was crucial to achieving stable and responsive temperature control. Each scenario helped refine how the system responds to sudden changes or load variations, and the position of the Hotgun related to DUT directly influencing controller performance and tuning accuracy.

5.7.1 Case 1

In practical scenarios, the user may place the hot air gun at different positions—too close, too far, or at various angles relative to the DUT. This kind of changes can lead to uneven heating and impact the accuracy of temperature feedback. For optimal system performance, consistent alignment and positioning of the heat source should be maintained during all test conditions.

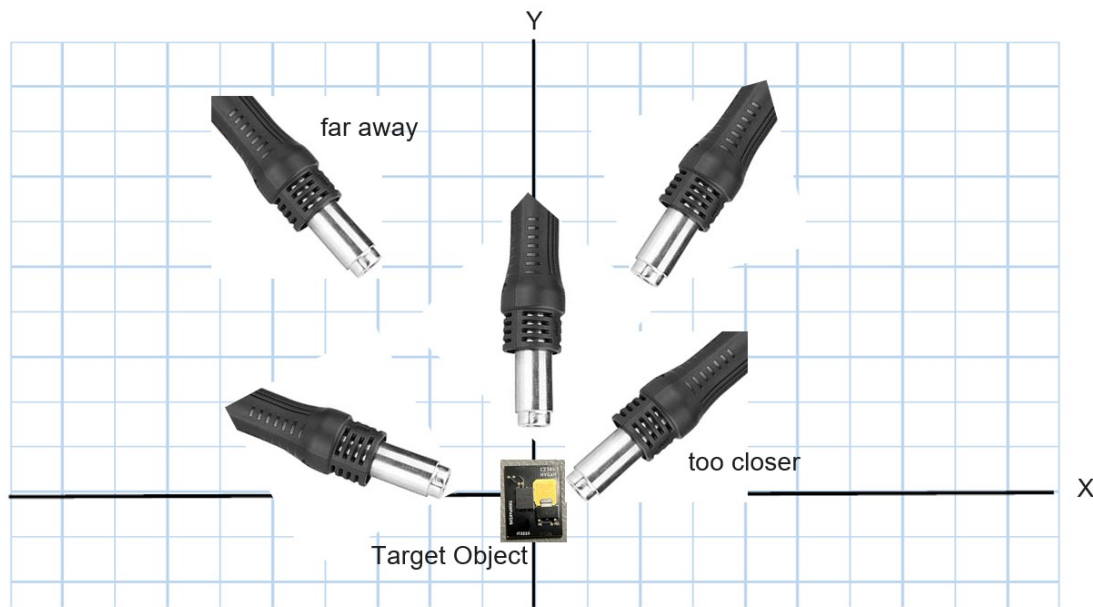


Figure 5.9: Hotgun placed in different position and angle

5.7.2 Case 2

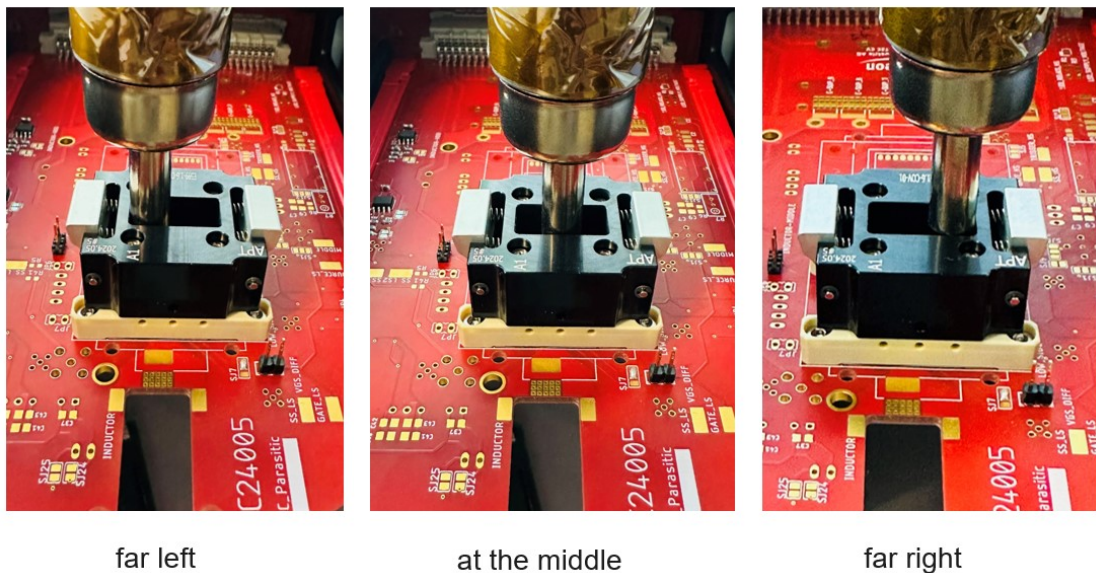


Figure 5.10: Hotgun placed in different horizontal positions over DUT

This setup on Figure 5.10 illustrates three different hot air gun positions horizontally—far left, center, and far right—above the DUT socket on the measurement board. Even small deviations in positioning may lead to uneven temperature distribution, making it necessary to adjust PID settings to achieve consistent and precise regulation.

5.7.3 Case 3

This case demonstrates how vertical distance between the hot air gun and DUT affects heating efficiency. When placed too far, insufficient heat may reach the target, especially at low fan speeds. Finding the right balance between distance and airflow is key for stable operation.

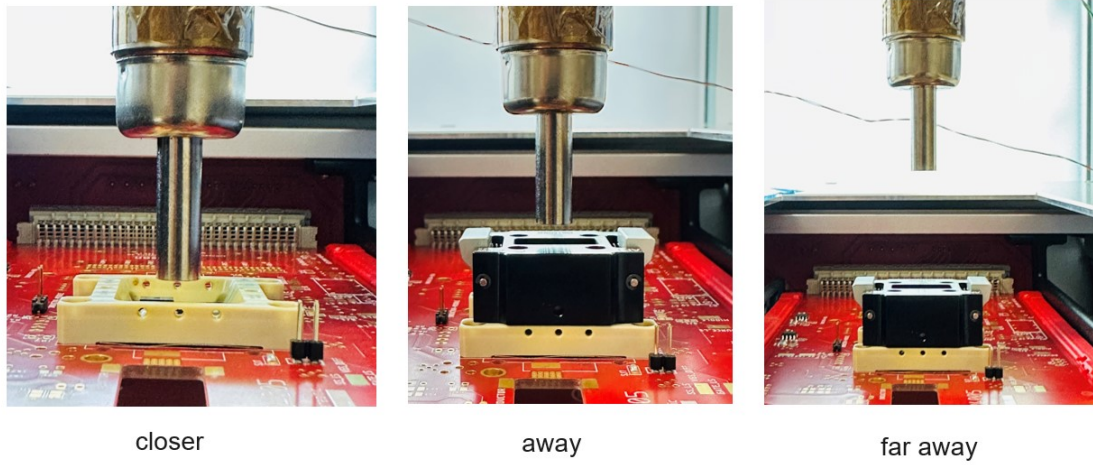


Figure 5.11: Hotgun placed in different vertical positions over DUT

5.8 PID Tuning: Trial and Error Method

5.8.1 Experiment Concept

The experiment was based on placing a scale on the hot air gun holder of the dynamic measurement station to define X and Y coordinates. As shown in Figure 5.12, the hot air gun was tested at different positions, and PID constants were

manually adjusted to achieve minimal overshoot and tried to maintain a tolerance of around $\pm 1\text{C}$. This tuning method was completely manual and took a lot of time and effort.

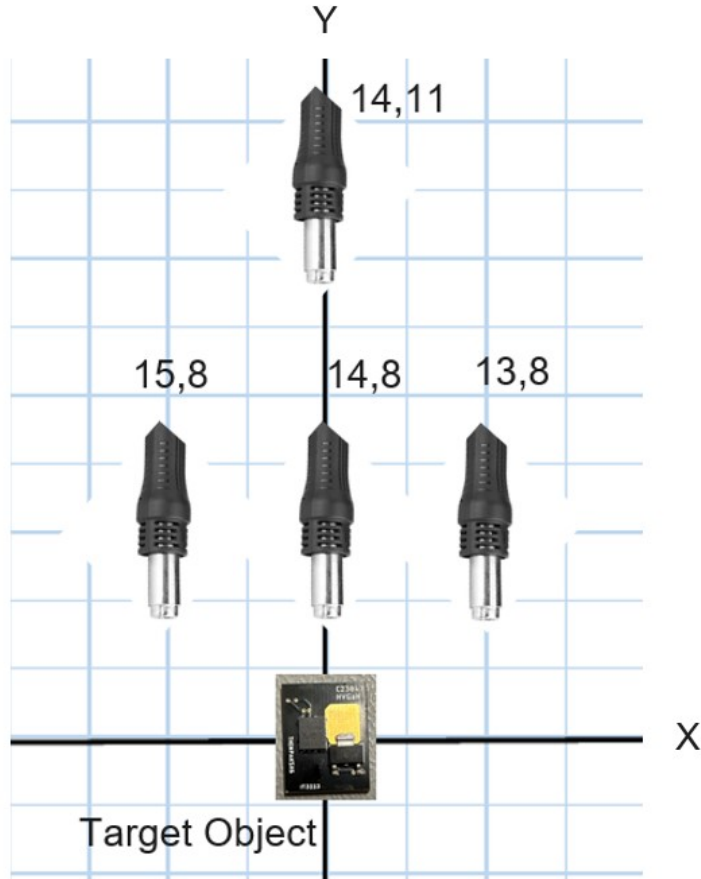


Figure 5.12: Hot air gun on X-Y grid for PID tuning trials

It was found that one set of PID constants could not be used across the entire temperature range; for example, values working at 25C did not work well at 250C . So, the temperature range was divided into zones, and suitable constants were identified for each. Another issue was that PID values found for PT1000 feedback did not work when using a thermocouple as feedback, and new constants had to be found for the thermocouple. Moreover, the thermocouple did not demonstrate the same level of stability and tolerance as the PT1000 sensor. Autotuning was tested but did not give reliable results. AI-based methods were also explored

briefly, but results were not promising—though they could be considered for future improvement.

5.8.2 Obtained Results

To better organize the outcomes of the PID tuning, the results are grouped by temperature ranges and formatted for improved readability. Each group reflects performance under specific ‘Setpoint’ ranges.

Table 5.1: PID Tuning Results Across Different Temperature Ranges

Setpoint ≥ 25 Setpoint ≤ 50

X,Y	Kp	Ki	Kd	Tolerance ($^{\circ}\text{C}$)	Overshoot Avg (%)	Overshoot ($^{\circ}\text{C}$)
14,8	10	10	10	toggle ± 1	10	5
14,9	10	10	10	toggle ± 1	10	5
14,10	10	10	10	toggle ± 1	10	5
14,11	10	10	10	toggle ± 1	10	5
13,8	10	10	10	toggle ± 1	14	7
13,9	10	10	10	toggle ± 1	8	4
15,8	10	10	10	toggle ± 1	14	7
15,9	10	10	10	toggle ± 1	12	6

Setpoint ≥ 51 Setpoint ≤ 80

X,Y	Kp	Ki	Kd	Tolerance ($^{\circ}\text{C}$)	Overshoot Avg (%)	Overshoot ($^{\circ}\text{C}$)
14,8	10	15	10	toggle ± 1	7	6
14,9	10	15	10	toggle ± 1	6	5
14,10	10	15	10	toggle ± 1	5	4
14,11	10	15	10	toggle ± 1	1	1
13,8	10	15	10	toggle ± 1	5	4
13,9	10	15	10	toggle ± 1	2	2
15,8	10	15	10	toggle ± 1	6	5
15,9	10	15	10	toggle ± 1	2	2

Setpoint ≥ 81 Setpoint ≤ 100

X,Y	Kp	Ki	Kd	Tolerance ($^{\circ}\text{C}$)	Overshoot Avg (%)	Overshoot ($^{\circ}\text{C}$)
14,8	15	80	80	toggle ± 1	5	5
14,9	15	80	80	toggle ± 1	4	4
14,10	15	80	80	toggle ± 1	1	1
14,11	15	80	80	toggle $+1,-2$	1	1
13,8	15	80	80	toggle ± 1	2	2
13,9	15	80	80	toggle ± 1	2	2
15,8	15	80	80	toggle $+1,-2$	4	4
15,9	15	80	80	toggle ± 1	7	7

Setpoint ≥ 101 Setpoint ≤ 155

X,Y	Kp	Ki	Kd	Tolerance ($^{\circ}\text{C}$)	Overshoot Avg (%)	Overshoot ($^{\circ}\text{C}$)
14,8	35	100	150	toggle ± 1	1	2
14,9	35	100	150	toggle ± 1	1	2
14,10	35	100	150	$+1,-2$	1	1
14,11	35	100	150	$+1,-2$	1	1
13,8	35	100	150	toggle ± 1	1	1
13,9	35	100	150	toggle ± 1	1	4
15,8	35	100	150	toggle ± 1	2	3
15,9	35	100	150	toggle $+2$ and -3	4	7

Setpoint > 155

X,Y	Kp	Ki	Kd	Tolerance ($^{\circ}\text{C}$)	Overshoot Avg (%)	Overshoot ($^{\circ}\text{C}$)
14,8	40	200	150	toggle $+1,-2$	1	2
14,9	40	200	150	toggle ± 1	1	1
14,10	40	200	150	toggle ± 1	1	2
14,11	40	200	150	toggle ± 1	1	2
13,8	40	200	150	toggle $+1,-2$	0	0
13,9	40	200	150	toggle $+1,-2$	0	0
15,8	40	200	150	toggle $+2,-3$	1	1
15,9	40	200	150	toggle $+1,-2$	1	3

5.9 Designing of GUI for Temperature Control and Monitoring—First Phase

The first phase of GUI development focused on creating a Python-based interface using Matplotlib for real-time temperature monitoring and control of the heating unit. Two example test cases are shown: one with PT1000 as the feedback sensor, regulating temperature from 25C to 50C in Figure 5.13, and another with a thermocouple, reaching 100C in Figure 5.14. The GUI allows the user to start and stop the system, set temperature setpoints, define safety thresholds, and adjust fan speed. A dynamic plot displays actual temperature (blue line) against the target setpoint (red dashed line), enabling immediate visual feedback on system performance.

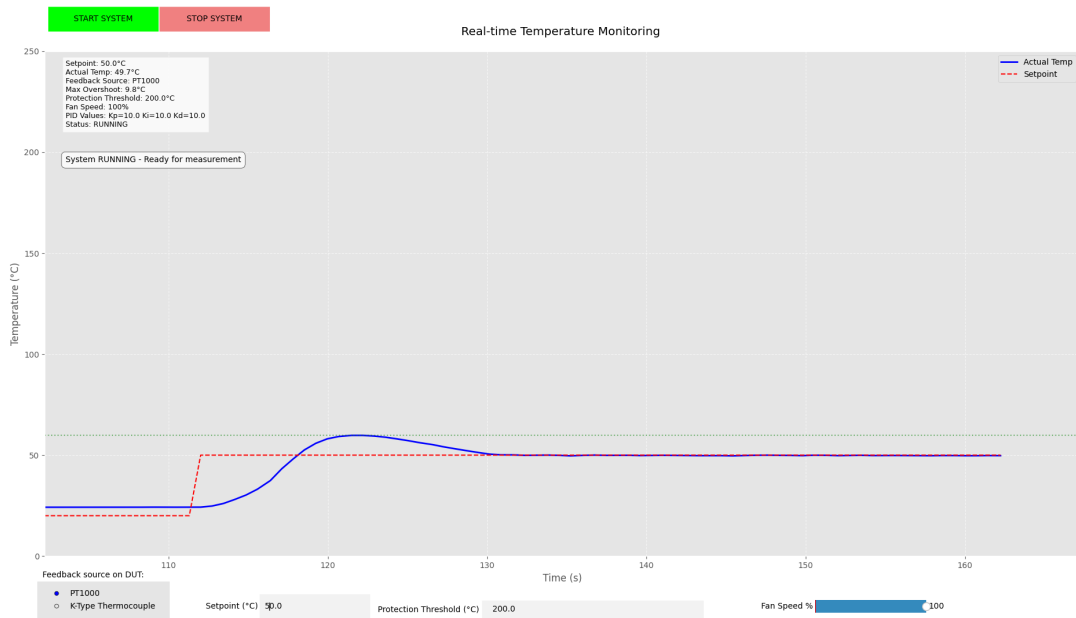


Figure 5.13: GUI test case with PT1000 sensor: 25C to 50C

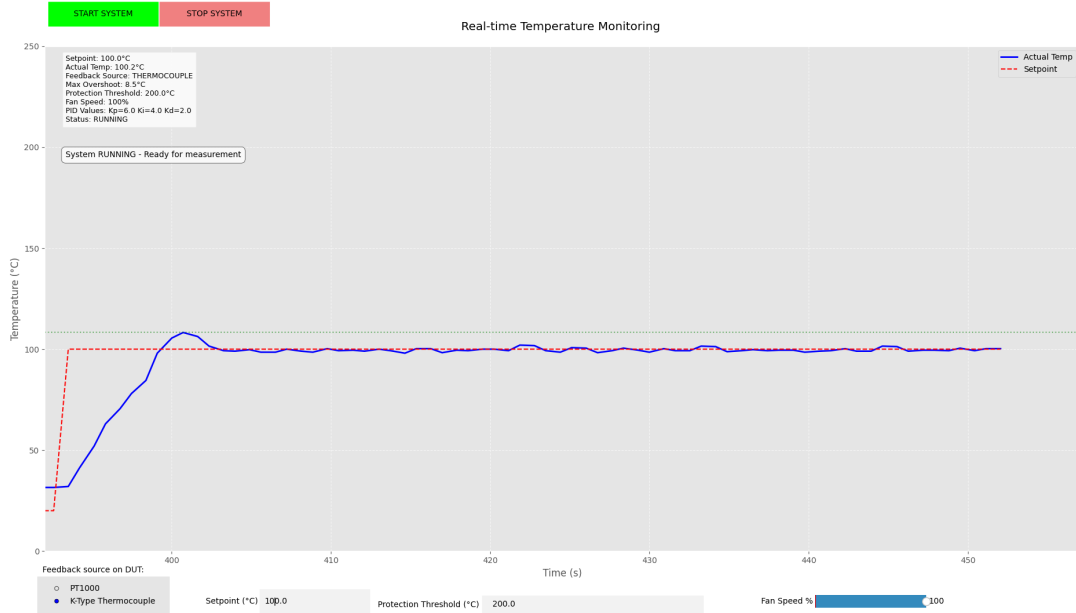


Figure 5.14: GUI test case with thermocouple: 25C to 100C

Real-time parameters such as system status (RUNNING, STOPPED), sensor source, PID values, maximum overshoot, and warning messages (like over-temperature or sensor failure) are also displayed. A sensor switch option allows the user to select between PT1000 and thermocouple inputs, depending on DUT configuration—particularly useful for DUTs without PT1000 mounting due to cost constraints. The GUI development process was accelerated with occasional assistance from AI-based coding tools. To support dual-channel communication, a USB-to-TTL cable was used, enabling simultaneous monitoring via both the GUI and Arduino IDE during testing and tuning.

Chapter 6

Design and Development of Digital Temperature Control Systems – New Python PyQt-based GUI

6.1 GUI Overview

The Arduino and Python GUI work together as a closed-loop digital temperature control system. The Arduino reads temperature data from either a PT1000 sensor or a thermocouple, processes it using a PID algorithm, and controls a heater and fan accordingly. It transmits real-time status data such as current temperature, setpoint, PID values, and system state to the PyQt5-based GUI via serial communication. The GUI visualizes this data on live plots and allows users to control parameters like setpoint, fan speed, and feedback source. User inputs from the GUI are sent back to the Arduino, enabling dynamic and safe system control.

The newly developed GUI, built using Python (PyQt5), acts as a central interface for both monitoring and controlling the digital temperature control system. It features a live temperature plot, where the blue line indicates the actual temperature of the DUT and the red dashed line shows the setpoint. This helps users visually track system response and stability. A system info panel displays key parameters such as setpoint, current temperature, fan speed, sensor type, PID values, and communication status. It also provides real-time status messages like

"initializing" or "running."

6.2 Main Plot and System Information

The main plot continuously displays the actual temperature of the DUT in real time (solid blue line) compared to the user-defined setpoint (red dashed line). This visual representation helps users track system performance and response accuracy. The System Information panel shows key parameters such as connection status, setpoint, actual DUT and hotgun temperatures, selected sensor type, fan speed, and applied PID values. It also reports current system status (e.g., RUNNING or STOPPED), initialization progress, and maximum overshoot recorded since the last setpoint change.

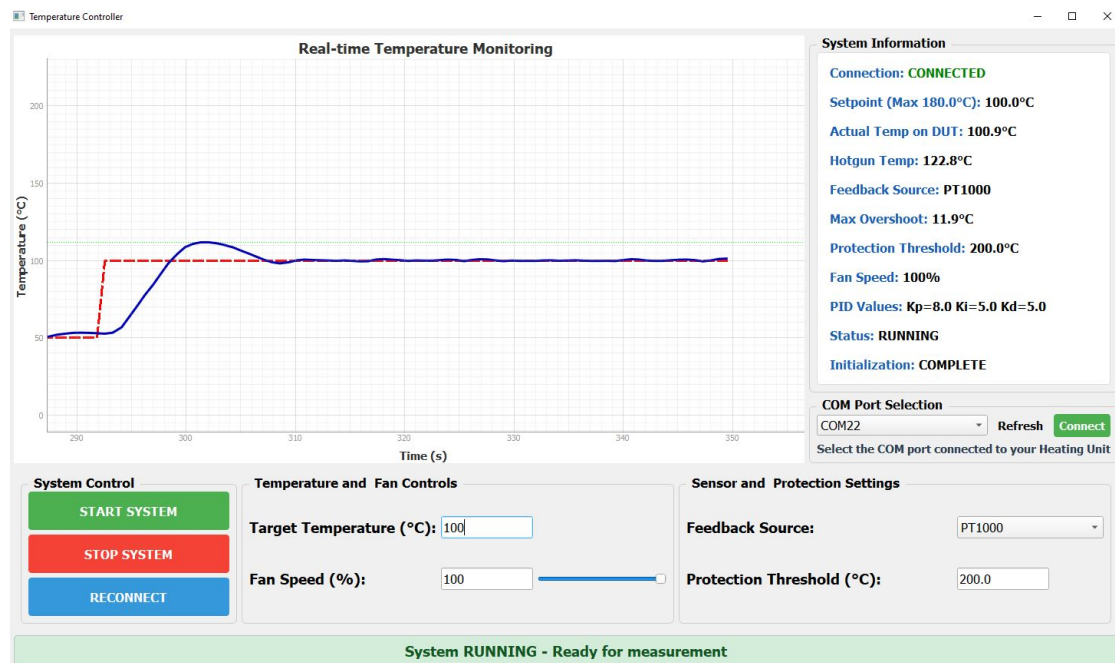


Figure 6.1: Main plot and system information panel

6.3 System Control, Temperature and Fan Controls, Sensor and Protection Setting

The System Control panel includes Start, Stop, and Reconnect buttons to manage the heating unit's operation. The Reconnect button gives the user the option to manually restart communication between the PC and the microcontroller. Normally, the system attempts automatic reconnection up to 10 times if the initial connection fails. However, if all automatic retries are unsuccessful, the user may need to physically reset the USB port by unplugging and reconnecting the cable. The Temperature and Fan Controls section allows users to set the desired temperature and adjust fan speed. The Sensor and Protection Settings panel provides options to choose the feedback source (PT1000 or thermocouple) and set a protection threshold, which is 200°C by default.

6.4 COM Port Selection and Interactive Status Bar

The system automatically scans for available communication ports, and the COM Port Selection panel allows users to manually select the correct port for establishing a connection between the GUI and the heating unit. Once the port is selected, pressing the Connect button initiates the connection process. As shown in Figure 6.2, the Interactive Status Bar provides continuous real-time feedback on system events. It displays messages such as connection status, readiness prompts, temperature settling progress, and running state. In case of critical events, it clearly alerts the user to over-temperature, hot gun over-temperature, or under-temperature conditions. These visual messages not only improve usability but also help ensure the system is operating safely and efficiently at all times.

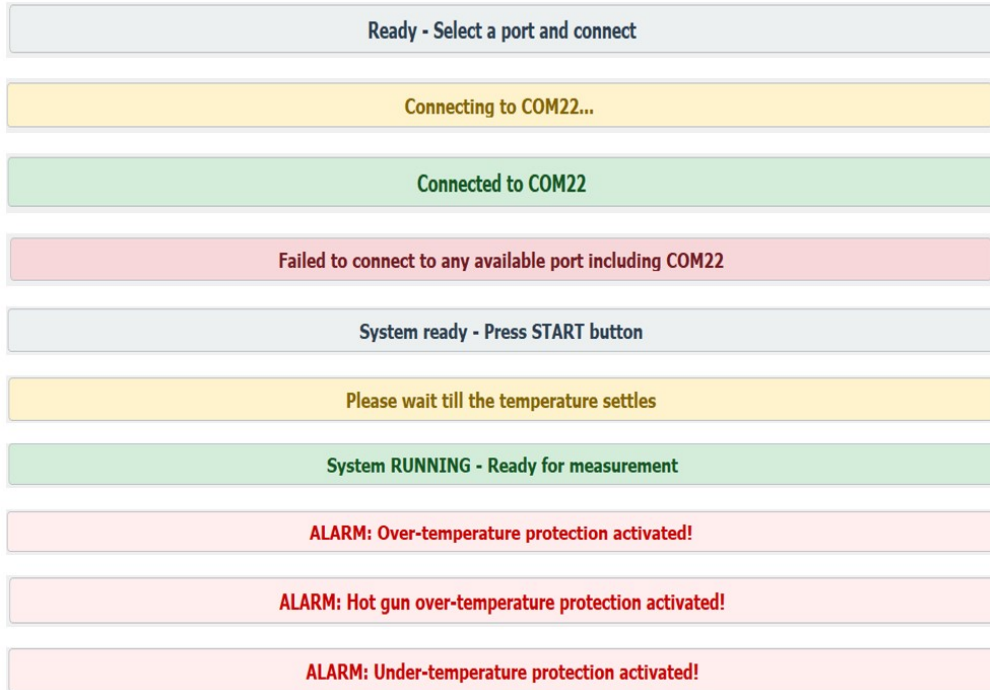


Figure 6.2: COM port selection and status bar

6.5 Performance Analysis with PT1000 as Feedback Source

Figure 6.1 shows a test scenario where the target setpoint is 100°C, and the PT1000 sensor is selected as the feedback source. The system reaches the setpoint with a maximum overshoot of 11.9°C and then quickly stabilizes with minimal oscillation. The actual temperature closely follows the setpoint, maintaining a tolerance within $\pm 1^\circ\text{C}$. This highlights the PT1000's high accuracy and responsiveness in temperature sensing. Once settled, the system remains steady without significant fluctuation, demonstrating excellent thermal control. Compared to a K-type thermocouple, the PT1000 consistently delivers better control behavior in terms of overshoot and stability. Additionally, the precision of PT1000 allows more effective PID tuning across a wide range of temperatures, making it a preferred sensor for demanding applications.

6.6 Performance Analysis with K-Thermocouple as Feedback Source

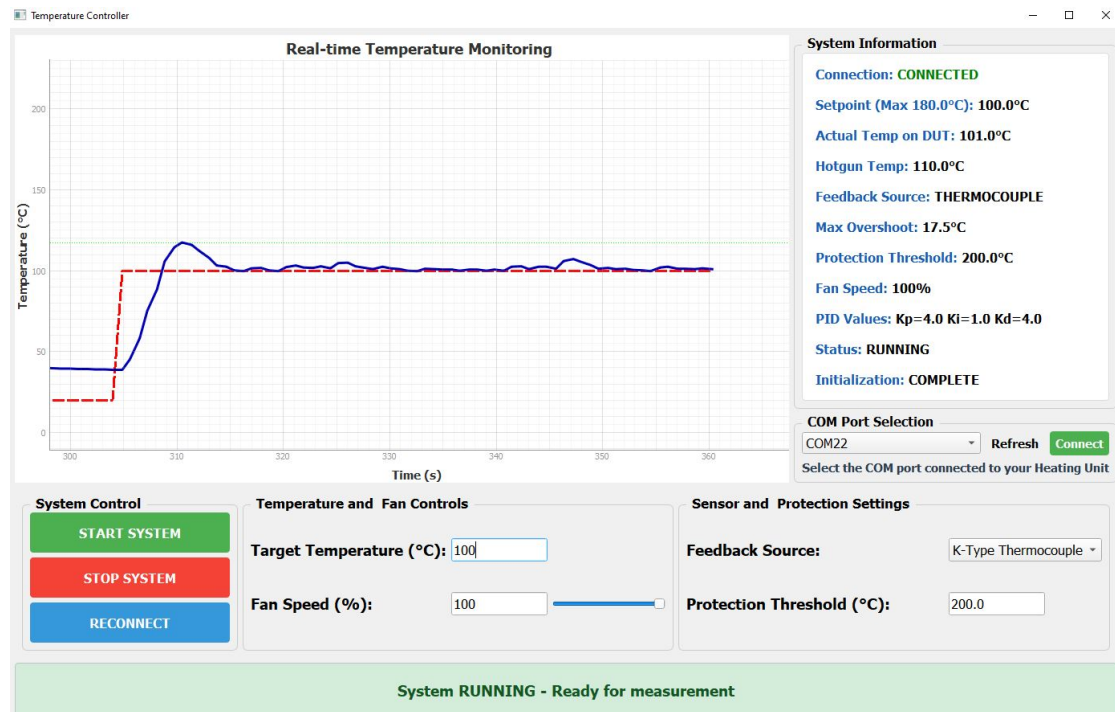


Figure 6.3: System response using K-type thermocouple

Figure 6.3 presents the system response when using a K-type thermocouple as the feedback source with a setpoint of 100°C. The system reaches the target quickly but exhibits a higher maximum overshoot of 17.5°C. While the thermocouple allows for faster heating, it tends to stabilize with more residual oscillations and shows a wider steady-state deviation, typically within $\pm 5^\circ\text{C}$. Compared to PT1000, the thermocouple offers lower accuracy and stability in maintaining tight temperature control. However, it remains a practical alternative when cost is a concern, as PT1000 sensors are significantly more expensive. Additionally, it was observed that overshoot values may vary across tests, even for the same setpoint. This variation is primarily influenced by initial and final temperature differences, as thermal inertia plays a key role in system behavior. For applications requiring high precision and minimal overshoot, PT1000 remains the preferred option despite its

cost.

6.7 Different Protection Mechanisms

6.7.1 Over-Temperature Protection Using Protection Threshold Setting

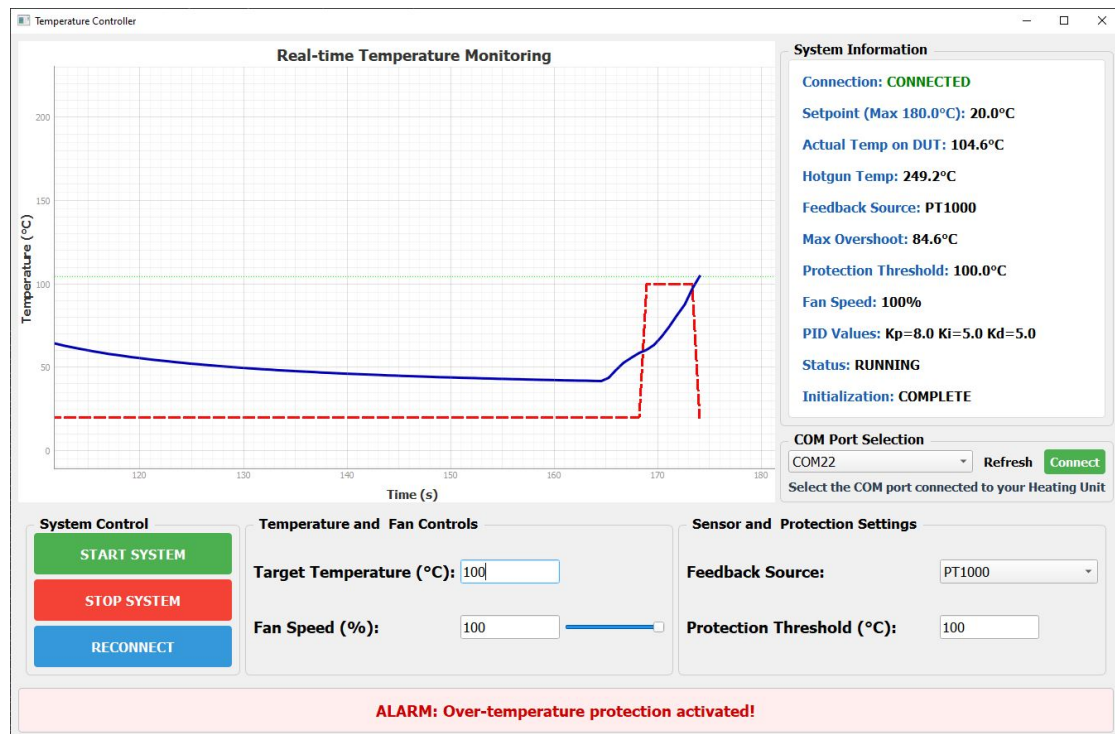


Figure 6.4: Over-temperature protection based on user-defined threshold

As shown in Figure 6.4, the over-temperature protection feature allows users to define a safety threshold, which is set to 200°C by default but can be adjusted as needed. In this test case, the threshold was reduced to 100°C. If the actual DUT temperature exceeds this limit, the system automatically resets the setpoint to 20°C and triggers a relay to cut off power to the heating element. Additionally, the system prevents users from setting a target temperature higher than the defined

threshold. This protective mechanism is vital for preventing overheating, reducing thermal stress on components, and ensuring operator safety during testing.

6.7.2 Over-Temperature Protection Using Hot Gun Temperature

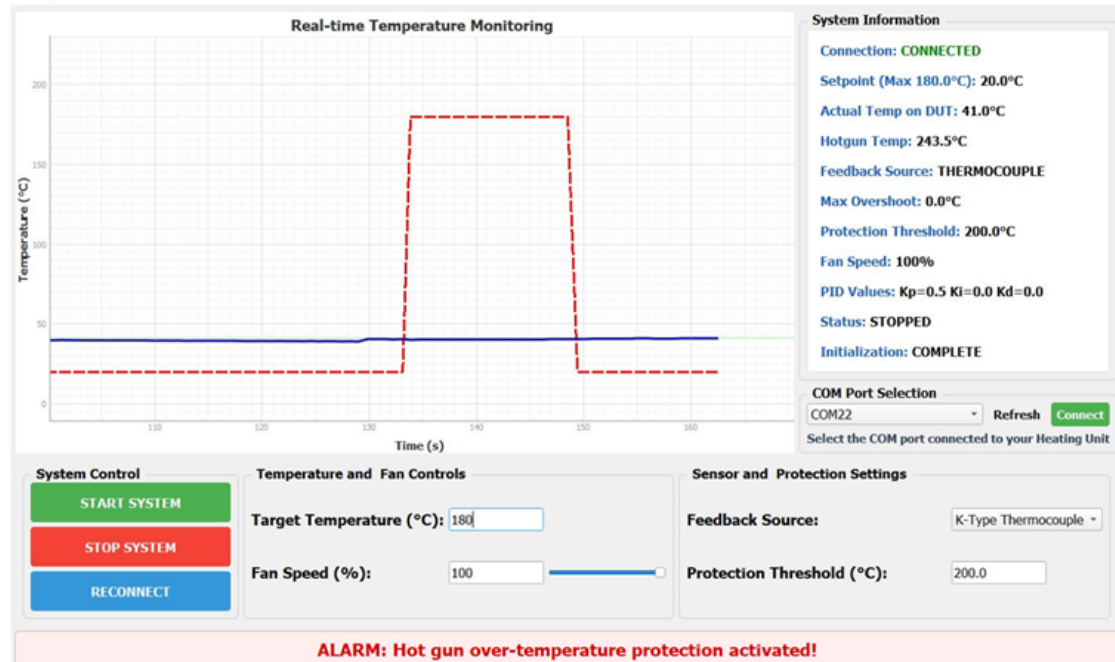


Figure 6.5: Over-temperature protection triggered by hot gun

As illustrated in Figure 6.5, the system includes an additional safety mechanism that monitors the hot gun's internal temperature using its built-in thermocouple. In this case, a target temperature of 180°C was set, but the hot gun was not properly aimed at the DUT. As a result, the DUT temperature remained low while the hot gun continued heating excessively. Once the hot gun temperature exceeded the internal threshold, the system immediately reduced the setpoint to 20°C and activated the relay to cut off power. This independent protection layer helps prevent damage when the feedback sensor fails to reflect actual heating, enhancing overall system safety.

6.7.3 Under-Temperature Protection

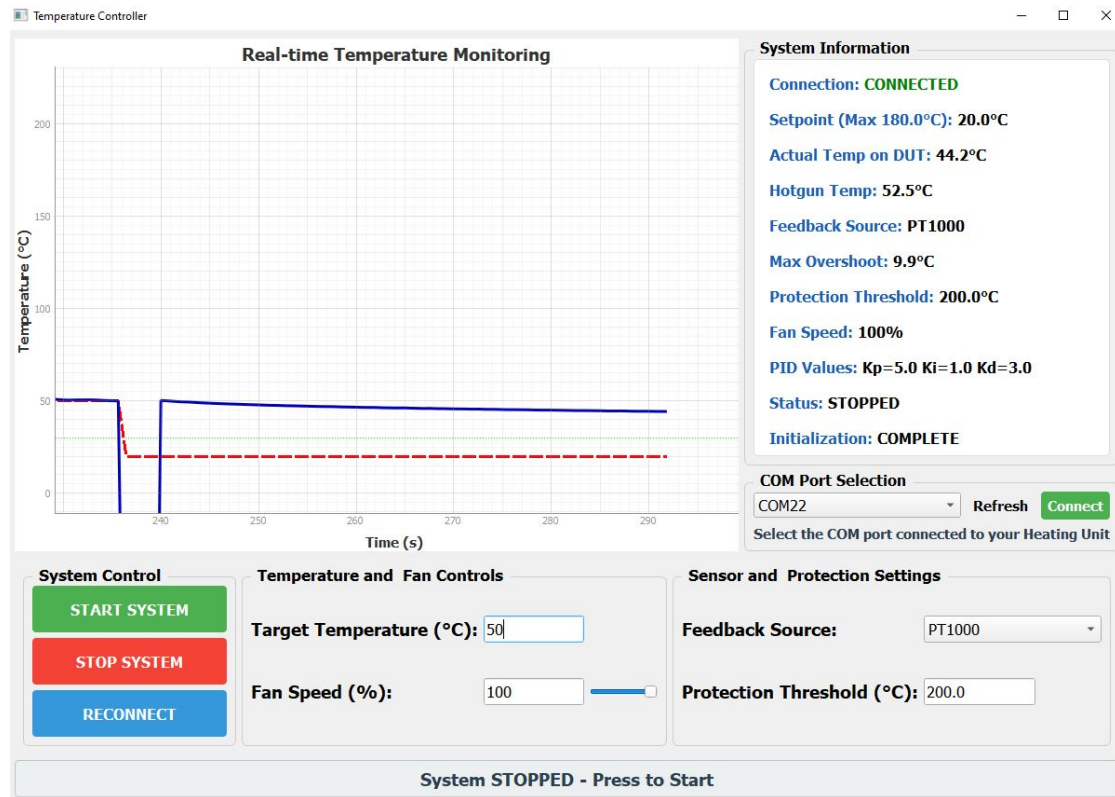


Figure 6.6: Under-temperature protection mechanism

As illustrated in Figure 6.6, the under-temperature protection mechanism is designed to prevent uncontrolled heating in case of sensor failure or abnormal readings. This typically occurs if the PT1000 sensor is shorted or disconnected, resulting in falsely low or even negative temperature values. In such situations, the system may dangerously continue heating in an attempt to reach the setpoint. To address this, the system monitors for values below a predefined threshold—15°C in this case. If breached, the system resets the setpoint to 20°C and cuts off power using the relay, ensuring safe shutdown. This logic adds a critical safety layer against thermal runaway events.

6.8 Problem Observed with Interposer Assembly

The assembly process for mounting the Device Under Test (DUT) involves a combination of three essential components: the rubber pad, the interposer, and the socket. This modular configuration is designed to enable straightforward DUT replacement while ensuring robust electrical contact with the underlying measurement board. As illustrated in Figure 6.7, the DUT is placed above the solder pads, with the rubber pad establishing the electrical interface. The interposer provides mechanical stability and alignment, while the socket secures the entire stack-up during measurement. This structure offers both mechanical reliability and high contact fidelity under standard testing conditions.

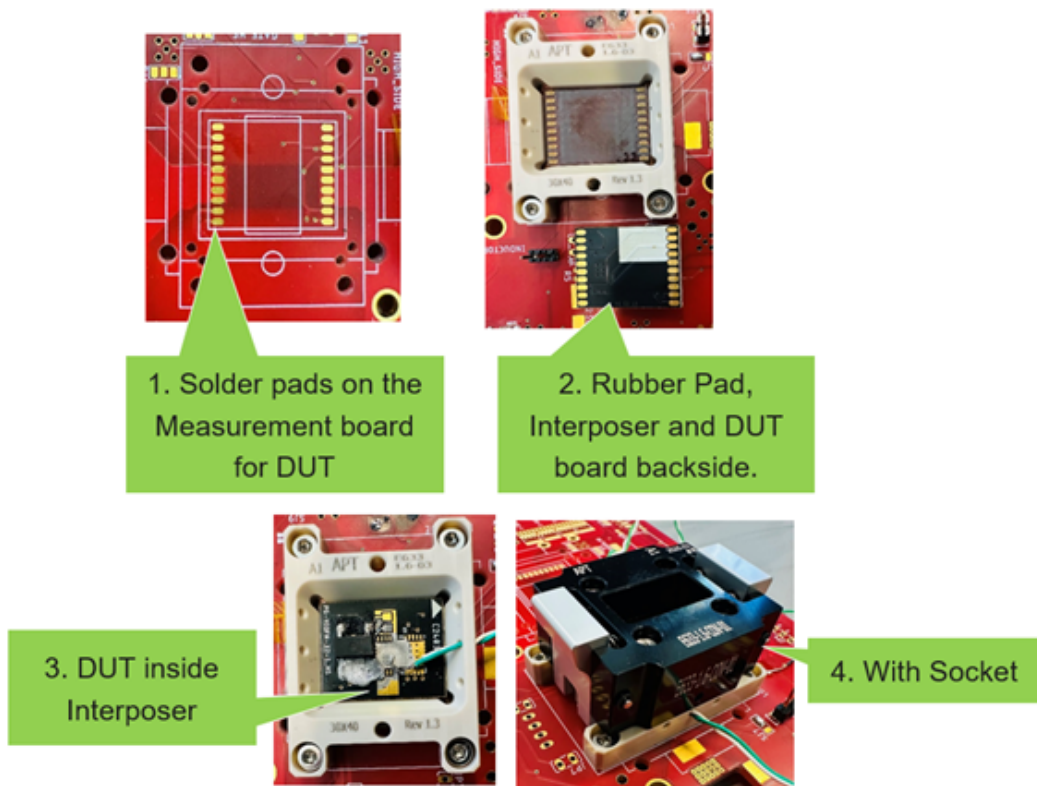


Figure 6.7: Illustration of the rubber pad, the interposer, and the socket

However, under elevated thermal stress—specifically temperatures exceeding 150 °C—the rubber pad exhibits deformation, compromising contact integrity between the DUT and the measurement board. This leads to discontinuity in the electrical connec-

tion, particularly affecting the PT1000 sensor feedback used for thermal control. The disrupted feedback loop activates a built-in protection mechanism, which disables the heating unit and halts testing to avoid damage. To overcome this issue, a revised interposer design was implemented. The improved structure reinforces mechanical compression, maintaining consistent pressure despite rubber pad deformation and thus ensuring uninterrupted electrical contact. This modification not only restored measurement reliability but also extended the thermal robustness of the test fixture under prolonged high-temperature exposure. As an added benefit, the new interposer reduces the need for manual re-seating, streamlining the overall test setup process.

6.9 Custom Back Panel for Heating Unit

To facilitate modular connectivity and improve serviceability, a custom back panel was designed using Autodesk Fusion 360. The layout accommodates essential interfaces, including connectors for the PT1000 sensor and thermocouple, a USB port for Arduino communication, and a power socket for the heating unit. Figure 6.8 illustrates the rendered view of the designed panel.

Following the design phase, the back panel was manufactured by outsourcing the fabrication process to a PCB manufaucture. This solution significantly simplifies the process of modifying or duplicating the heating unit. Unlike the original version, which included hard metallic parts difficult to reshape, the new modular back panel enables straightforward assembly and rapid prototyping for future iterations.



Figure 6.8: Custom-designed back panel for Heating Unit

Chapter 7

Measurement and Analysis of SiC MOSFET Switching Losses over Temperature

7.1 Purpose of the Measurement and Analysis

In today's technologically driven society, the reliable operation of electronic circuits and controlled electric drives requires a continuous and efficient supply of electrical energy. This demand is largely fulfilled by power electronic converters, which are constructed using controllable power semiconductor devices such as IGBTs and MOSFETs. Despite substantial progress in semiconductor fabrication and device performance, power losses—particularly within switching devices—remain unavoidable. These losses are converted into thermal energy, leading to an increase in the junction temperature of the semiconductor.

To ensure long-term reliability, the junction temperature must be maintained below the device's specified thermal limits. Furthermore, the cyclical nature of power converter operation causes repetitive heating and cooling, known as thermal cycling, which significantly influences the lifetime of semiconductor components[22]. This factor must be considered during the thermal design phase, especially when selecting appropriate cooling mechanisms.

Accurately estimating power losses is therefore essential for both thermal management and performance optimization. These losses are generally categorized into conduction losses and switching losses. While conduction losses can be determined with relative ease, switching losses are more complex to quantify due to their dynamic nature and the fast transient conditions involved. Understanding these switching losses—particularly under varying thermal conditions—is critical for designing high-efficiency power systems that remain reliable under fluctuating operational stress. This study focuses specifically on the temperature-dependent behavior of switching losses in SiC MOSFETs, highlighting their role in thermal modeling and system-level performance evaluation.

7.2 Objectives of Double Pulse Test

Switching losses in SiC MOSFETs occur predominantly during their turn-on and turn-off transitions, contributing directly to energy dissipation and affecting the overall efficiency of power electronic converters. The Double Pulse Test (DPT) is a widely adopted method for quantifying these losses under dynamic operating conditions[9]. It allows for accurate evaluation of the energy lost during each switching event, providing crucial data for performance optimization.

Silicon carbide (SiC) MOSFETs are recognized for their high-speed switching and thermal resilience compared to conventional silicon-based devices[23]. However, their switching efficiency is notably sensitive to junction temperature. The DPT enables the systematic assessment of switching losses across a range of temperatures, offering insights into how thermal variations influence key device parameters such as carrier mobility, threshold voltage, and switching time[24].

As switching losses inherently produce heat, they can trigger a positive feedback loop—raising the device temperature, which in turn affects electrical behavior and reliability. By characterizing switching losses under different thermal conditions, the DPT supports the design of effective thermal management systems aimed at preventing thermal runaway and extending device lifetime. The primary goal of the DPT is to separate and analyze turn-on and turn-off energy losses. These are influenced by multiple factors, including gate drive voltage, switching speed, parasitic inductance, and the device's internal capacitances. Through precise waveform

measurement and energy integration, the test reveals how these losses evolve with changing temperature, enabling engineers to tailor circuit designs for optimal efficiency.

SiC MOSFETs are increasingly used in high-efficiency applications such as electric vehicles, solar inverters, and industrial drives. However, if switching losses are not minimized, the full performance potential of these devices cannot be realized. The Double Pulse Test offers the necessary empirical data to support gate driver tuning, thermal design, and layout optimization under real-world thermal stress conditions.

In addition, it allows manufacturers and system designers to validate switching performance in environments with fluctuating loads and temperatures. Ultimately, the Double Pulse Test is an indispensable tool in the characterization and optimization of SiC MOSFETs. By enabling accurate, temperature-dependent switching loss analysis, it contributes to enhanced system-level efficiency, reliability, and robustness across diverse operating scenarios.

7.3 Test Setup

The complete measurement setup is enclosed within a safety box, designed to ensure operator safety during high-voltage testing procedures. This enclosure provides mechanical protection and electrical isolation, preventing unintentional contact with energized components. For enhanced safety, the system includes an interlock mechanism that disables the power supply if the door is opened. Additionally, a programmed delay of approximately 10 seconds allows parasitic energy stored in the system to dissipate before physical access is granted. This delay significantly reduces the risk of accidental shock or component damage due to residual charge.

A heating unit is mounted internally and interfaced through the rear panel (PT1000) of the Dynamic Measurement Station Figure 7.6. It enables temperature-controlled testing by regulating the thermal conditions experienced by the device under test (DUT). The temperature can be varied from ambient levels up to 180°C to replicate real-world operating environments. The DUT temperature is monitored in real-

time via a PT1000 or thermocouple sensor directly affixed to the device surface, ensuring precise thermal feedback for control and protection.

The Dynamic Measurement Station Figure 7.5 (DMS) serves as the core test platform, integrating essential elements for double pulse testing such as power delivery, signal generation, and measurement interfaces. It supports a variety of measurement boards and device packages. Internally, the DMS incorporates a configurable microcontroller that allows users to define pulse sequences, adjust gate resistance (R_g), and set gate-source voltage (V_{GS}) using a dedicated software interface. This level of control is essential for capturing temperature-dependent switching behavior accurately.

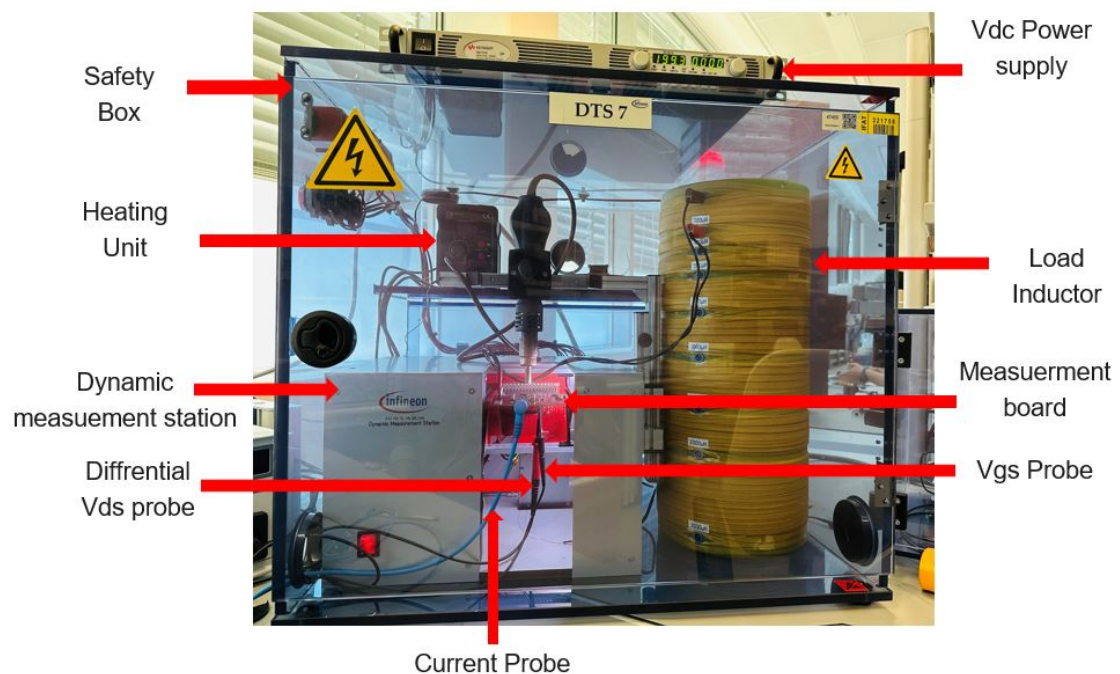


Figure 7.1: Test Setup of the Dynamic Measurement Station

Voltage across the device is measured using a differential V_{DS} probe Figure 7.12, which ensures high bandwidth and common-mode rejection—critical for precise observation of fast transients during switching. Complementing this, a coaxial current shunt is used as the current probe to measure instantaneous current through the DUT Figure 7.13. Together, these measurements enable accurate computation of instantaneous power and switching energy losses.

The gate signal is monitored using a V_{GS} probe Figure 7.11, providing insight into the device's turn-on and turn-off behavior. Proper gate control is vital to minimize losses and ensure efficient switching transitions. The DUT is mounted on a dedicated measurement board that provides probe access, power connections, and driver circuitry necessary for the experiment.

An external DC power supply is connected via the rear interface of the station, supplying the required test voltage to the circuit Figure 7.9. A large load inductor, also integrated through the rear panel, emulates real-world inductive loads. The inductance determines the current ramp rate and stored energy, significantly influencing switching losses during the test cycle.

As shown in Figure 7.1, all system components are arranged for optimized accessibility and measurement accuracy. This comprehensive setup allows for reliable dynamic characterization of SiC MOSFET switching performance under thermally varied and electrically demanding conditions.

7.4 Description of the Test Circuit

Dynamic switching measurements were carried out using a clamped inductive load setup, commonly referred to as the double pulse test (DPT) circuit. A simplified schematic of the test configuration, including probe placements and component layout, is shown in Figure 7.2. The setup is based on a half-bridge topology comprising two transistors: the high-side switch serves as a free-wheeling path, while the low-side switch functions as the device under test (DUT). The high-side switch remains permanently turned off throughout the test.

This condition can be achieved through three established methods. The first and most typical approach involves connecting a zero-ohm external gate resistor (R_G) to suppress unintended turn-on caused by capacitive coupling through C_{GD} and the resulting voltage drop across R_G . The second method uses a direct short between the gate and source terminals. The third and more recent technique employs a negative gate bias voltage from an external supply to ensure the high-side switch stays reliably off[4]. In cases where parasitic oscillations are to be minimized, the high-side switch may be replaced with a SiC Schottky diode.

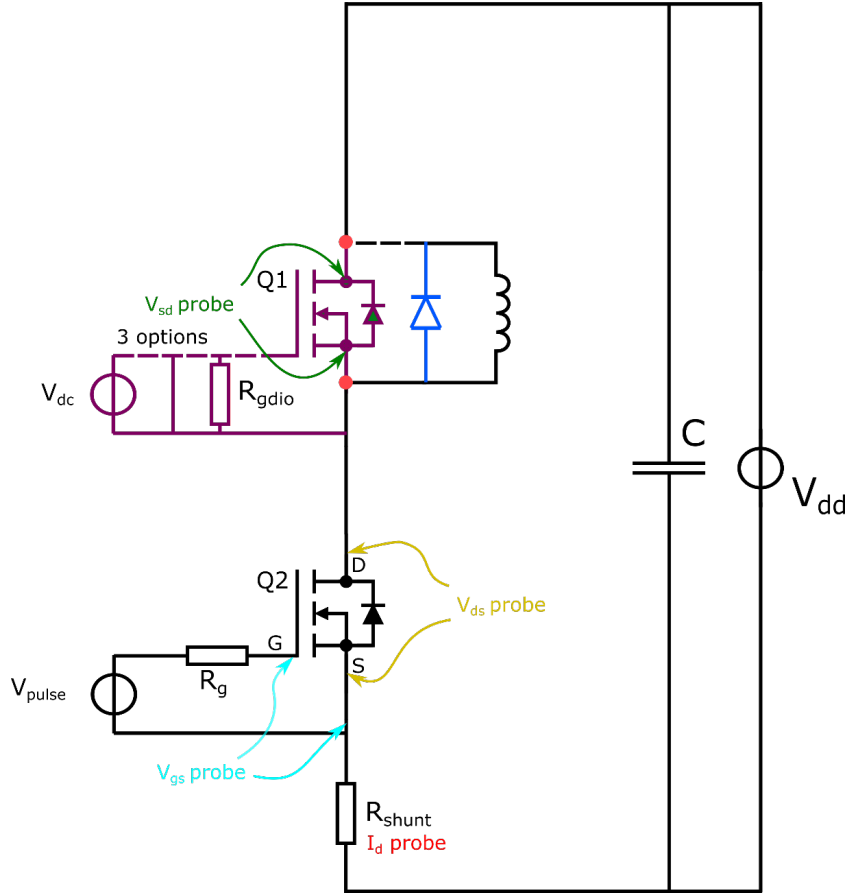


Figure 7.2: Schematic of the Double Pulse Test Circuit[4].

The low-side switch—the DUT—is actively driven by a gate driver module that supports adjustable gate resistance and configurable gate voltage levels, typically ranging from -17.5 V to $+20\text{ V}$. This flexibility allows for fine-tuning of switching dynamics during the measurement process. An inductive load (L_{Load}) is connected in parallel with the high-side switch to simulate a realistic load condition. By modulating the pulse width of the low-side gate signal, the current through the inductor can be ramped to a desired value prior to switching transitions. A pre-charged capacitor bank supplies the DC link voltage (V_{DD}) to the half-bridge via an external power source[4].

Drain current is sensed using a coaxial shunt resistor installed in the source path of the DUT. For SiC-based measurements, shunt resistors of $10\text{ m}\Omega$ or $100\text{ m}\Omega$ are typically sufficient to ensure accurate current measurement with minimal parasitic

influence. This test setup enables high-fidelity characterization of dynamic switching behavior, making it particularly well-suited for evaluating switching losses of SiC MOSFETs over a range of operating conditions.

7.5 Measurement Board

The measurement board serves as a dedicated platform for characterizing the dynamic switching behavior of silicon carbide (SiC) MOSFETs under controlled test conditions. It is designed to accurately capture key parameters—such as drain-source voltage, drain current, and temperature—while minimizing parasitic interference that could distort results.

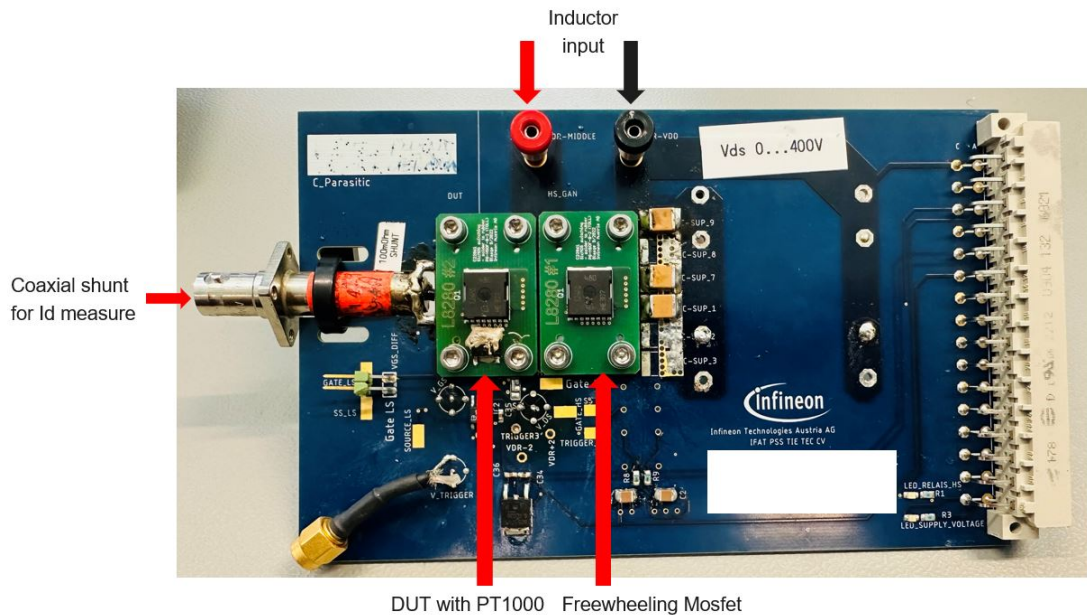


Figure 7.3: Front Side of the Measurement Board

As shown in Figure 7.3, the board provides well-defined connection points for all external components and integrates a coaxial shunt resistor for precise drain current (i_D) measurement, enabling high-resolution monitoring of current transients during switching events.

The Device Under Test (DUT) is mounted centrally on the board, paired with a PT1000 temperature sensor for real-time thermal feedback during heating. This

setup allows for accurate characterization of thermal impacts on switching losses. The board includes an integrated freewheeling SiC MOSFET placed adjacent to the DUT, ensuring voltage clamping and circuit stability during commutation events. In addition, the board accepts input from an external load inductor to emulate real-world inductive loading scenarios, facilitating energy storage and dissipation studies. Parasitic elements—particularly stray capacitance—are marked and intentionally factored into the layout to enable more refined modeling and to guide future design optimizations[10].

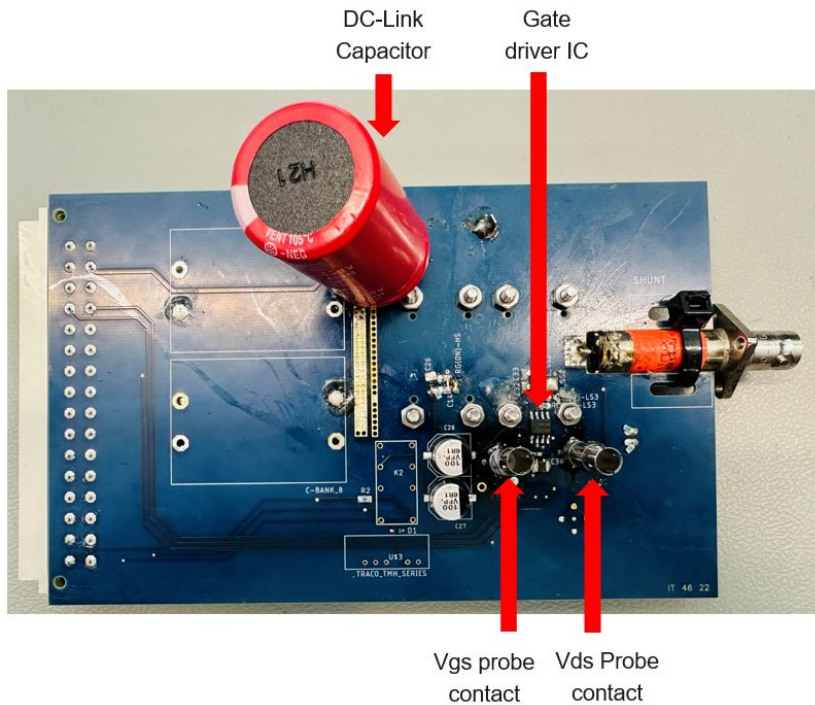


Figure 7.4: Back Side of the Measurement Board

Gate driving is handled by onboard driver ICs, with galvanic isolation implemented between gate driver supplies and the main power domain to eliminate ground loop interference. This isolation improves signal integrity and ensures reliable triggering during high-speed switching. The gate driver circuit allows for customizable gate resistance and voltage settings, enabling flexible tuning of switching behavior. The board supports a wide voltage range up to 400 V, with tests in this setup performed at 200 V.

As shown in Figure 7.4, the rear side of the board houses the large DC-link capacitor and measurement probe interfaces. The proximity of the half-bridge components, DC capacitor, and coaxial shunt enables minimal loop inductance, which is crucial for achieving fast and clean switching waveforms. Dedicated contact points for v_{GS} and v_{DS} probe measurements ensure clean signal capture without disturbing sensitive circuit paths. Together, the layout and integrated features of this measurement board establish a robust testbed for evaluating the switching efficiency and thermal robustness of SiC MOSFETs across a variety of load and temperature conditions.

7.6 Equipment Used

7.6.1 Dynamic Measurement Station



Figure 7.5: Dynamic Measurement Station

The Dynamic Measurement Station Figure 7.5 is a modular and automated platform specifically developed to facilitate accurate Double Pulse Test (DPT) procedures for power semiconductor devices. It integrates all essential components—including the measurement board, load inductor, DC power supply, heating unit, and sensor interfaces—within a centralized unit for streamlined control and precise data acquisition.

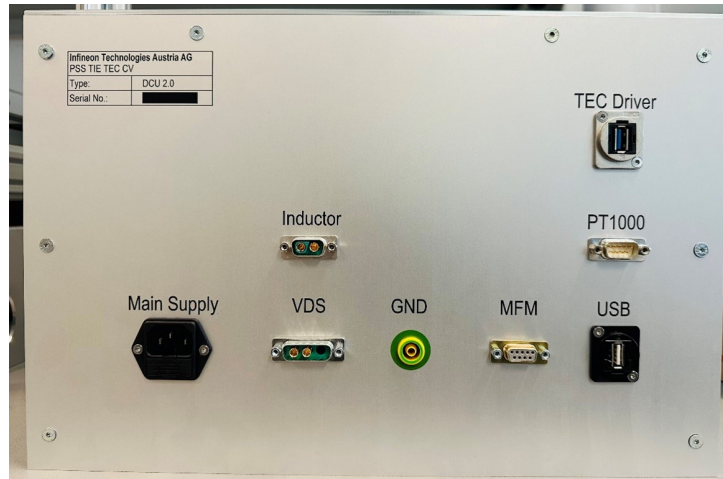


Figure 7.6: Back Panel of the Dynamic Measurement Station

The rear panel of the station, shown in Figure 7.6, includes multiple ports for interfacing with external elements, such as the inductor connection, V_{DS} terminals, GND, main power input, PT1000 temperature feedback, and TEC driver for temperature regulation.

At the core of the system lies a configurable microcontroller unit or TEC driver that enables dynamic adjustment of key parameters, such as gate-source voltage (V_{GS}), gate resistance (R_g), and pulse timing sequences. These parameters are controlled via dedicated PC software through USB communication.

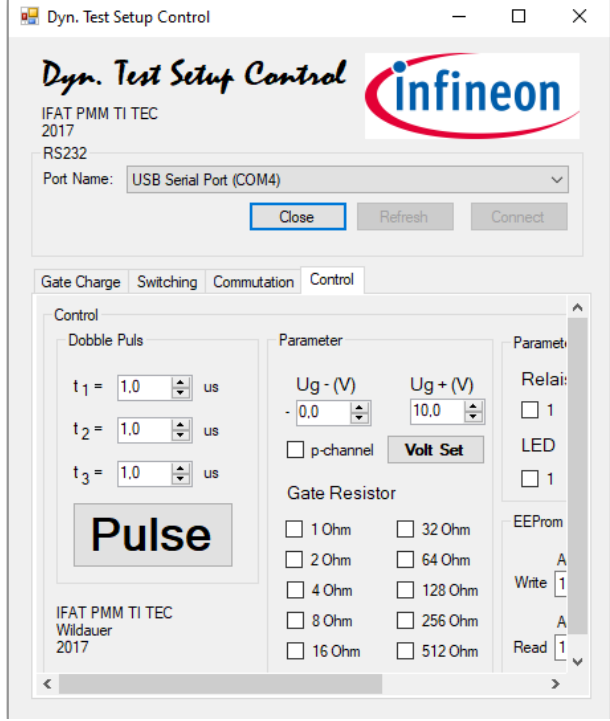


Figure 7.7: GUI of the Dynamic Measurement Station 1

As seen in Figure 7.7, the software GUI provides a clear interface for setting double pulse durations (t_1 , t_2 , t_3), defining gate voltages, selecting resistor values, and enabling relay or LED states. EEPROM read/write functionality is also included for configuration storage.

One of the notable capabilities of the station is its integration with the heating system via feedback from PT1000 sensors mounted directly on the Device Under Test (DUT). This enables real-time thermal monitoring and precise adjustment of heating output, maintaining a consistent junction temperature during measurement campaigns. Such thermal control is crucial for temperature-dependent characterization of switching losses.

Furthermore, the station's architecture supports real-time monitoring of dynamic switching variables, including drain-source voltage (V_{DS}), gate-source voltage (V_{GS}), and drain current (I_D). These are captured with high fidelity to calculate energy dissipation during switching transitions. The compact and standardized layout allows the same station to be used across a variety of MOSFET packages and board

layouts, thus improving experimental repeatability.

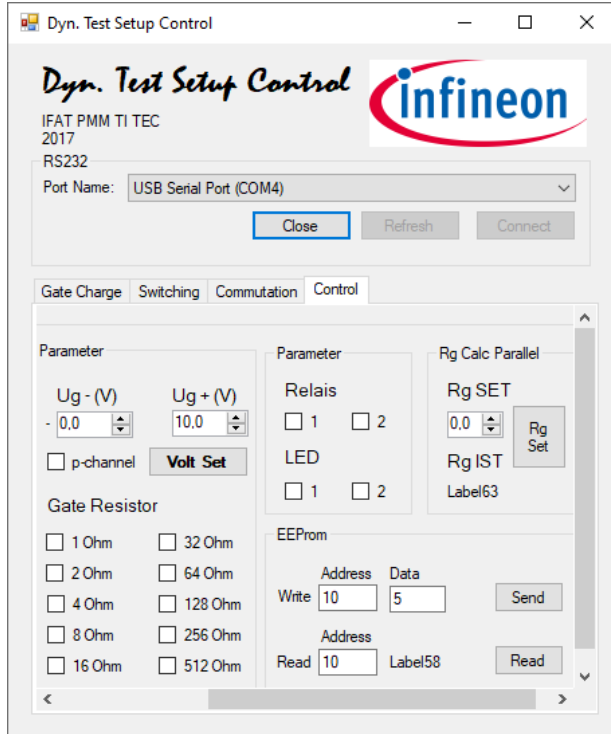


Figure 7.8: GUI of the Dynamic Measurement Station 2

7.6.2 Power Supply

For supplying the necessary DC voltage to the test setup, a Keysight N5772A programmable power supply was employed Figure 7.9. This precision instrument is capable of delivering up to 600 V, 2.6 A, with a maximum power output of 1560 W, making it suitable for charging the DC-link capacitors used in the Double Pulse Test (DPT) setup.



Figure 7.9: Keysight N5772A Programmable Power Supply[5].

In this experiment, the unit was configured to deliver a regulated DC voltage of 200 V, which served as the initial charging voltage for the capacitor bank connected to the half-bridge circuit. The high voltage capability and fine voltage/current control features of the power supply ensured consistent and safe operation throughout the measurement process.

7.6.3 Oscilloscope

To accurately capture high-speed switching waveforms, a Keysight InfiniVision DSO-X 6004A digital storage oscilloscope was employed during the measurement process. This high-performance instrument offers a bandwidth of 2 GHz and a real-time sampling rate of 20 GSa/s, making it well-suited for characterizing wide-bandgap semiconductors such as SiC and GaN, which are known for their fast switching capabilities.



Figure 7.10: Keysight InfiniVision DSO-X 6004A Oscilloscope (Front View)[6].

Its high bandwidth ensures the precise resolution of rapid voltage and current transitions during turn-on and turn-off events, which is essential for reliable extraction of dynamic parameters such as v_{DS} , i_D , and v_{GS} .

As shown in Figure 7.10, the oscilloscope supports multi-channel waveform acquisition and includes advanced triggering options that enable synchronization with switching events.

It is capable of directly measuring instantaneous power and energy losses by internally multiplying voltage and current signals over time. However, for post-processing flexibility and documentation, the waveform data were exported as CSV files using a USB interface. These files were then analyzed using a custom Python script to calculate turn-on and turn-off energy losses with higher resolution and batch processing capabilities.

7.6.4 Measurement Probes (Voltage/Current)

Accurate measurement of dynamic signals during Double Pulse Tests (DPT) necessitates the use of high-precision voltage and current probes with wide bandwidth and minimal parasitic interference. Two types of voltage probes are employed in this setup: passive probes and active differential probes.

Passive voltage probes are simple, robust, and do not require external power sources. They are ideal for general-purpose measurements but are susceptible to parasitic inductances, especially when long leads are used, which can lead to ringing and overshoots.



Figure 7.11: Tektronix P6100 Passive Voltage Probe used for V_{GS} Measurement[7].

The Tektronix P6100-series passive probe, shown in Figure 7.11, was used for gate-to-source voltage (V_{GS}) measurements. This probe offers a wide bandwidth (DC to 500 MHz), high input resistance of $10\text{ M}\Omega$ with 8 pF capacitance, and a 10:1 attenuation ratio. It can handle up to 300 V (DC or RMS, CAT II), with a compensation range of 7–30 pF, making it well-suited for fast-switching measurements.

For high-voltage drain-to-source measurements (V_{DS}), the Tektronix P5100A active differential probe was used. It offers a high impedance of $50\text{ M}\Omega$ in parallel

with 7.5 pF, a 100:1 attenuation ratio, and supports voltages up to 2000 V Figure 7.12. This allows for precise measurement of high-voltage switching events while isolating the measurement ground from the oscilloscope.



Figure 7.12: Tektronix P5100A Differential Probe used for V_{DS} Measurement[8].

Current measurement was conducted using the coaxial shunt method, a preferred technique for DPT due to its high temporal resolution and compatibility with fast-switching devices. As shown in Figure 7.13, the coaxial shunt was inserted in the source path of the device under test (DUT).



Figure 7.13: Coaxial Shunt Setup for Drain Current Measurement (i_D)

The current (I_D) was calculated based on the voltage drop across the shunt resistor using Ohm's law. However, this method is subject to a bandwidth limitation due to parasitic inductance L_{shunt} , and its upper frequency response is defined as:

$$f_{\text{BW}} = \frac{R_{\text{shunt}}}{2\pi L_{\text{shunt}}} \quad (7.1)$$

To enhance signal fidelity, a 50Ω termination resistor was connected to the oscilloscope input to match impedance and minimize reflections. Additionally, the coaxial current probe was wound with a ferrite core to suppress common-mode noise, ensuring reliable waveform capture even in high-noise environments.

7.7 De-skewing Methods and Procedure

De-skewing is a critical step in high-speed dynamic measurements, aimed at compensating for the time delay differences between voltage and current probes. Without proper de-skewing, signal misalignment may lead to inaccurate energy calculations, especially during high-speed switching transients in SiC MOSFETs.

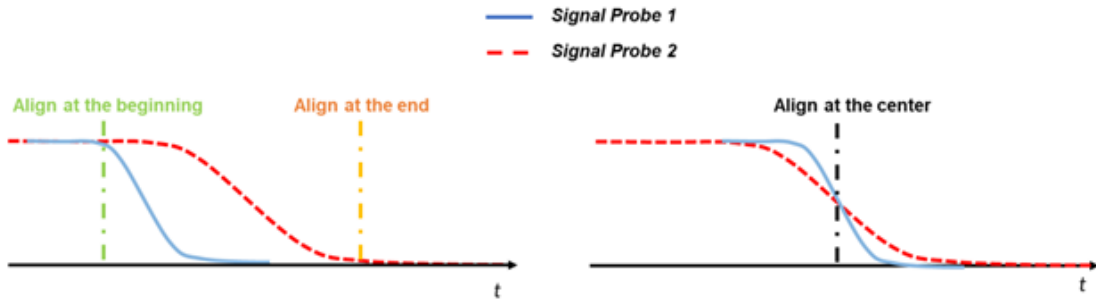


Figure 7.14: Illustration of Probe Misalignment and Midpoint Alignment during Switching Transition[9].

Figure 7.14 illustrates typical probe misalignments and alignment strategies during a signal transition. The goal of de-skewing is to synchronize the timing of voltage (V_{DS}) and current (I_D) signals captured during the double pulse test. Due to differences in probe bandwidth, cable length, and internal circuitry, even small mismatches can introduce errors in the switching energy measurement. Signal alignment can be performed at the beginning, midpoint (50% threshold), or end of the transition slope. Each method has its own application context, but aligning at the midpoint is often considered most robust for pulse symmetry[9].

In practical test setups, several techniques are available for de-skewing. One approach involves the use of a calibrated power de-skew fixture that emits known voltage and current pulses. By aligning these reference waveforms on the oscilloscope display, users can fine-tune the relative delay between probes until they overlap precisely. Another common method relies on the behavior of the actual device under test (DUT). During a switching event, the falling edge of V_{DS} can be aligned with the rising edge of I_D , particularly at the point of maximum derivative or local peak.

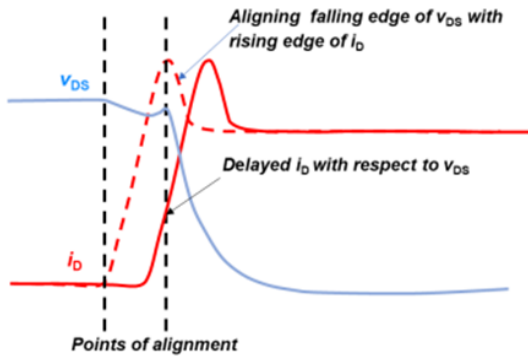


Figure 7.15: Overlay of De-skewed V_{DS} and I_D Signals during Switching[9].

In the current setup, a manual de-skewing procedure was adopted due to the absence of a dedicated de-skew fixture. The inductor was temporarily removed from the circuit and replaced by a low-inductance resistor and freewheeling diode. The resistor establishes a resistive load condition, ensuring a linear voltage-to-current relationship with minimal phase shift. Although some parasitic inductance (L_{Shunt}) is inevitable, careful component selection helps reduce its effect on accuracy.

The drain voltage during the de-skew process was limited to remain below the resistor's pulse tolerance to prevent damage. This manual method proved to be practical and repeatable, offering sufficient precision for synchronizing signals in a lab environment. It also allowed flexible adjustments tailored to the specific measurement board and probe characteristics. By performing proper de-skewing, the accuracy of switching energy loss measurements was significantly improved[9].

Chapter 8

Measurement Procedure for Switching Loss Analysis

8.1 Test Procedure

The double pulse test procedure begins with the initialization of the measurement circuit, where the capacitor bank is intentionally charged to a voltage slightly above the desired test value. This precharging strategy accounts for the expected voltage dip that occurs during the initial switching event. Specifically, when the inductive load becomes energized, a portion of the capacitor's stored energy is expended, leading to a temporary voltage drop. By precharging above the nominal test voltage, the test conditions are maintained close to the intended parameters, ensuring consistent and reliable switching behavior throughout the measurement sequence[9].

After reaching the desired voltage level, the DC power supply is disconnected from the circuit, resulting in a floating measurement configuration. In this state, the measurement setup itself defines the voltage reference. Operating at a floating potential is beneficial because it avoids direct grounding of the measurement circuit, thereby reducing the influence of common-mode noise and allowing greater flexibility in choosing measurement probes[9]. This configuration enhances the fidelity of voltage and current measurements, particularly when capturing fast switching transitions of SiC MOSFETs.

One of the key advantages of this floating setup is the possibility of performing high-side voltage measurements using passive probes. Due to their inherent robustness and simplicity, passive probes are preferred for capturing signals in electrically isolated environments. They are less sensitive to noise and do not require external power, making them suitable for high-speed dynamic tests. The ability to utilize passive probes effectively for high-side measurements significantly improves the reliability and accuracy of the captured data. Furthermore, this approach provides greater compatibility with standard differential probe arrangements and simplifies the de-skewing process by reducing potential probe-to-ground mismatches. Overall, the test procedure ensures that the double pulse test is conducted under well-controlled, reproducible conditions, allowing precise analysis of switching losses over varying operating parameters[9].

8.2 Preparation and Initial Checks

The preparatory phase of the double pulse test is critical to ensuring both the accuracy and repeatability of the measurement results. All essential instruments, including the oscilloscope, DC power supply, and dynamic measurement station, must be powered on at least 20 minutes before initiating any data acquisition[4]. This warm-up period allows the internal circuitry of the equipment to reach thermal equilibrium, reducing signal drift and electronic noise. Stabilizing the operating temperature of the measurement devices prior to testing is a standard best practice, particularly when capturing sensitive switching characteristics of wide bandgap semiconductors such as SiC MOSFETs.

The switching measurements are conducted using a fully integrated dynamic measurement station, complemented by peripheral systems including differential voltage probes, coaxial current shunts, and temperature-controlled heating units. These components are precisely configured to suit the requirements of double pulse characterization. The dynamic measurement station, often developed in-house for research purposes, features modular elements such as adjustable gate drivers, customizable measurement boards, and pulse generation tools, allowing flexibility in accommodating different DUTs and switching conditions. This modularity ensures that the test environment remains both robust and adaptable to varying

experimental setups.

8.2.1 Pulse Width and Timing

In the double pulse test, the exact timing and sequence of gate pulses are predefined and programmed into the signal generator to ensure precise control of the switching events. As depicted in Figure 9.1, the test sequence comprises three stages: a first pulse of duration τ_1 , a short intermission or pulse break τ_{break} , and a second pulse of duration τ_2 . The corresponding current and voltage waveforms, along with the active current conduction paths, are illustrated for each phase in the accompanying figure.

During the first pulse τ_1 , the device under test (DUT) is turned on, closing the current loop consisting of the pre-charged DC-link capacitor, the load inductor L_{load} , and the series parasitic resistance R_s . The goal of this interval is to linearly ramp up the load current to the intended test value. The fundamental inductor voltage-current relationship is given by:

$$v_{\text{load}} = L_{\text{load}} \cdot \frac{di_{\text{load}}}{dt} \quad (8.1)$$

Assuming $v_{\text{load}} = V_{\text{DC}}$, and integrating with respect to time, the required pulse width is:

$$\tau_1 = \frac{L_{\text{load}} \cdot I_{\text{test}}}{V_{\text{DC}}} \quad (8.2)$$

Following this, the device is turned off for a brief pulse break τ_{break} , during which the load current freewheels through the body diode or external freewheeling diode:

$$v_f = - \left(R_s \cdot i_{\text{load}} + L_{\text{load}} \cdot \frac{di_{\text{load}}}{dt} \right) \quad (8.3)$$

When the second pulse τ_2 begins, the DUT is switched on again, enabling continued energy transfer. The current peak observed in Figure 9.1 results from the reverse recovery effect of the freewheeling diode[4].

8.2.2 Gate Resistance and Drive Voltage

In double pulse testing (DPT) of MOSFETs, the selection of gate resistance R_g and gate drive voltage V_{dr} is crucial for shaping the device's switching dynamics.

A lower R_g value facilitates faster transitions, enhancing switching efficiency but increasing di/dt and dv/dt rates. Conversely, a higher R_g value reduces EMI and overshoot but increases switching losses[9].

Similarly, applying a gate drive voltage V_{dr} typically in the range of 12–15 V for SiC MOSFETs ensures full enhancement and minimal $R_{DS(on)}$. Exceeding gate voltage limits (typically ± 20 V) can damage the gate oxide, whereas too low a voltage increases conduction losses[4].

8.3 Measurement Points

8.3.1 Voltage Probing Locations

Accurate placement of measurement probes is essential for capturing the gate-to-source voltage (V_{GS}), drain-to-source voltage (V_{DS}), and drain current (I_D) during switching events. The V_{GS} probe is connected directly between the gate and source terminals of the MOSFET to monitor the gate signal in real time. This measurement ensures that the gate voltage remains within the specified operating range and provides valuable insight into the effectiveness of the gate driver circuit. Proper probe alignment minimizes distortion and helps evaluate the influence of gate resistance on switching dynamics. Likewise, the V_{DS} probe is positioned between the drain and source terminals to capture the voltage waveform across the MOSFET during turn-on and turn-off transitions. This information is critical for analyzing energy losses and detecting transient phenomena such as overshoot, ringing, or voltage spikes.

As illustrated in Figure 7.2, careful probe placement is necessary to reduce the effects of parasitic inductance and to preserve signal integrity. To achieve high measurement accuracy, probes must be placed close to the device under test with short ground leads and minimal loop area. This is particularly important for V_{DS} measurements, which are highly sensitive to switching noise and high-frequency oscillations. These probing techniques support a reliable evaluation of the SiC MOSFET's dynamic behavior across different load and temperature conditions. Collectively, the voltage and current probing strategy plays a vital role in assessing

performance, optimizing circuit design, and ensuring the long-term reliability of the switching device[4].

8.3.2 Current Probing Location

The drain current (I_D) is measured using a coaxial shunt connected in series with the drain terminal of the SiC MOSFET. This shunt-based current probe is engineered for low inductance and resistance to reduce parasitic interference and enable accurate current sensing during high-speed switching transitions. Proper placement of the shunt ensures minimal signal distortion, allowing the capture of precise current waveforms that reflect the true dynamic behavior of the device.

As shown in Figure 7.2, the captured I_D waveform is vital for analyzing current transients during both turn-on and turn-off intervals. These measurements are essential for computing switching energy losses and evaluating overall device efficiency under varying electrical and thermal loads. Additionally, accurate current probing supports synchronized measurements with voltage waveforms, enabling correct power and energy calculations during post-processing. To further reduce noise and ensure signal fidelity, a 50Ω termination resistor is typically used at the oscilloscope input.

8.4 Data Acquisition

During the double pulse test, data acquisition is performed with precision to ensure accurate capture and retention of dynamic switching characteristics. The oscilloscope functions as the central tool for recording high-speed voltage and current signals during the critical turn-on and turn-off events of the SiC MOSFET. These waveforms are exported in CSV format to a USB drive, providing structured datasets that include time, drain-source voltage (V_{DS}), gate-source voltage (V_{GS}), drain current (I_D), instantaneous power, and cumulative energy. Each CSV file reflects a high-resolution temporal snapshot of a switching interval, enabling post-processing and analysis with tools such as Python.

In parallel with numerical logging, visual oscilloscope screenshots are saved to document waveform behavior graphically. These real-time images complement

the CSV data by highlighting anomalies, overshoot, or ringing effects that may be difficult to interpret from numerical output alone. As illustrated in Figure 7.2, this dual-format approach facilitates both quantitative and qualitative understanding of switching dynamics. To further streamline the workflow, file naming conventions are standardized based on test conditions, improving traceability and organization during batch testing.

8.5 Measurement Parameters

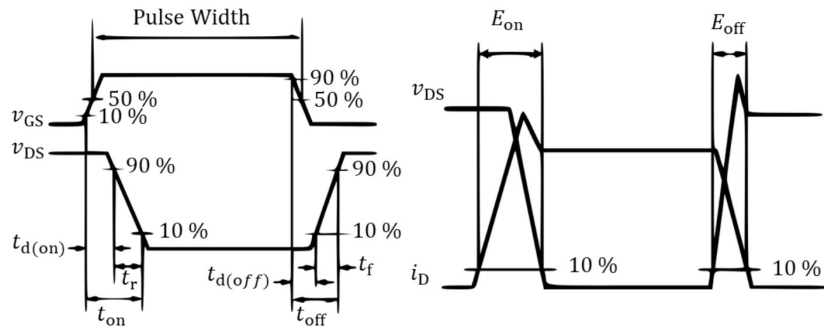


Figure 8.1: Parameter_{waveform}

The double pulse test enables the extraction of key switching characteristics such as rise time, fall time, switching energies, and peak overshoots in voltage and current. These parameters are derived from the switching waveforms obtained under hard-switching conditions. As illustrated in Figure 8.1, the evaluation of these parameters provides crucial insights into the transient behavior of the MOSFET and serves as a benchmark for assessing device performance and switching losses[9].

8.5.1 Turn-on Energy (Eon)

Turn-on energy loss is computed by integrating the instantaneous power during the turn-on interval. It is defined within the time window where the drain current rises from 10% of I_{test} and the drain voltage drops to 10% of V_{DC} . The energy is calculated as:

$$E_{on} = \int_{t_{I_{test},10\%}}^{t_{V_{DC},10\%}} v_{DS}(t) \cdot i_D(t) dt \quad (8.4)$$

8.5.2 Turn-off Energy (E_{off})

Turn-off energy loss is determined similarly, based on the time interval where the drain voltage rises to 10% of V_{DC} and the drain current falls to 10% of I_{test} . It is given by:

$$E_{\text{off}} = \int_{t_{V_{\text{DC}},10\%}}^{t_{I_{\text{test}},10\%}} v_{\text{DS}}(t) \cdot i_{\text{D}}(t) dt \quad (8.5)$$

8.5.3 Switching Times ($t_{\text{on}}, t_{\text{off}}, t_{\text{d}}$)

- $t_{\text{d}(\text{on})}$: Turn-on delay time – time between 10% of the rising v_{GS} and 90% of the falling v_{DS} .
- t_r : Rise time – time interval for v_{DS} to fall from 90% to 10%.
- $t_{\text{d}(\text{off})}$: Turn-off delay time – time between 90% of the falling v_{GS} and 90% of the rising v_{DS} .
- t_f : Fall time – time interval for v_{DS} to rise from 10% to 90%.

8.6 Parasitic Effects Observed

Parasitic elements significantly influence the dynamic switching behavior of power semiconductors, particularly during double pulse testing. As illustrated in Figure 8.2, the equivalent test circuit includes various distributed parasitics such as inductances from the busbar (L_{Bus}), source and drain terminals (L_S, L_D), gate path (L_G), sense path (L_{Sense}), and external measurement or load connections. Additionally, parasitic capacitances across device terminals, including C_{GS} , C_{DS} , and C_{GD} , as well as layout-induced capacitances such as C_{DD} , contribute to dynamic behavior. These stray components introduce oscillations, overshoots, and waveform distortion during high-speed transitions, directly affecting switching energy losses and electromagnetic compatibility.

During fast switching events, these parasitic interactions become more critical. For instance, common source inductance introduces undesired voltage feedback that distorts the gate signal and slows the transition, leading to elevated losses and

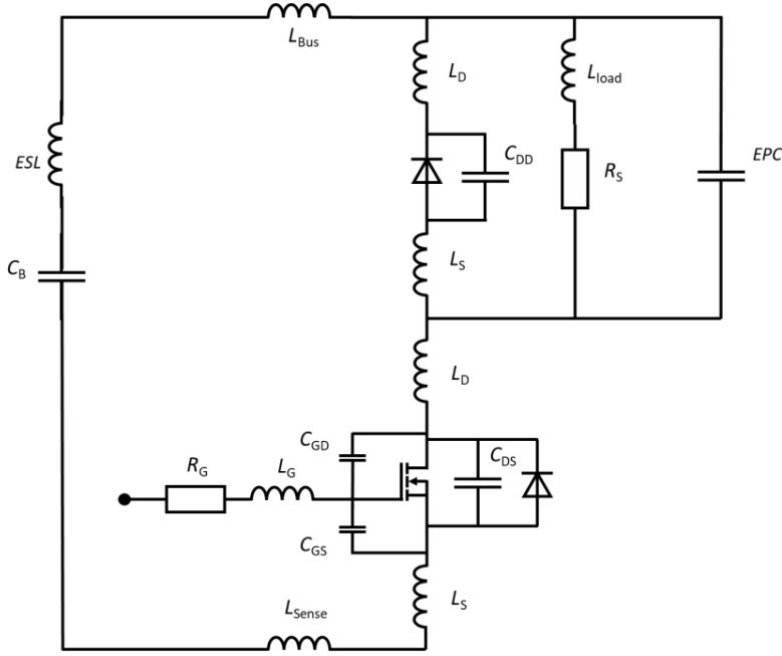


Figure 8.2: Parasitic Equivalent Circuit[9].

voltage spikes. On turn-on, high di/dt interacts with stray inductance to generate overshoot in V_{DS} , while during turn-off, the interplay between device capacitance and loop inductance results in oscillations that can stress the MOSFET beyond its rated limits. Accurately modeling and minimizing these parasitic effects is essential for obtaining representative switching energy data and ensuring safe and reliable operation in real-world converter designs. It is also noteworthy that optimization of PCB layout, measurement probe routing, and gate drive impedance play a pivotal role in suppressing these effects[9].

8.7 Verify Functionality of Setup

Before initiating any switching measurements, it is essential to confirm that all connected hardware components function correctly. This preliminary verification step helps ensure that the measurement setup operates reliably and safely under the intended test conditions. Performing basic tests before applying full power to the device under test (DUT) helps identify potential misconfigurations and avoid

unnecessary risks during the switching procedure[10].

8.7.1 Gate Pulse Test

As a first step, the accuracy of the applied gate pulse should be validated prior to introducing any DUT or load resistance into the circuit. For this purpose, only the gate resistor (R_g) must be configured using the TEC Driver software interface. The test can be performed without connecting a load, and a pulse width on the order of a few microseconds is typically sufficient. The oscilloscope should be configured to trigger on the gate-source voltage (V_{GS}) channel, with the trigger threshold adjusted to match the expected gate drive voltage.



Figure 8.3: Gate Pulse Verification without DUT[10].

Upon triggering the gate pulse via the TEC Driver program, a square waveform corresponding to the defined V_{GS} values should appear on the oscilloscope screen. This waveform confirms the integrity of the signal path and the functionality of the driver. The pulse amplitude should closely match the programmed gate drive levels, while the pulse width should correspond to the configured timing parameters. As shown in Figure 8.3, the waveform presents a stable gate pulse in the absence of a DUT, verifying correct system response and signal propagation. This test can also be repeated with a DUT in place for additional verification, provided safety protocols are followed[10].

8.7.2 Drain Supply V_{DC}

Prior to conducting switching tests, it is necessary to ensure that the drain terminal is supplied with the intended V_{DC} level. This verification is typically performed by inserting a dummy resistor (R_0) to create a current path on the low side. Once the resistor is in place, the desired drain voltage is set on the power supply unit. The safety enclosure door must be properly closed before enabling the power supply output, which should then be ramped up gradually to the target value.

This precaution is critical to avoid unexpected voltage application or unsafe operating conditions. In the event the safety box is opened during operation, the system is designed to immediately disconnect the supply to the measurement board, thereby safeguarding the user and the equipment. Such built-in interlocks reinforce operational safety while maintaining test continuity and reliability.

Chapter 9

Data Analysis

9.1 Waveform Interpretation

The waveform obtained from a Double Pulse Test (DPT) on a 400 V Silicon Carbide (SiC) MOSFET provides valuable insight into its switching characteristics and energy dissipation. As shown in Figure 9.1, the test is divided into key intervals: the first pulse (τ_1), a break time (τ_{break}), and the second pulse (τ_2).

The gate-source voltage V_{GS} (blue trace) is set to 18 V during turn-on, activating the MOSFET. The drain-source voltage V_{DS} (yellow) drops sharply, while the current I_D (green) ramps linearly due to inductor charging. During the first pulse, the inductor stores energy, and pulse width is tuned to reach the desired test current.

At turn-off, V_{GS} drops to 0 V or a negative voltage to ensure full deactivation. Consequently, V_{DS} rises and I_D falls to zero. A short break time τ_{break} follows to ensure complete switch-off and to retain inductor energy for the next pulse.

The second pulse begins similarly with V_{GS} rising to 18 V. A brief current spike appears due to reverse recovery of the body diode. This is followed by a controlled linear current rise. Pulse width is kept short to avoid excessive inductor charging. Figure 9.2 shows the corresponding real-time oscilloscope capture, validating these events[9].

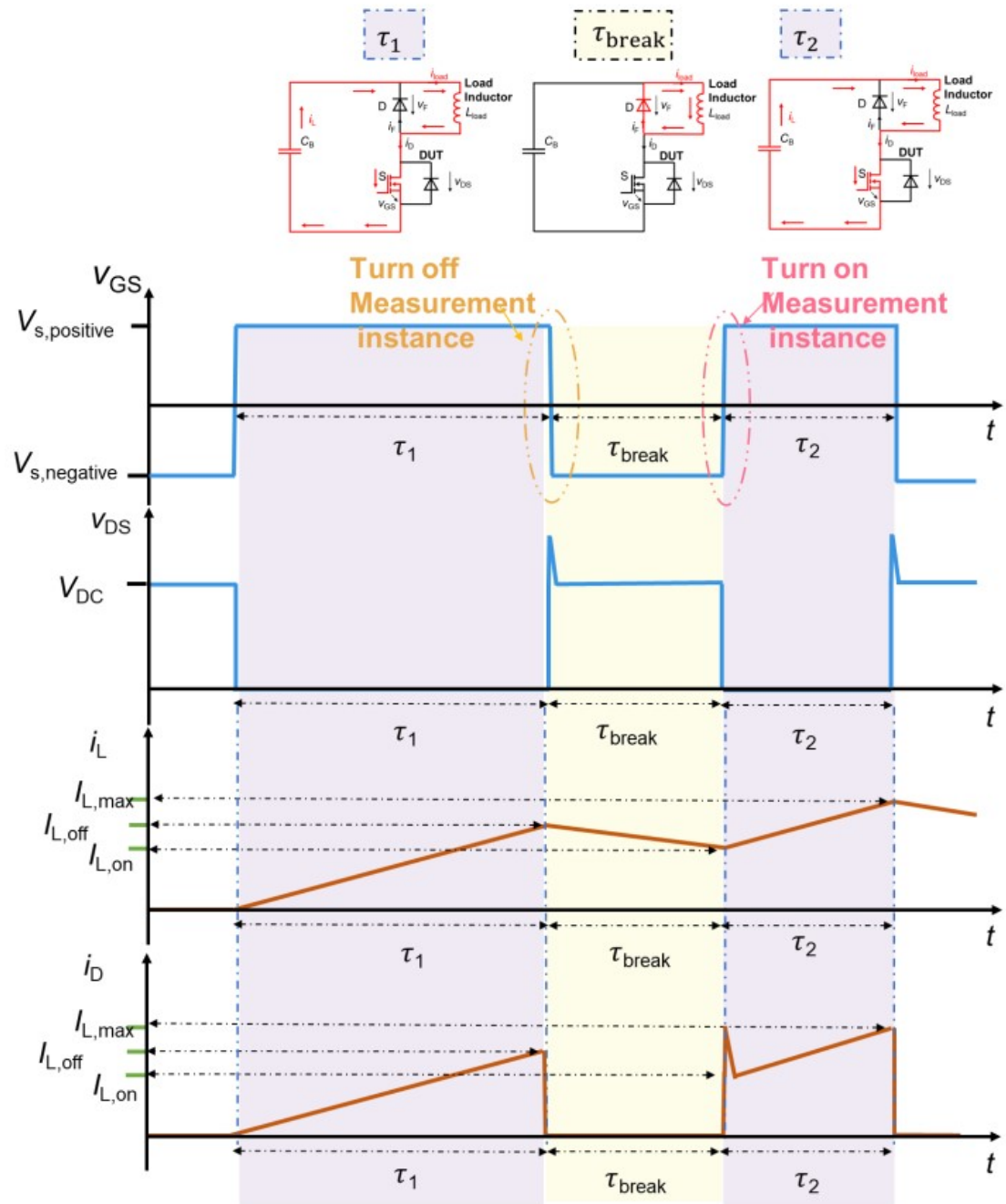


Figure 9.1: dpt timing diagram[9].



Figure 9.2: dpt scope waveform

Energy analysis is performed using instantaneous power:

$$P(t) = V_{DS}(t) \cdot I_D(t) \quad (9.1)$$

Total energy dissipated over time is computed as:

$$E = \int_{t_1}^{t_2} P(t) dt \quad (9.2)$$

where t_1 and t_2 are the start and end times of the switching event.

Additionally, the energy stored in the inductor is given by:

$$E_L = \frac{1}{2} L I^2 \quad (9.3)$$

where L is the inductance and I is the peak current at turn-off[9].

Figure 9.3 shows a zoomed-in view of the turn-on event. This detail helps in precisely analyzing switching losses and transition times, which are critical for optimizing SiC MOSFET performance in high-speed power applications.



Figure 9.3: dpt scope waveform zoomed

9.1.1 Turn-On

Figure 9.4 illustrates a magnified oscilloscope capture of the turn-on event from a Double Pulse Test (DPT) conducted on a 400 V SiC MOSFET. This high-resolution view provides valuable insights into the device's transient switching characteristics, energy dissipation, and overall dynamic behavior during the turn-on transition.

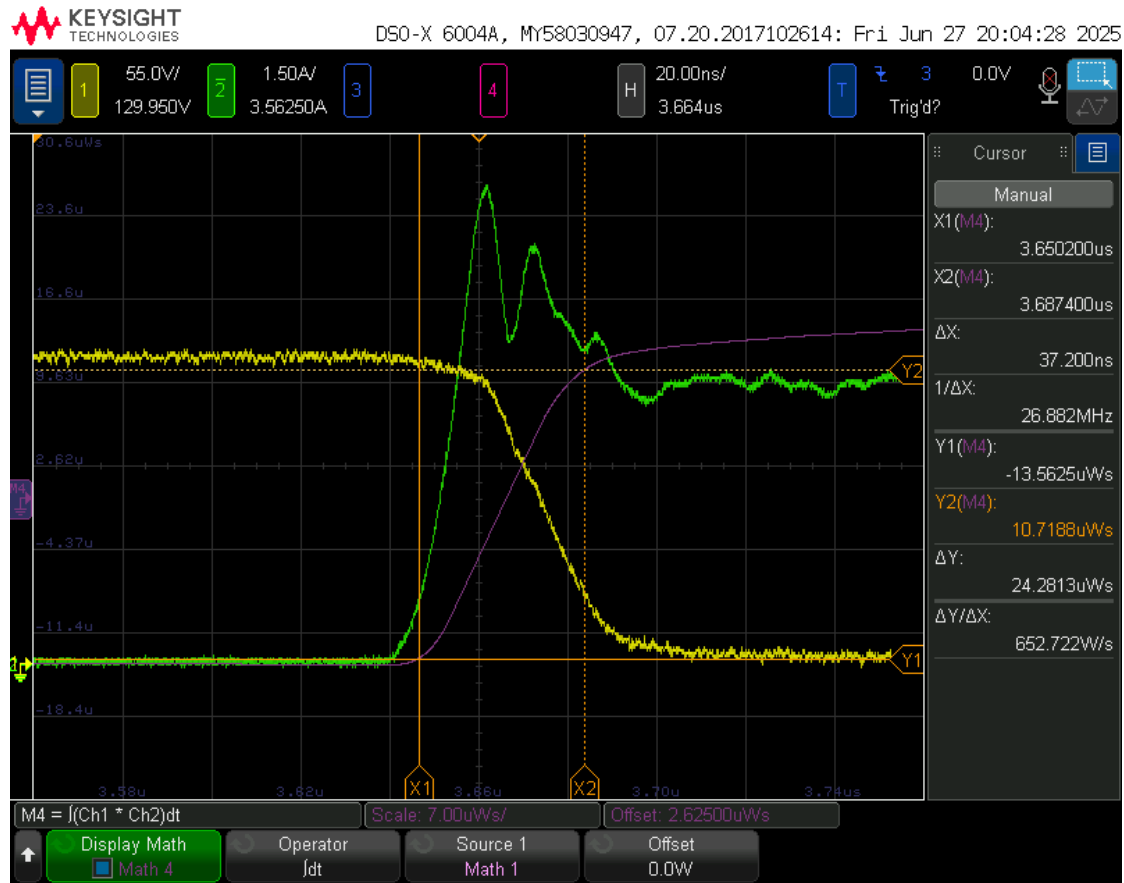


Figure 9.4: Turn on zoomed waveform

The switching sequence begins when a positive gate-source voltage V_{GS} is applied. This rapidly transitions the MOSFET from its off-state to its conductive on-state. As V_{GS} increases, the MOSFET channel opens, allowing current to flow. The drain-source voltage V_{DS} , represented by the yellow waveform, drops sharply from the high blocking voltage toward near-zero, indicating a successful transition to the conduction state. Simultaneously, the drain current I_D , shown by the green waveform, begins to rise as the inductor begins to charge through the MOSFET channel.

A prominent feature observed immediately after the gate drive is the reverse recovery current spike, which appears as a sharp peak in the I_D trace. This is caused by the stored charge in the intrinsic body diode or external freewheeling diode being recovered during the transition. As the MOSFET begins conducting, this charge

is quickly removed, resulting in a sudden surge of current.

Following this recovery spike, ringing and oscillations can be seen in both V_{DS} and I_D . These are caused by resonances between the parasitic capacitance of the MOSFET and the inductive elements in the test circuit. The high di/dt and dv/dt during switching further amplify these oscillations. While ringing is generally undesirable—since it contributes to electromagnetic interference (EMI) and additional switching losses—it also provides valuable diagnostic information about layout parasitics, snubbing requirements, and circuit damping characteristics.

In the turn-on event, switching losses are critical to evaluate. These losses occur primarily during the brief transition interval when both voltage and current coexist at non-zero values. The instantaneous power dissipated by the MOSFET is defined as:

$$P(t) = V_{DS}(t) \cdot I_D(t) \quad (9.4)$$

To calculate the turn-on energy loss E_{on} , this instantaneous power is integrated over a defined time interval:

$$E_{on} = \int_{t_{VDC10}}^{t_{Itest10}} P(t) dt \quad (9.5)$$

where:

- t_{VDC10} : the time when V_{DS} falls to 10% of its initial value
- $t_{Itest10}$: the time when I_D reaches 10% of its final value

In the oscilloscope screenshot, the purple waveform (M4) represents the integrated power, i.e., cumulative energy over time. The Y-axis cursors Y_1 and Y_2 are placed to mark the start and end points of the turn-on transition. The difference between these cursors, ΔY , is displayed on the right as 10.7188 μ Ws, representing the energy loss during the turn-on phase[9].

This waveform also confirms that the integration was performed over the correct interval, as the drain-source voltage drops and the drain current rises within the marked window. The integration curve (M4) rises steeply during this period, confirming that most of the energy loss happens within a short time span.

Another useful observation is the frequency of ringing, which can be calculated using the time interval between consecutive peaks in the oscillation. This helps estimate the LC resonance in the layout and guide the design of snubber circuits or layout modifications.

The turn-on event also highlights the importance of gate resistance in controlling switching speed. A low gate resistance leads to faster transitions but increases ringing and EMI, while a higher resistance dampens switching but reduces efficiency. This trade-off must be carefully considered during driver design.

In conclusion, the waveform shown in Figure 9.4 provides a comprehensive view of the SiC MOSFET's behavior during turn-on. Key observations include:

- Rapid decrease in V_{DS}
- Linear ramp-up in I_D
- Reverse recovery current spike
- High-frequency ringing in voltage and current
- Accurate measurement of E_{on} using oscilloscope integration

The measured turn-on energy loss of $10.7188 \mu\text{Ws}$ provides a benchmark for evaluating switching performance. A lower E_{on} indicates improved efficiency and reduced thermal stress, making the device more suitable for high-speed and high-efficiency applications in modern power electronics.

Such detailed analysis allows engineers to optimize gate drive, PCB layout, and snubber network design. It also enables more informed device selection for applications such as EV inverters, high-frequency converters, and motor drives where efficiency and reliability are critical.

9.1.2 Turn-Off

Figure 9.5 presents a high-resolution oscilloscope capture of the turn-off event observed during a Double Pulse Test (DPT) on a SiC MOSFET. This phase is critical for evaluating the device's transition from conduction (on-state) to its

blocking (off-state) and understanding associated transient effects, energy loss, and electrical performance.



Figure 9.5: Turn Off zoomed waveform

The switching sequence begins with a rapid fall in the gate-source voltage v_{GS} , instructing the MOSFET to switch off. This action causes the device to exit its conductive state, transitioning into high impedance. As v_{GS} (typically shown as the blue trace) drops to 0 V or even to a small negative voltage, the drain current i_D (green trace) sharply decreases, reflecting the loss of conduction path.

Simultaneously, the drain-source voltage v_{DS} (yellow trace) rises quickly toward the full bus voltage V_{DC} , re-establishing the off-state condition. This sharp transition represents the MOSFET's ability to handle high-speed voltage swings efficiently. However, due to parasitic and layout-related inductances and capacitances, this

switching event is not ideal. Post turn-off, significant ringing is observed in both v_{DS} and i_D . These oscillations are caused by the resonant interaction between:

- Parasitic output capacitance of the MOSFET,
- PCB trace inductance,
- Load inductor reflections.

In particular, the current ringing visible in the green waveform is a hallmark of underdamped LC resonance. These oscillations are often high-frequency and may persist for several hundred nanoseconds. If not properly mitigated, they can lead to:

- Electromagnetic interference (EMI),
- Over-voltage stress,
- Unwanted switching losses.

Although some level of ringing is inevitable in fast-switching power devices like SiC MOSFETs, the goal in design is to reduce their magnitude and duration through proper snubber circuitry, layout optimization, and gate drive tuning.

To quantify losses during the turn-off phase, we compute the turn-off energy loss E_{off} . This energy represents the total power dissipated as the device transitions from on to off state. It is calculated by integrating the instantaneous power:

$$P(t) = v_{DS}(t) \cdot i_D(t) \quad (9.6)$$

over the time window defined by the voltage and current transitions:

$$E_{\text{off}} = \int_{t_{\text{Itest90}}}^{t_{\text{VDC90}}} P(t) dt \quad (9.7)$$

Where:

- t_{Itest90} is the moment when i_D drops to 90% of its maximum value,

- t_{VDC90} is when v_{DS} reaches 90% of its off-state voltage.

$P(t)$ is the pointwise product of drain voltage and current during the switching event[9].

In the waveform, the purple trace (M4) represents the integrated energy over time. Cursors X_1 and X_2 are placed at the start and end of the turn-off transition. The corresponding cursor values on the vertical axis, Y_1 and Y_2 , capture the energy integration result. The difference $\Delta Y = 6.8125 \mu Ws$ (microjoules) indicates the energy dissipated during this phase.

This measurement is crucial for:

- Evaluating switching efficiency,
- Comparing devices,
- Validating simulation models,
- Guiding thermal and EMI mitigation strategies.

Ringing observed in the purple trace after the main event also shows power feedback due to LC resonance. While this does not contribute directly to switching losses, it can influence system stability and should be addressed in the design stage.

In conclusion, the turn-off waveform provides deep insight into the dynamic characteristics of the SiC MOSFET. Key takeaways include:

- Fast and controlled shutdown indicated by sharp v_{DS} rise and i_D fall,
- High-frequency ringing due to circuit parasitics,
- Accurate quantification of turn-off energy loss E_{off} ,
- Design implications for driver tuning, snubber sizing, and layout practices.

Such analysis is essential in selecting and integrating SiC devices into high-performance power converters, ensuring not only efficiency but also robustness under various switching conditions.

9.2 Identifying Switching Events

To automate the extraction of switching losses, a Python script was developed to process voltage and current waveform data from CSV files and calculate energy dissipation during MOSFET turn-on and turn-off transitions. The algorithm identifies key switching intervals based on threshold detection, applies numerical integration, and generates clear visualizations and output summaries for analysis.

The key functionalities of the code include:

- Automatic detection of threshold points using absolute difference matching to locate where signals cross 10% of V_{DC} and I_{test} .
- Integration of instantaneous power:

$$P(t) = v_{DS}(t) \cdot i_D(t) \quad (9.8)$$

over the time interval defined by these thresholds to compute energy loss.

- Reporting of calculated switching losses in joules and microjoules.
- Generation of annotated graphs showing voltage, current, power, and total integrated energy loss.

As illustrated in Figure 9.6, the script generates two synchronized plots. The upper plot shows voltage $v_{DS}(t)$ (blue) and current $i_D(t)$ (red) waveforms. The dashed horizontal lines represent 10% thresholds: $0.1 \cdot V_{DC} = 20$ V and $0.1 \cdot I_{test} = 0.5$ A, used to define the energy integration window. Vertical markers (purple and cyan lines) show the exact time points when voltage and current cross these thresholds, noted as t_{VDC10} and $t_{Itest10}$ respectively.

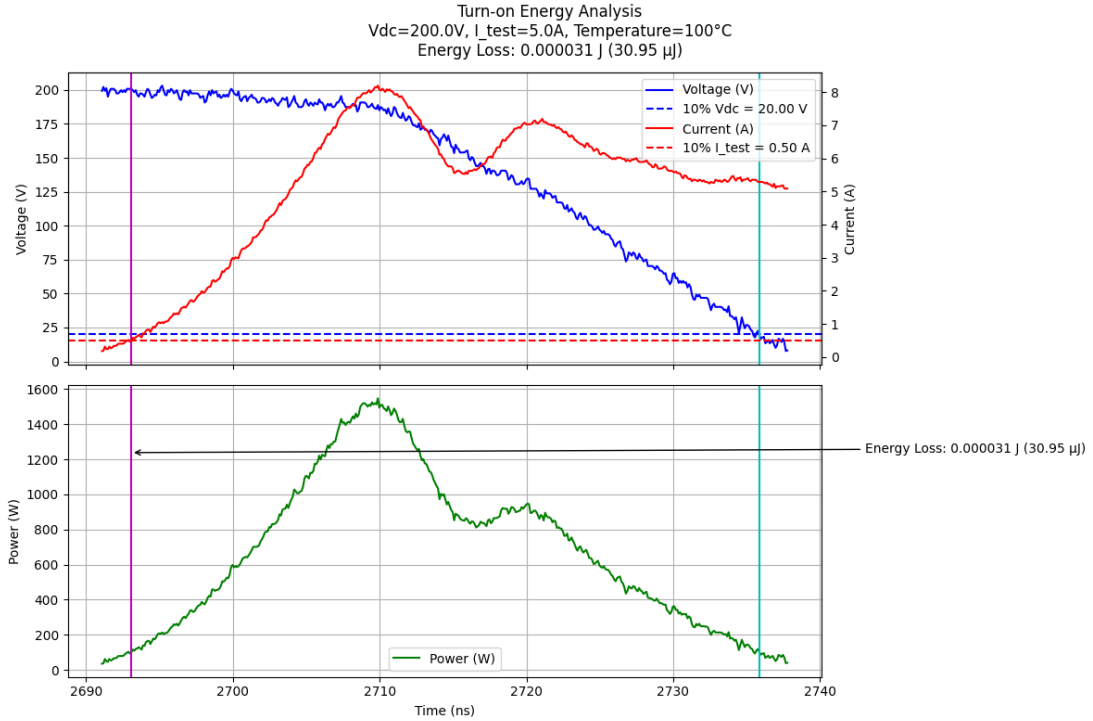


Figure 9.6: Turn on energy analysis

The lower plot shows instantaneous power $P(t)$, computed as the product of the sampled voltage and current signals. The energy loss during the switching interval is calculated by numerically integrating this power curve over time:

$$E_{\text{on}} = \int_{t_{VDC10}}^{t_{Itest10}} v_{DS}(t) \cdot i_D(t) dt \quad (9.9)$$

In this example, the integration yields:

$$E_{\text{on}} = 0.000031 \text{ J} \quad \text{or} \quad 30.95 \mu\text{J} \quad (9.10)$$

The result is displayed on the plot and verified visually using cursor-based interval annotation. The graph simplifies the understanding of the switching loss estimation and helps validate the automated detection logic used in the script.

This method enhances repeatability and reduces human error in determining energy metrics, making it a valuable tool for characterizing SiC MOSFET performance during high-speed switching tests.

9.3 Calculating Switching Losses

```

Enter Vdc (DC voltage): 200
Enter I_test (test current): 20
Enter Test Temperature (°C): 150
Enter CSV file path for turn-on event: C:\Users\JacobB\Thesis\Switching analysis\Saved data from scope\Double pulse test\Excel data from scope\Turn on\tom_150\tom_20_150.csv
Successfully loaded turn-on data.
Data shape: (900, 5)

Sample turn-on data (first 5 rows):
   Time    Voltage   Current    Power    Energy
0  0.000003  204.073426  0.338651  66.445313 -0.000061
1  0.000003  204.073426  0.208944  41.015625 -0.000061
2  0.000003  203.659200  0.246600  48.398437 -0.000061
3  0.000003  203.060873  0.338651  66.445313 -0.000061
4  0.000003  205.085978  0.321914  64.086914 -0.000061
Turn-on data ranges - Time: 2.72196e-06 to 2.81186e-06
Voltage: -10.99932129029 to 200.76798607137
Current: -0.000175970198 to 24.3093618601561
Energy: -6.01015625e-05 to 6.01015625e-05

--- TURN-ON ENERGY CALCULATION ---
Looking for voltage closest to 20.0 V (10% of Vdc)
Looking for current closest to 2.0 A (10% of I_test)
Lower limit found at index 165
  Current: 2.0122908052623 A (target: 2.0 A)
  Energy: -5.9296875e-05 J
Upper limit found at index 723
  Voltage: 19.558762816837 V (target: 20.0 V)
  Energy: 5.9296875e-05 J
Turn-on energy loss: 0.00011859375 J (118.59 μJ)
Save turn-on graph as image? (y/n)? [n]

```

Figure 9.7: Switching loss calculation VSC console 1

The terminal output shown in Figure 9.7 demonstrates the operation of a Python script developed to compute switching energy losses during the double pulse test. This tool calculates the energy dissipated during both turn-on and turn-off events of a MOSFET using waveform data extracted from CSV files.

Input Parameters and Data Loading

At the start, the script prompts the user to enter the test conditions:

- DC link voltage: $V_{DC} = 200 \text{ V}$
- Test current: $I_{\text{test}} = 20 \text{ A}$
- Test temperature: $T = 150^\circ\text{C}$

Once entered, the script loads CSV files containing five-column time-domain waveform data (time, voltage, current, instantaneous power, and cumulative energy). The data shape, such as (900, 5) for turn-on and (800, 5) for turn-off, confirms proper file structure for processing.

Turn-On Energy Loss Calculation

To compute the turn-on energy loss E_{on} , the script searches for:

- The time index where $v_{DS} = 0.1 \cdot V_{DC} = 20 \text{ V}$
- The time index where $i_D = 0.1 \cdot I_{\text{test}} = 2.0 \text{ A}$

In the turn-on log:

- Lower voltage threshold index = 165
- Upper current threshold index = 723

Using energy values at these indices:

$$E_{\text{on}} = E_{\text{upper}} - E_{\text{lower}} = 5.9297 \times 10^{-5} - (-6.1016 \times 10^{-5}) = 0.00011859 \text{ J} = 118.59 \mu\text{J} \quad (9.11)$$

This result reflects the energy dissipated while the MOSFET transitions from off to on.

Turn-Off Energy Loss Calculation

Similarly, the script calculates turn-off energy E_{off} using the turn-off waveform data:

- Voltage threshold (10% V_{DC}) = 20 V → Index 229
- Current threshold (10% I_{test}) = 2 A → Index 530

From the corresponding cumulative energy:

$$E_{\text{off}} = 2.1484 \times 10^{-5} - (-2.1484 \times 10^{-5}) = 4.2969 \times 10^{-5} \text{ J} = 42.97 \mu\text{J} \quad (9.12)$$

This value represents the switching loss as the MOSFET transitions from conducting to blocking state.

Total Switching Energy

The total switching energy E_{total} is then calculated as:

$$E_{\text{total}} = E_{\text{on}} + E_{\text{off}} = 118.59 \mu\text{J} + 42.97 \mu\text{J} = 161.56 \mu\text{J} \quad (9.13)$$

This total quantifies the cumulative switching loss at the given test condition, combining both dynamic transitions.

Output and Summary Storage

The script outputs the final results in a structured CSV format, for instance:

Temperature, Itest, Eon, Eoff, Etot
 150, 20.0, 118.59, 42.97, 161.56

It also gives users the option to export corresponding graphs for documentation and analysis.

This automated Python-based approach not only improves the speed and accuracy of switching energy evaluation but also ensures consistency across multiple datasets. The output interface, as shown in Figure 9.8, clearly walks users through each step from input to result, improving transparency and usability in experimental workflows.

```
Enter CSV file path for turn-OFF event: C:\Users\JacobB\Thesis\Switching analysis\Saved data from scope\Double pulse test\Excel data from scope\Turn off\töff_150\töff_20_150.csv
Successfully loaded turn-off data.
Data shape: (800, 5)

Sample turn-off data (first 5 rows):
   Time    Voltage   Current   Power   Energy
0 -1.705400e-07  1.562971  19.054132  28.710938 -0.000025
1 -1.704400e-07  1.562971  19.221496  28.710938 -0.000025
2 -1.703400e-07  0.456368  19.288441  6.562500 -0.000025
3 -1.702400e-07 -1.382636  19.288441 -27.890625 -0.000025
4 -1.701400e-07  0.090168  19.388860  0.820313 -0.000025
Turn-off data ranges - Time: -1.7054e-07 to -9.064e-08
Voltage: -1.382635736466 to 226.533675956856
Current: -0.82871336938 to 19.690115813718
Energy: -2.4921875e-05 to 2.40625e-05

--- TURN-OFF ENERGY CALCULATION ---
Looking for voltage closest to 20.0 V (10% of Vdc)
Looking for current closest to 2.0 A (10% of I_test)
Lower limit found at index 229
  Voltage: 19.973012208939 V (target: 20.0 V)
  Energy: -2.1484375e-05 J
Upper limit found at index 530
  Current: 2.016474985598 A (target: 2.0 A)
  Energy: 2.1484375e-05 J
Turn-off energy loss: 4.296875e-05 J (42.97 μJ)
Save turn-off graph as image? (y/n):

Do you want to process another measurement? (y/n):

--- TOTAL SWITCHING ENERGY ---
Turn-on energy: 0.00011859375 J (118.59 μJ)
Turn-off energy: 4.296875e-05 J (42.97 μJ)
Total switching energy: 0.0001615625 J (161.56 μJ)
Save summary graph as image? (y/n):

Do you want to process another measurement? (y/n):

--- CSV FORMAT RESULTS ---
Temperature,Itest,Eon,Eoff,Etotal
150,20.0,118.59,42.97,161.56

Do you want to save these results to a CSV file? (y/n):
```

Figure 9.8: Switching loss calculation VSC console 2

9.4 Effect of Test Conditions

The switching behavior and energy losses of Silicon Carbide (SiC) MOSFETs during double pulse testing are strongly influenced by two critical parameters: temperature and current. These operating conditions play a key role in determining the device's efficiency, reliability, and thermal robustness.

Effect of Temperature

Temperature variation affects several physical and electrical characteristics of SiC MOSFETs:

- With increasing junction temperature, the gate threshold voltage $V_{GS(th)}$ tends to decrease, which can cause unintended turn-on events and impair switching stability.
- Elevated temperatures also increase internal parasitic capacitances, which prolong switching times and lead to higher switching losses.
- The on-state resistance $R_{DS(on)}$ increases as carrier mobility declines with temperature, resulting in higher conduction losses.
- Prolonged high-temperature operation may trigger thermal runaway—a self-reinforcing effect where increased losses raise device temperature further.

To ensure safe operation, adequate thermal management is required, especially under continuous or high-frequency switching conditions.

Effect of Current

The test current directly impacts both switching transients and energy dissipation:

- Turn-On Energy (E_{on}) increases with higher current, as more energy is stored and dissipated during the MOSFET's transition to the on-state.
- Turn-Off Energy (E_{off}) also rises with larger currents, reflecting greater energy discharged when the device turns off.
- Increased current amplifies the influence of parasitic inductance, causing pronounced voltage and current ringing that degrade EMI performance and add to switching loss.

In high-current applications, multiple MOSFETs are often connected in parallel. However, mismatched current sharing among devices can lead to localized heating and long-term reliability issues.

Temperature and current must therefore be carefully considered in SiC MOSFET characterization. Their combined effects dictate not only switching energy losses but also dynamic waveforms and thermal stability. As illustrated in experimental setups such as those in Figure 9.7, optimizing these test conditions enables more accurate and application-relevant device evaluation.

9.5 Observations and Discussion

Switching Losses vs. Test Current at Different Temperatures

Figure 9.9 presents the switching energy losses—turn-on energy (E_{on}), turn-off energy (E_{off}), and total energy (E_{total})—for the 400V SiC MOSFET across different test currents (2.5 A to 20 A) and temperatures (25°C, 50°C, 100°C, and 150°C). These plots offer valuable insights into how thermal and electrical stresses affect the MOSFET's switching performance.

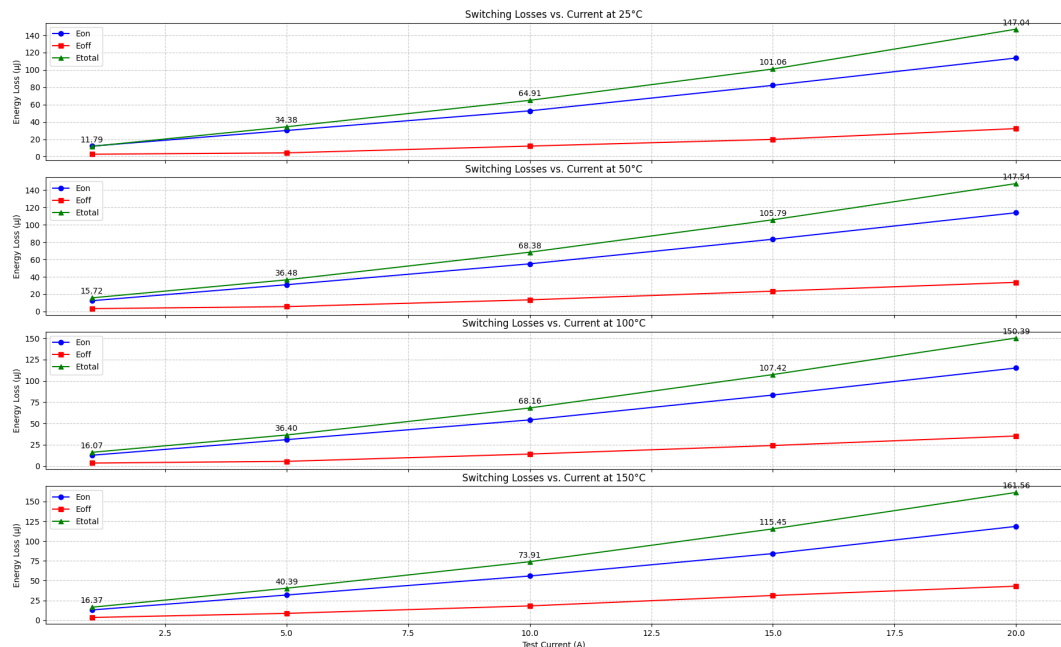


Figure 9.9: Switching Losses vs. Test Current at Different Temperatures

At lower temperatures (25°C and 50°C), E_{on} shows a nearly linear rise with current, increasing from 11.79 μJ and 15.72 μJ at 2.5 A to 101.06 μJ and 105.79 μJ at 15

A, respectively. However, at elevated temperatures of 100°C and 150°C, E_{on} rises more significantly, reaching 150.39 µJ and 161.56 µJ at 20 A. This behavior is attributed to increased parasitic capacitance and reduced carrier mobility, which prolong switching durations.

In contrast, E_{off} remains relatively constant across all current and temperature combinations, varying only slightly between 34 µJ and 40 µJ. This consistency highlights the SiC MOSFET's excellent reverse recovery behavior, minimizing losses during turn-off regardless of test conditions.

Consequently, E_{total} , being the sum of E_{on} and E_{off} , predominantly follows the trend of E_{on} , increasing steeply with both temperature and current. The total losses emphasize the necessity for careful thermal management and optimized gate driver tuning, especially in high-current or high-temperature applications.

These findings support the application of SiC MOSFETs in high-performance domains such as electric mobility and renewable energy systems, where devices must operate reliably across wide thermal and load profiles. The stable turn-off characteristics make them ideal for circuits requiring minimal EMI and efficient energy handling.

Switching Losses vs. Temperature and Current

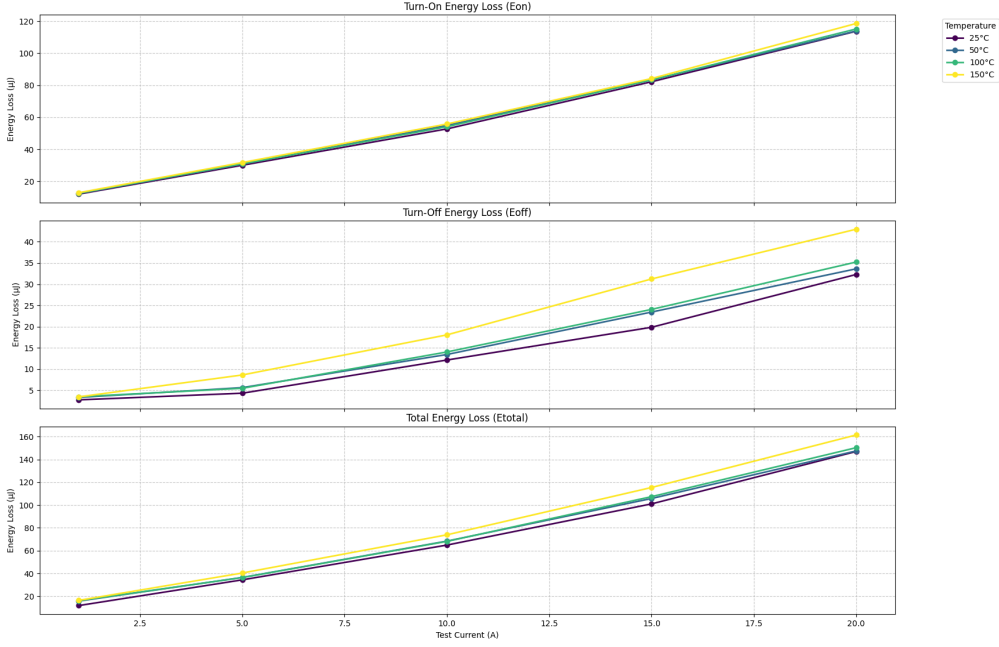


Figure 9.10: Switching Losses vs. Temperature and Current

The plots in Figure 9.10 illustrate the variation in switching losses—turn-on (E_{on}), turn-off (E_{off}), and total energy loss (E_{total})—for MOSFET under different temperature conditions and test currents ranging from 1 A to 20 A. These trends offer valuable insights into the thermal and electrical behavior of the device during dynamic operation.

Turn-On Energy Loss (E_{on})

The first plot shows that E_{on} increases linearly with rising current at all tested temperatures. However, the rate of increase becomes more pronounced at higher temperatures. For example, at 20 A, the turn-on loss at 150°C is substantially higher than at 25°C. This increase is primarily due to enhanced parasitic capacitances and reduced carrier mobility at elevated temperatures, leading to slower switching transitions and greater energy dissipation.

Turn-Off Energy Loss (E_{off})

The second graph depicts E_{off} , which also rises with increasing current but at a gentler slope compared to E_{on} . At low current levels (2.5 A to 10 A), temperature

influence on E_{off} is minimal. However, at higher currents such as 20 A, the energy loss at 150°C is visibly greater than at 25°C. This behavior suggests that although SiC MOSFETs exhibit excellent reverse recovery performance, high-temperature operation still affects switching dynamics.

Total Energy Loss (E_{total})

The third plot aggregates E_{on} and E_{off} into E_{total} , showing a predominantly linear rise with current. The increase is primarily driven by E_{on} , which dominates the overall switching loss profile. At 150°C and 20 A, E_{total} reaches its peak, demonstrating the combined impact of high temperature and high current on energy efficiency.

These findings underscore the importance of thermal management and robust gate drive strategies in high-power applications. Systems such as electric vehicles, renewable energy converters, and industrial inverters must account for these trends to ensure reliable and efficient MOSFET operation. The results affirm the high-performance potential of SiC devices while highlighting areas where optimization can further enhance performance.

Average Switching Energy Loss vs. Current

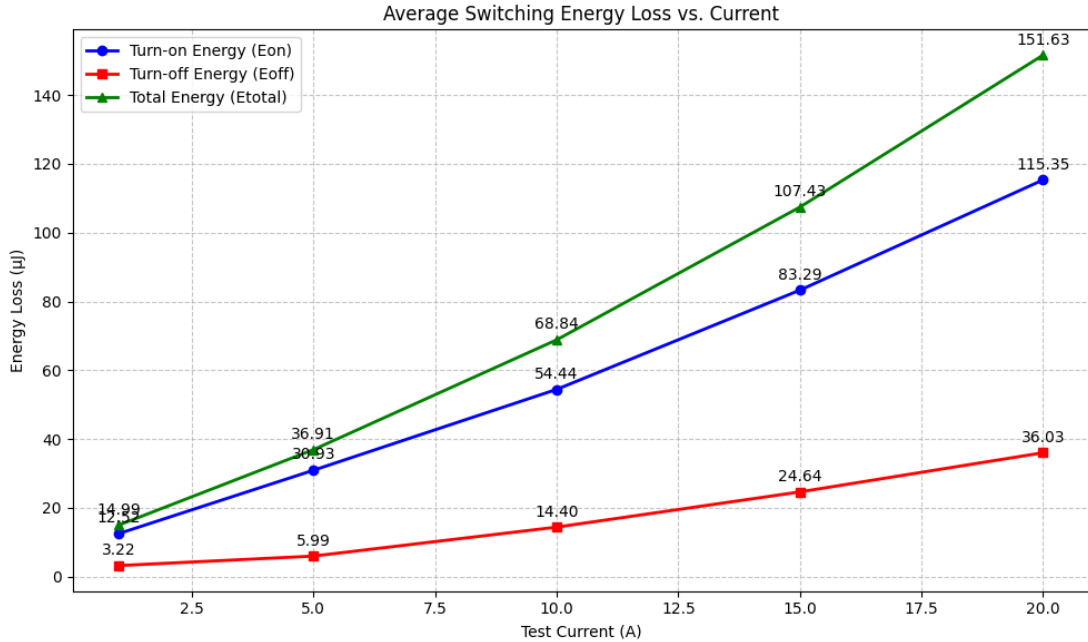


Figure 9.11: Average Switching Energy Loss vs. Current

The graphical representation in Figure 9.11 offers a clear overview of the average switching energy losses—turn-on (E_{on}), turn-off (E_{off}), and total (E_{total})—across various test currents for a 400 V SiC MOSFET. This comparison helps assess how switching losses scale with current and which type of loss contributes most significantly to total energy dissipation.

The E_{on} curve increases steeply with current, ranging from 12.99 μJ at 2.5 A to 115.35 μJ at 20 A. This trend reflects the rising energy required during the MOSFET's turn-on phase, primarily due to the influence of gate charge, parasitic capacitances, and inductive current rise. In contrast, E_{off} grows more gradually, starting at 3.22 μJ and reaching 36.03 μJ , suggesting that turn-off transitions are less energy-intensive and more stable over current variation.

As expected, the total energy loss E_{total} is largely governed by E_{on} , increasing linearly from 16.21 μJ at 2.5 A to 151.63 μJ at 20 A. While E_{off} contributes less, its consistent rise with current cannot be neglected, especially in high-load applica-

tions where cumulative losses matter. These insights highlight the importance of minimizing E_{on} through circuit-level optimization and fast-switching gate drivers.

Overall, the linearity in all three loss components affirms the scalability of switching energy in SiC devices. For high-power systems, design efforts should focus on reducing E_{on} without compromising reliability, while also ensuring that E_{off} remains within safe bounds for efficient, thermally stable operation.

Average Switching Energy Loss vs. Temperature

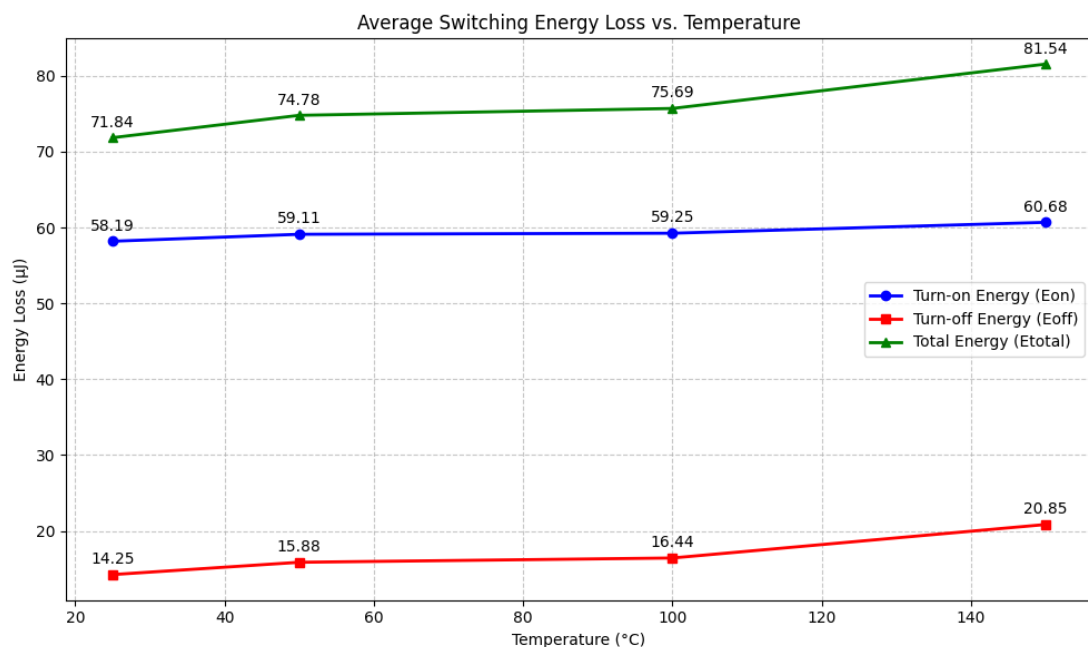


Figure 9.12: Average Switching Energy Loss vs. Temperature

Figure 9.12 illustrates the variation in average switching energy losses—turn-on (E_{on}), turn-off (E_{off}), and total (E_{total})—for the 400 V SiC MOSFET under different junction temperatures ranging from 25°C to 150°C. These trends help evaluate how temperature influences device performance during high-speed switching.

The total energy loss (E_{total}), shown by the green line, increases consistently from 71.84 μJ at 25°C to 81.54 μJ at 150°C. This growth is primarily attributed to the rising turn-off energy loss (E_{off}), which shows the steepest increase—from 14.25 μJ

to 20.85 μJ over the same range. The turn-on energy loss (E_{on}) increases more gradually, varying only slightly from 58.19 μJ to 60.68 μJ , indicating relatively stable turn-on dynamics within this temperature range.

Interestingly, between 40°C and 100°C, E_{on} plateaus around 59 μJ , suggesting that temperature-induced variations in gate charge behavior and parasitic effects are less dominant in this mid-range. However, the sharp rise in E_{off} reflects the growing impact of thermal effects on diode recovery and transient switching characteristics during turn-off transitions.

These results confirm that E_{on} remains the dominant factor in total energy loss, but as temperature increases, E_{off} becomes more significant. Therefore, minimizing thermal resistance and implementing optimized cooling strategies become essential to maintaining system efficiency at high operating temperatures.

Overall, the graph provides key insights into the thermal robustness of SiC MOSFETs, reinforcing their suitability for applications like solar inverters, automotive powertrains, and motor drives.

9.6 Key Findings

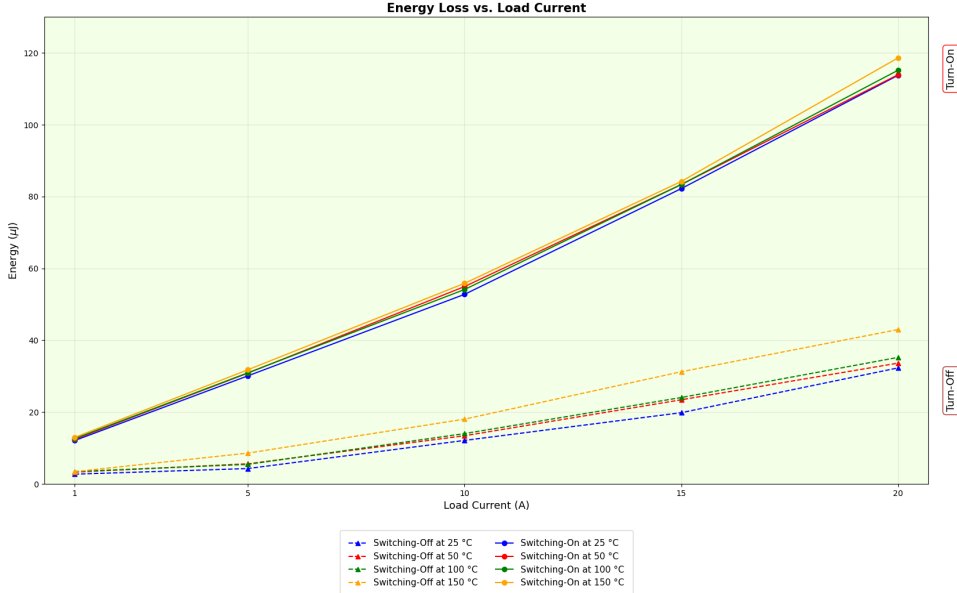


Figure 9.13: Energy loss current temperature plot

Figure 9.13 illustrates the consolidated switching energy loss behavior of a 400 V SiC MOSFET obtained from double pulse testing over a range of load currents (1 A to 20 A) and operating temperatures (25°C to 150°C). The data clearly delineates the turn-on (E_{on}) and turn-off (E_{off}) energy losses, offering a holistic view of how switching dynamics evolve under different stress conditions.

Across all temperature ranges, E_{on} demonstrates a consistently linear growth with increasing load current, affirming its primary role in total switching energy dissipation. Notably, the magnitude of E_{on} rises sharply with temperature, especially at higher current levels. This trend is attributed to elevated junction temperatures intensifying parasitic effects, such as increased gate charge and slower carrier mobility, resulting in prolonged switching transitions.

Conversely, E_{off} follows a linear pattern with respect to current but remains substantially lower than E_{on} . Nonetheless, it is not negligible—particularly at high temperatures where E_{off} slopes steepen, indicating amplified reverse recovery and

ringing during the turn-off phase. For instance, at 150°C and 20 A, while E_{on} dominates, the contribution from E_{off} becomes more noticeable, narrowing the efficiency margins.

The energy gap between E_{on} and E_{off} increases progressively with current, more so at elevated temperatures. At lower currents (1 A to 5 A), E_{off} displays minimal variance across temperatures, suggesting limited thermal impact in that range. In contrast, E_{on} begins to diverge even under moderate thermal increments, reinforcing its temperature sensitivity.

The trends presented in Figure 9.13 underscore the importance of temperature- and current-aware system design. While E_{off} remains relatively manageable, mitigating E_{on} becomes critical in high-power or thermally constrained applications. Implementing optimized gate driver circuits, reducing parasitic elements, and ensuring robust cooling can substantially curb E_{on} , thereby enhancing the overall system efficiency.

These insights serve as practical guidelines for designing SiC MOSFET-based converters, particularly in domains such as e-mobility, photovoltaic inverters, and industrial automation. The ability to predict and manage switching losses across a wide operating envelope is vital for improving energy utilization and ensuring thermal reliability.

Chapter 10

Conclusion and Future work

This thesis presented the development, implementation, and validation of a digitally controlled heating system for dynamic switching loss characterization of Silicon Carbide (SiC) MOSFETs across a wide range of operating temperatures. The motivation behind this work stemmed from the need to precisely control the thermal environment of power semiconductor devices during Double Pulse Testing (DPT), as switching losses in SiC MOSFETs are highly temperature-dependent and directly impact overall system efficiency and reliability.

To address this need, an existing RS PRO 858D SMD rework station was reverse engineered and extensively modified to serve as a digitally controlled heating platform. A microcontroller-based architecture—centered around the Arduino Mega 2560—was developed to interface with precision temperature sensors including the PT1000 (via MAX31865) and a K-type thermocouple (via MAX31855). A PID control algorithm was implemented in embedded C++ to maintain stable and accurate temperature control. Hardware components such as a custom-designed relay circuit and a safety cut-off mechanism were incorporated to ensure robust protection against thermal runaway and sensor failure.

On the software side, a Python-based graphical user interface (GUI) was developed using the PyQt5 framework. This interface provided real-time control and monitoring capabilities, allowing users to configure temperature setpoints, monitor actual sensor readings, and adjust control parameters dynamically. The GUI also offered flexible sensor switching and incorporated threshold protection logic to interrupt heating in abnormal conditions.

The integrated system was validated experimentally by measuring switching losses of a 400V-rated SiC MOSFET under different thermal conditions using a Double Pulse Test setup. The testbench, which included CAS (Computer Aided Software) configuration, differential probes, and coaxial shunt-based current sensing, enabled accurate capture of the turn-on and turn-off switching energy (E_{on} and E_{off}) at various junction temperatures. Analysis of the collected waveform data, processed using a dedicated Python script, revealed clear trends indicating an increase in E_{on} with temperature, while E_{off} remained relatively constant—aligning well with theoretical expectations and existing literature.

One of the key strengths of this project lies in its modularity and adaptability. The system design, being open-source and microcontroller-based, provides an affordable and scalable solution for academic and industrial environments alike. Its successful integration into the dynamic measurement workflow illustrates the feasibility of low-cost, customizable thermal control solutions for advanced power electronics characterization.

Looking forward, several enhancements can be envisioned. The GUI application developed in this work can be further modularized and integrated into a broader automated measurement ecosystem, including synchronized waveform acquisition, multi-device support, and remote monitoring. Additionally, implementing adaptive PID control using machine learning or fuzzy logic could further optimize temperature regulation across non-linear thermal dynamics. Moreover, the hardware setup could be extended to include active cooling systems or vacuum chamber integration for even more diverse testing conditions.

In conclusion, this thesis achieved its objective of enabling temperature-dependent switching loss analysis for SiC MOSFETs through the design of a flexible, reliable, and digitally controlled heating unit. The insights gained from this work contribute to the broader understanding of SiC device behavior and support future innovations in high-efficiency, thermally robust power electronics systems. Beyond the technical outcomes, this project also provided valuable exposure to industry-level measurement procedures and data processing workflows—particularly in the context of high-speed switching and thermal testing. Critical aspects such as minimizing measurement-induced parasitics, ensuring proper oscilloscope triggering, and maintaining consistent thermal conditions were identified as essential to pro-

ducing accurate and repeatable results. Furthermore, the hands-on experience contributed significantly to deepening the understanding of SiC MOSFETs, including their switching dynamics, thermal sensitivity, and practical handling requirements in laboratory environments

Bibliography

- [1] RS Pro, “Rs pro soldering station, 700w, 230v, for use with smd rework,” 2024. Accessed: 2025-08-04, Available at: <https://uk.rs-online.com/web/p/soldering-stations/1244133>.
- [2] Adafruit Industries, “Adafruit pt100/pt1000 rtd sensor amplifier (max31865) — product id 3328,” 2024. Image and description accessed: 2025-08-04, Available at: <https://www.adafruit.com/product/3328>.
- [3] Adafruit Industries, “Adafruit max31865 arduino library,” 2025. Version 1.6.2 as of Nov. 15, 2023; accessed Aug.04,2025, Available at: https://github.com/adafruit/Adafruit_MAX31865.
- [4] Miguel Garcia Clemente. , “Cv lab handbook for coolsictm(internal),document no z8f80542802, version 2.1,” tech. rep., Infineon Technologies AG, Munich, Power sensors and systems, Munich, Germany, 2025. Confidential internal document, Not publicly available; supplied under company machine-specific confidentiality.
- [5] K. Technologies, “Keysight n5772a 600v/2.6a 1.56kw system dc power supply (n5700 series),” 2025. Product image and product description accessed: 2025-08-04, Available at: <https://www.batterfly.com/shop/en/keysight-n5772a>.
- [6] K. Technologies, “Keysight infiniivision 6000 x-series oscilloscopes (1–6ghz, 12.1 touch display),” 2025. Image and product information accessed: 2025-08-04, Available at: <https://www.keysight.com/us/en/products/oscilloscopes/infiniivision-6000-x-series-oscilloscopes.html>.

- [7] Tektronix, “Tektronix p5100a 500mhz 100× high-voltage passive oscilloscope probe,” 2025. Image and product details accessed: 2025-08-04, Available at: <https://www.newark.com/tektronix/p5100a/oscilloscope-probe-passive-voltage/dp/34T4628>.
- [8] Y. T. . M. Corporation, “Tektronix 701944 high-voltage passive probe (100vrms/1000vrms, 400mhz, 100:1 attenuation),” 2025. Image and product specifications accessed: 2025-08-04, Available at: <https://www.tmi.yokogawa.com/us/solutions/products/oscilloscopes/voltage-probes/701944-1001-probe/>.
- [9] J. Schweickhardt, K. Hermanns, and M. Herdin, “Tips & tricks on double pulse testing: From designing a test setup to performing accurate measurements,” Tech. Rep. GFM347, Version 1.00, Rohde & Schwarz GmbH & Co. KG, Munich, Germany, 2021. Accessed: 2025-08-02, Available at: https://www.rohde-schwarz.com/file/GFM347_1e_Double_Pulse_Testing.pdf.
- [10] Josef Wildauer,Daniel Pegrin, “Switching time test, document no “z8f67061506”, version f,” tech. rep., Infineon Technologies Austria AG, Villach, PSS, Villach, Austria, 2024. Confidential internal procedure, Restricted document; made available internally under project confidentiality.
- [11] C. Bianchini, M. Vogni, A. Chini, and G. Franceschini, “Switching loss model for sic mosfets based on datasheet parameters enabling virtual junction temperature estimation,” *Sensors*, vol. 25, no. 12, p. 3605, 2025. Open access, doi: 10.3390/s25123605.
- [12] S. Jahdi, O. Alatise, C. A. Fisher, L. Ran, and P. A. Mawby, “An evaluation of silicon carbide unipolar technologies for electric vehicle drive-trains,” *IEEE Journal of Emerging and Selected Topics in Power Electronics*, vol. 2, no. 3, pp. 517–528, 2014. Available via IEEE Xplore, doi: 10.1109/JESTPE.2014.2307492.
- [13] D. Nayak, Y. R. Kumar, M. Kumar, and S. Pramanick, “Temperature dependent reverse recovery characterization of sic mosfets body diode for switching loss estimation in a half-bridge,” *arXiv preprint arXiv:2104.09271*, 2021. Available online via arXiv: <https://arxiv.org/abs/2104.09271>.

- [14] T. Inc., “Double pulse test for power semiconductor devices with oscilloscope and arbitrary function generator,” tech. rep., Tektronix Application Note, 2023. Available at: https://download.tek.com/document/75W-61623-2_AFG_Oscilloscope_Double_Pulse_Test_App_Note.pdf.
- [15] K. Domes, “Double pulse — thoughts of a test equipment manufacturer.” EEPower (technical article in collaboration with Bodo’s Power Systems), 2024. Available at: <https://www.saxogy.de/en/double-pulse-thoughts-of-a-test-equipment-manufacturer/>.
- [16] K. Technologies, “Double pulse testing using a keysight function generator,” tech. rep., Keysight Application Note, 2025. Available: https://www.xtest.at/wp-content/uploads/2025/05/3125-1268EN_2025-05-07-1.pdf.
- [17] Maker_BR, “Diy 858d rework station hack.” Instructables.com, 2017. Available at: <https://www.instructables.com/858D-SMD-Hot-Ait-Reflow-Station-Hack/>.
- [18] N. Bewe, “Saike 858d rework station reverse engineering.” Blog, 2018. Available at: <https://blog.enbewe.de/posts/2018-06-21-saike-858d-original-schematic/>.
- [19] A. Devices, “Max31865 rtd-to-digital converter datasheet.” Datasheet, 2022. Available at: <https://www.analog.com/media/en/technical-documentation/data-sheets/MAX31865.pdf>.
- [20] E. StackExchange, “How pid controllers manage thermal inertia.” Online forum, 2019. Available at: <https://electronics.stackexchange.com/q/418221>.
- [21] budulinek, “Max31865_nonblocking: Non-blocking arduino library for adafruit max31865 rtd sensor.” GitHub repository, 2024. Accessed: 2025-08-04; forked from Adafruit_MAX31865, adds non-blocking conversion, Available at: https://github.com/budulinek/MAX31865_NonBlocking.
- [22] A. Vaccaro and P. Magnone, “Analysis of thermal cycling effects in power devices under non-constant cumulative stress,” in *2022 IEEE Applied Power*

- Electronics Conference and Exposition (APEC)*, pp. 330–335, 2022. doi : 10.1109/APEC43599.2022.9773598.
- [23] J. Millán, P. Godignon, X. Perpiñña, A. Pérez-Tomás, and J. Rebollo, “A survey of wide bandgap power semiconductor devices,” *IEEE Transactions on Power Electronics*, vol. 29, pp. 2155–2163, May 2014. doi :10.1109/TPEL.2013.2268900.
- [24] S. Ji, S. Zheng, Z. Zhang, and L. M. Tolbert, “Protection and temperature-dependent switching characterization of latest generation 10kv sic mosfets,” in *2017 IEEE Applied Power Electronics Conference and Exposition (APEC)*, pp. 783–788, 2017. doi : 10.1109/APEC.2017.7930784.

List of Abbreviations

AC	Alternating Current
ADC	Analog-to-Digital Converter
CAS	Computer Aided Software
CAD	Computer-Aided Design
DPT	Double Pulse Test
DUT	Device Under Test
DC	Direct Current
FET	Field Effect Transistor
FTDI	Future Technology Devices International (USB-to-Serial Converter)
GIMP	GNU Image Manipulation Program
GUI	Graphical User Interface
IDE	Integrated Development Environment
IDS	Drain Current
LDO	Low Dropout Regulator
MCU	Microcontroller Unit
MOSFET	Metal Oxide Semiconductor Field Effect Transistor
PCB	Printed Circuit Board
PC	Personal Computer
PDF	Portable Document Format

PID	Proportional Integral Derivative (Controller)
PT1000	Platinum Resistance Temperature Detector (1000)
PWM	Pulse Width Modulation
RTD	Resistance Temperature Detector
SiC	Silicon Carbide
SPI	Serial Peripheral Interface
TC	Thermocouple
VDS	Drain-to-Source Voltage
VGS	Gate-to-Source Voltage
Eon	Turn-on Switching Energy Loss
Eoff	Turn-off Switching Energy Loss
td(on)	Turn-on Delay Time
td(off)	Turn-off Delay Time
tr	Rise Time
tf	Fall Time
ton	Turn-on Time
toff	Turn-off Time
t1	First Pulse Duration in DPT
t2	Second Pulse Duration in DPT
tbreak	Pulse Break Interval
VDC	DC Link Voltage
Tj	Junction Temperature
RDS(on)	On-state Resistance of MOSFET
EL	Inductor Energy
P(t)	Instantaneous Power
Etotal	Total Switching Energy Loss

Appendix A

Source Code

A.1 Template File Formats

A.1.1 HSPICE

```
HEADER_FIRST: .SUBCIRCUIT &!cell_name &%I &%O &%IO &%S &@BulkNode
PIN_INFO: *.PININFO &(&%I : I &) \&(&%O : O &) &(&%IO : IO &
STOP_VIEW: M &^ &!inst_name &@d &@g &@s &@BulkNode nmos w= &@w l= &@l
INSTANCE: X &^ &!inst_name &%I &%O &%IO &!cell_name
```

A.1.2 VHDL

```
HEADER_FIRST ENTITY &!cell_name IS \n
\> PORT( \n \> &(&%I : IN std_logic; \n
&) \> &(&%O : OUT std_logic; \n
&) ); END &!cell_name NULL

PIN_INFO \n ARCHITECTURE madebyTDI of &!cell_name IS \n
\> &(& SIGNAL &(&%I : std_logic; \n
&) \> &(&%O : std_logic; \n
&) BEGIN NULL

INSTANCE \t X &- &!inst_name : &!cell_name \n
\> PORT MAP( \n
\> \t &(& IN => &%I , \n
```

```

&) \t    \t  &(& OUT => &%0 , \n
&) );  NULL

FOOTER END madebyTDI; NULL

```

A.2 Generated Netlists

A.2.1 HSPICE

```

** Cell 'c_inv', library: 'cmoslib', path
** '/opt/tech5/cmos/.dr/cmoslib/v2.1/cdb/cmoslib', vers 'vnil'
.SUBCKT c_inv in0 out0 hSup lSup nBulk pBulk nOL=1.0 nOW=1.0 pOL=1.0 pOW=1.0
*.PININFO in0:I out0:0

** The following net names were mapped:
** OriginalName: net11 mapped to: hSup
** OriginalName: net10 mapped to: lSup

Mn0 out0 in0 lSup nmod w='nOW*GEONSHRNK-2*GEONDEL2'
+ l='nOL*GEONSHRNK-2*GEONDEL1'
Mp0 out0 in0 hSup pBulk pmod w='pOW*GEOPSHRNK-2*GEOPDEL2'
+ l='pOL*GEOPSHRNK-2*GEOPDEL1'

.ENDS

** Cell 'rol_einfach', library: 'rol', path
** '/home/sab_kurs/fw1.1.1/v1.0.0/home/leng/lib_rol/rol', vers 'vnil'
XIN0 input output VDD VSS VDD VSS c_inv nOL=nOL pOL=pOL nOW=nOW pOW=pOW

```

A.2.2 VHDL

```

--Netlist:
--Time: Tue Jan 11 11:41:47 2000
--By: leng

--Library=cmoslib,Cell=c_inv,View=native
LIBRARY IEEE,cmoslib,proj_vhdl,proj_verilog;
USE IEEE.std_logic_1164.all;

```

```
USE work.all;
USE cmoslib.cmoslib.all;

ENTITY c_inv IS
  GENERIC (
    nOL : real := 1.0;
    nOW : real := 1.0;
    pOL : real := 1.0;
    pOW : real := 1.0
  );
  PORT(
    in0 : IN std_logic;
    out0 : OUT std_logic
  );
END c_inv;

ARCHITECTURE madebyTDI OF c_inv IS
  SIGNAL VSS : std_logic;
  SIGNAL VDD : std_logic;

  SIGNAL out0_ylw : std_logic;

BEGIN

  VSS <= '0';
  VDD <= '1';
  out0 <= out0_ylw;
  Mn0 : c_ntrans
    PORT MAP(
      d => out0_ylw,
      s => VSS,
      g => in0
    );

  Mp0 : c_ptrans
    PORT MAP(
      d => out0_ylw,
      s => VDD,
      g => in0
    );

```

END madebyTDI;